Antioxidant-loaded nanoparticles for the treatment of excitotoxicity in neurological disease

Rick Liao

A dissertation
submitted in partial fulfilment of the
requirements for the degree of

Doctor of Philosophy

University of Washington

2020

Reading Committee:

Elizabeth Nance, Chair
Jim Pfaendtner
Buddy Ratner
Thomas Wood

Program Authorized to Offer Degree:

Chemical Engineering

University of Washington

Abstract

Antioxidant-loaded nanoparticles for the treatment of excitotoxicity in neurological disease

Rick Liao

Chair of the Supervisory Committee:
Elizabeth Nance
Department of Chemical Engineering

In the United States alone, neurological diseases affect tens of millions of people, costing $800 billion annually. In acute neurological injury, a process known as excitotoxicity manifests from energy failure or direct trauma, causing overexcitation of neurons that leads to neuronal toxicity. Following neuronal death, toxic metabolites and cellular debris accumulate in the brain, perpetuating excitotoxicity to neighboring neurons. Despite the heavy social and economic toll and extensive research into neurotherapeutic development, there are currently no approved therapeutics for targeting excitotoxicity after acute neurological injury. The difficulty in clinical translation is largely attributed to several barriers intrinsic to the brain, including traversing the blood-brain barrier (BBB) and diffusion through the brain parenchyma. Therefore, in addition to understanding the biological complexity of the brain, developing effective therapeutics is a drug delivery problem.

To expedite the pre-clinical research process, we have developed a tailorable organotypic whole hemisphere (OWH) brain slice model, capable of mimicking *in vivo* processes including excitotoxity and neuroinflammation. Using OWH models, we can systematically study disease processes and screen therapeutics in a high-throughput fashion, bypassing delivery obstacles. To improve therapeutic enzyme delivery, we have developed brain-penetrating antioxidant enzyme-loaded polymeric nanoparticles that inhibit enzymatic degradation. Furthermore, via nanoparticle screening on the OWH model, we have elucidated the toxicity of a common polymeric nanoparticle formulation involving poly(ethylene glycol) (PEG) and sonication, and developed alternative biocompatible nanoparticle formulations. Finally, the OWH model has enabled detailed observation of disease-dependent nanoparticle-microglia interactions that can better inform drug delivery strategies. Throughout these studies, we have implemented a transdisciplinary approach that emphasizes thorough understanding of the neurobiology of disease and leverages chemical engineering fundamentals, to ultimately advance neurotherapeutic development.

TABLE OF CONTENTS

LIST OF FIGURES……………………………………………………………………………..v

LIST OF TABLES……………………………………………………………………………vii

ACKNOWLEDGEMENTS…………………………………………………………………..viii

CHAPTER 1: Introduction…………………………………………………………………...1

- 1.1 Neurological diseases and their social and financial impacts……………………………..1
- 1.2 Excitotoxicity……………………………………………………………………………1
- 1.3 Neuroinflammation………………………………………………………………………2
- 1.4 Antioxidant enzymes as therapeutics……………….……………………………………...2
- 1.5 The barriers to CNS drug delivery…………………………………………………………..3
- 1.6 Polymeric nanoparticles for drug delivery…………………………………………………..3
- 1.7 Organotypic whole hemisphere brain slice models………………………………………4
- 1.8 Overview of project chapters………………………………………………………………..5

CHAPTER 2: Methods………………………………………………………………………6

- 2.1 Animal work and ethics statement………………………………………………………….6
- 2.2 Preparation for OWH brain slice culturing…………………………………………………6
- 2.3 OWH brain slice culturing and disease induction…………………………………………...7
- 2.4 Lactate dehydrogenase (LDH) cytotoxicity of OWH brain slice supernatants…………...8
- 2.5 Immunofluorescence (IF) of OWH brain slices……………………………………………..8
- 2.6 Mitochondrial morphology of OWH brain slices…………………………………………...9
- 2.7 RT-PCR analysis of OWH brain slices…………………………………………………...9
- 2.8 8-OHdG ELISA of OWH brain slices……………………………………………………..10
- 2.9 PLGA-PEG nanoparticle formulation and characterization……………………………11
- 2.10 Catalase activity assay………………………………………………………………..12

2.11 Bicinchoninic acid (BCA) protein concentration assay……………………………………12

2.12 Scanning electron microscopy……………………………………………………………..13

2.13 Serum collection from rats…………………………………………………………...13

2.14 Catalase activity stability study……………………………………………………………13

2.15 Catalase activity stability in OWH brain slices…………………………………………….14

2.16 GSH assay of OWH brain slices…………………………………………………………...14

2.17 Hydrogen nuclear magnetic resonance (H-NMR) spectroscopy………………………..14

2.18 Differential scanning calorimetry…………………………………………………………15

2.19 pH measurement………………………………………………………………………...15

2.20 Propidium iodide (PI) of OWH brain slices………………………………………………..15

2.21 VAMPIRE for microglial morphometric analysis…………………………………………16

2.22 Polystyrene (PS) and dendrimer nanoparticle preparation and characterization………...16

2.23 Multiple particle tracking (MPT) in OWH brain slices……………………………………17

2.24 Flow cytometry of OWH brain slices……………………………………………………...17

2.25 IF for nanoparticle co-localization in microglia and neurons……………………………18

2.26 Statistics…………………………………………………………………………………...18

CHAPTER 3: Nanotherapeutic modulation of excitotoxicity and oxidative stress in acute brain injury……………………………………………………………………………………………..19

3.1 Neurological diseases and their social and financial impacts……………………………19

3.2 Mechanisms of excitotoxicity in acute brain injury……………………………………..20

3.3 Therapeutic requirements for overcoming CNS barriers………………………………..23

3.4 Application of nanoparticles and their therapeutic benefits……………………………..24

3.5 ROS scavenging antioxidant enzyme-loaded nanoparticles…………………………….25

3.6 ROS scavenging antioxidant-mimetic materials as nanoparticles………………………26

3.7 Broad-acting antioxidant-loaded nanoparticles……………………………………………27

3.8 Pitfalls of translating anti-excitotoxic therapies…………………………………………...29

3.9 Barriers to clinical translation of nanotechnologies for acute brain injury………………31

3.10 Conclusions and looking forward………………………………………………………….32

CHAPTER 4: Superoxide dismutase reduces monosodium glutamate-induced injury in an organotypic whole hemisphere brain slice model of excitotoxicity……………………………40

4.1 Introduction……………………………………………………………………………..40
4.2 Results…………………………………………………………………………………..40
    4.2.1 Establishment of the MSG-induced excitotoxicity slice model…………………..40
    4.2.2 Superoxide dismutase antioxidant effects on MSG-induced excitotoxicity……...44
4.3 Discussion……………………………………………………………………………46
4.4 Conclusion…………………………………………………………………………...51

CHAPTER 5: Enzymatic protection and biocompatibility screening of enzyme-loaded polymeric nanoparticles for neurotherapeutic applications………………………………………………52

5.1 Introduction……………………………………………………………………………..52
5.2 Results and Discussion…………………………………………………………………53
    5.2.1 Formulation optimization for nanoparticle enzyme activity and protection……...53
    5.2.2 Biocompatibility screening of DE and NPPT nanoparticles……………………...57
    5.2.3 The role of oxidative stress in DCM PLGA-PEG DE nanoparticle toxicity………63
    5.2.4 Exploration of PEG degradation and toxic product formation……………………65
    5.2.5 Alternative biocompatible nanoparticle formulations with enzymatic protection..67
5.3 Conclusions……………………………………………………………………………..70

CHAPTER 6: Nanoparticle-microglial interaction in the ischemic brain is modulated by injury duration and treatment……………………………………………………………………………71

6.1 Introduction……………………………………………………………………………..71
6.2 Results…………………………………………………………………………………..72
    6.2.1 OGD time-dependent severity……………………………………………………72
    6.2.2 Therapeutic effect of SOD and AZ on OGD-induced injury……………………...73
    6.2.3 OGD and AZ effects on microglial shape as determined by VAMPIRE…………74

6.2.4 OGD enhances nanoparticle diffusion through the brain ECS……………………76
6.2.5 Microglial uptake of nanoparticles is influenced by disease state and nanoparticle properties………………………………………………………………………79
6.3 Discussion………………………………………………………………………82
6.4 Conclusions……………………………………………………………………..87
CHAPTER 7: Research Summary……………………………………………………..88
7.1 Nanotherapeutic modulation of excitotoxicity and oxidative stress in acute brain injury………………………………………………………………………………88
7.2 Nanoparticle-microglial interaction in the ischemic brain is modulated by injury duration and treatment……………………………………………………………………89
7.3 Enzymatic protection and biocompatibility screening of enzyme-loaded polymeric nanoparticles for neurotherapeutic applications………………………………………...90
7.4 Superoxide dismutase reduces monosodium glutamate-induced injury in an organotypic whole hemisphere brain slice model of excitotoxicity………………………………..91
7.5 Determining dominant driving forces affecting controlled protein release from polymeric nanoparticles……………………………………………………………………92
7.6 Systems-level thinking for nanoparticle-mediated therapeutic delivery to neurological diseases………………………………………………………………………………93
APPENDIX A: Supplementary Figures to Chapter 4…………………………………….94
APPENDIX B: Supplementary Figures to Chapter 5…………………………………….96
APPENDIX C: Supplementary Figures and Tables to Chapter 6…………………………98
BIBLIOGRAPHY……………………………………………………………………100

LIST OF FIGURES

Figure 3.1: Schematic overview of excitotoxic and oxidative stress processes in acute brain injury with points of intervention……………………………………………………….……………22

Figure 4.1: Establishment of the *ex vivo* whole hemisphere slice model………………………...41

Figure 4.2: Establishment of the MSG-induced excitotoxicity slice model……………………...42

Figure 4.3: Fold-changes of mRNA markers for inflammation-, excitation-, and antioxidant-related proteins of NT, 100 mM MSG, 100 mM NaCl, and 100 ng/mL LPS slices at 6h.…………44

Figure 4.4: Therapeutic effect of SOD application on MSG-induced excitotoxic OWH slices…..45

Figure 4.5: The exploration of mechanistic effects of SOD administration………………………46

Figure 5.1: Characteristics of nanoparticles formulated with DE and NPPT methods…………...55

Figure 5.2: Nanoparticle protection of catalase activity in biologically relevant environments….57

Figure 5.3: Biocompatibility assessment of blank DE and NPPT nanoparticles…………………60

Figure 5.4: Determination of toxicity from DE nanoparticles……………………………………63

Figure 5.5: The role of oxidative stress in CHA PLGA-PEG DE nanoparticle toxicity…………..64

Figure 5.6: Characterization methods to detect potential PEG degradation and toxic product formation………………………………………………………………………………………66

Figure 5.7: Identification of non-toxic DE nanoparticles with enzymatic protection…………….69

Figure 6.1: OGD exposure-dependent effect on cell death and oxidative stress environment……73

Figure 6.2: Therapeutic effects on OGD exposure-induced injury……….……………………...74

Figure 6.3: AZ reverses microglial heterogeneity and circularity after 0.5h OGD………………76

Figure 6.4: Characterization of nanoparticle diffusive behavior after OGD ……………………..78

Figure 6.5: Microglial uptake of PS-PEG, D-Cy5, and QD nanoparticles at 5h for NC, 0.5h OGD, and 0.5h OGD+AZ treatment……………………………………………………………………80

Figure 6.6: Microglial number decreases after OGD and is restored with AZ …………………...81

Figure S4.1: Fold-changes of antioxidant mRNAs for NT, 1000 mM MSG, and 1000 mM NaCl slices at 6h…………………………………………………………………………………..94

Figure S4.2: Fold-changes of pro-inflammatory mRNAs for NT, 100 μM NMDA, and 100 mM NaCl slices at 6h…………………………………………………………………………………94

Figure S4.3: Fold-changes of excitation-related proteins and antioxidant enzyme mRNAs mRNAs for NT and 100 μM NMDA slices at 6h…………………………………………………………..95

Figure S5.1: Active/total protein ratio for CHA nanoparticle formulations determined from catalase activity and protein concentration via BCA assay……………………………………….96

Figure S5.2: Characteristics of PVA nanoparticles formulated with the alternative DE conditions…………………………………………………………………………………...96

Figure S5.3: Characteristics of CHA nanoparticles formulated with the alternative non-toxic DE conditions…………………………………………………………………………………...97

Figure S6.1: Nanoparticle boundedness and efficiency………………………………………….98

Figure S6.2: Microglial uptake of 100ng/μL PS-PEG nanoparticles……………………………..98

Figure S6.3: Flow cytometry results of microglia as a proportion of all live cells………………..99

LIST OF TABLES

Table 2.1. Forward and reverse primer sequences for RT-PCR……………………………………10

Table 3.1. Promising treatments for excitotoxicity in acute brain injury…………………………23

Table 3.2. *In vitro* and *in vivo* models of excitotoxicity, stroke, TBI, and HIE…………………34

Table 6.1. D_{eff} in rat brain tissue…………………………………………………………………77

Table S6.1. Average circularity of microglia by shape mode……………………………………….99

Table S6.2. Physicochemical properties of polystyrene nanoparticles used in MPT and nanoparticle uptake studies…………………………………………………………………………99

ACKNOWLEDGEMENTS

Thank you to my supervisory committee: Dr. Elizabeth Nance, Dr. Thomas Wood, Dr. Jim Pfaendtner, Dr. Buddy Ratner, and Dr. Jonathan Weinstein. Thank you for your expert research advice and for investing in my professional growth throughout graduate school.

Thank you to my sister Sonia, Mom, and Dad for supporting me throughout life and during these past five years. Special thanks to Sonia for helping raise me to be the person I am today and instilling a set of morals that I carry with me everywhere I go.

Thank you Elizabeth for accepting me as one of your first PhD students, along with Chad Curtis and Mengying Zhang. Joining a startup lab has been an invaluable experience. Being the first student is a bit like being the first-born child. I may have been dropped on my head once or twice, but I like to think of it as preconditioning for the challenges to come.

Thank you Elizabeth for teaching me the importance of relentless hard work. Your ability to stay focused towards your vision and your passion for everything neuro- and diffusion-related are inspiring. I am forever grateful that I had the opportunity to study the fascinating interface of chemical engineering, neuroscience, and nanomedicine. Without you, I would have never become a “neurobiochemical engineer.” Under your mentorship, I have gained the perspective of seeing the forest AND the trees with a confocal micro-to-macroscope. I have learned that only the integration of every pixel across time and length scales provides the full picture.

Thank you Tommy for taking me on as if I were one of your own graduate students. You have extensively helped my growth as a lab rat and gym rat. You and Elizabeth are an amazing duo and I am lucky to have been able to learn under your dual mentorship.

Thank you to the entire Nance lab family that I am proud to have helped build, and especially Chad and Mengying as companions for that first year. I am forever grateful to have undergone my PhD in a community that has been so kind, supportive, hilarious, and brilliant. I am constantly amazed at our caliber of people, in terms of both professional accomplishments and iconic personalities.

Thank you to my undergraduate mentees Cayen Panlilio, Belinda Garana, Alex Choe, Jessica Pon, and Mikey Chungyoun and high school STEMPREP mentees Sarah Sackeyfio, Maya Mallya, and Jessica Holloway. I am grateful for what I have learned in mentoring Team Scayence and am proud to have played a role in your exciting future careers.

Thank you Andrea Joseph and Mike McKenna for always being there for me through every struggle and celebration of grad school. I am grateful to have gotten to know you both as y’all have become some of my best friends. Seattle would not have been nearly the same without y’all.

Thank you Kate’s pub for welcoming us every first Friday of the month for Nance lab happy hour and for your $10 PBR pitchers. Chip and Taylor, y’all have been nothing short of amazing.

Thank you Alexandra Pretto for supporting me every day throughout these past five years. I know getting a PhD is not easy, and neither is dating someone who is. You always believe in me and push me to reach my potential. I can confidently say I am a better human in all aspects of my life because of you. I am grateful to have a happy family with you, Po Pretto 🐈‍⬛, and Leo Liao 🐰. All three of you make my heart melt every day.

CHAPTER 1: Introduction

1.1 Neurological diseases and their social and financial impacts

Despite the advancements of the past century, treating neurological diseases accounts for $800 billion annually, and is set to increase significantly as a larger percentage of the population ages past 65, when many neurological diseases manifest [1, 2]. In the United States, 5.7 million people are living with Alzheimer's, over 16 million adults have experienced depression, and about 3 million people have suffered from a traumatic brain injury (TBI) in the last year [3-5]. The costs associated with these diseases are not limited to the price of treatment and loss of earned wages, but also include an unquantifiable heavy physical and emotional toll on the afflicted, along with their family and friends. There is an urgent need for better understanding of and better treatment options for neurological diseases to alleviate the suffering that so many individuals endure. Although the etiologies of central nervous system (CNS) diseases vary widely from genetic predispositions to environmental factors, many CNS diseases have common pathological processes, including excitotoxicity and neuroinflammation.

1.2 Excitotoxicity

Glutamate is one of the primary amino acids, constituting a building block for all the proteins in the body. It is also the major neurotransmitter used for neuronal communication, responsible for the sense of sight, smell, taste (umami), nociception, and hearing, as well as the more complex processes of memory formation and learning [6]. However, when glutamate is in excess it plays a critical role in mediating neuronal injury by over-activating glutamate receptors in a process known as excitotoxicity [7, 8]. Glutamate acts on postsynaptic receptors to initiate an action potential, promoting the influx of sodium and calcium ions through ionotropic glutamate receptors, namely the NMDA (N-methyl-D-aspartic acid), AMPA (α-amino-3-hydroxy-5-methyl-4-isoxazolepropionic acid), and KA (kainic acid) receptors, named for their respective chemical agonists [6]. During excessive glutamate activation, calcium floods into the neuron, disturbing cell homeostasis, damaging mitochondria, and promoting the generation of nitrogen and oxygen radicals, ultimately initiating pro-apoptotic and necrotic processes [7, 8]. After death, neurons release their glutamate depots, which furthers neighboring neuronal death. Excitotoxicity occurs in almost every neurological disease as either the primary cause of damage during stroke, TBI, and neonatal hypoxia-ischemia (HI), or as secondary downstream pathology during depression, schizophrenia, amyotrophic lateral sclerosis (ALS), and Alzheimer's [9]. For all these diseases, arresting the excitotoxic cycle is crucial for stopping the detrimental cascade to prevent further brain injury and promote recovery.

1.3 Neuroinflammation

Accompanying excitotoxicity, neuroinflammation is also present in most neurological diseases. General inflammation is a common immune response by the body to adverse conditions, where vasodilation increases blood flow to better circulate leukocytes and nutrients. Some potential causes of inflammation include foreign body infection, tissue damage, autoimmunity, and diet [10, 11]. However, inflammation in the brain is unique from the rest of the body, involving local and systemic immune cells, and can be initiated by a variety of overlapping or distinct etiologies, including stress, TBI, infection, prematurity, and environmental factors [12-15]. In the presence of inflammation, microglia, the brain-resident macrophage, and astrocytes, a glial cell responsible for regulatory and protective functions, become activated, undergoing changes in their phenotype and function [10, 16-18]. For neuroinflammation, the line is blurred between when glial immune responses transition from providing a healthy protective response to becoming harmful and contributing to further damage [19]. Activated microglia proliferate and migrate to damaged areas; release reactive oxygen species (ROS), excitotoxic metabolites including glutamate, and pro-inflammatory cytokines; and become extra-phagocytic for the clearance of cellular debris [16, 20-24]. Activated astrocytes proliferate as well and undergo glial scarring to isolate and contain damaged areas [25, 26]. During this process, glial cells lose their neuroprotective functions, including the ability to scavenge free radicals and excitotoxic metabolites [27]. Metabolic and cellular waste builds up in the presence of inflammation, leading to further tissue damage and a chronic neuroinflammatory state [28]. Like excitotoxicity, neuroinflammation must be regulated to minimize the self-promoting cycle. Because of the complexity and intertwining processes of neurological diseases, excitotoxicity and neuroinflammation must be addressed together in an integrated understanding to develop more effective therapeutics.

1.4 Antioxidant enzymes as therapeutics

Enzymes are a promising source of therapeutics for excitotoxicity and inflammation, especially naturally produced enzymes that illicit no immunogenic response. As opposed to small molecule drugs, an individual enzyme can perform its catalytic function repeatedly instead of being expended as the substrate, yielding greater and sustained therapeutic benefit for a given drug dosage. The catalytic affinity and specificity of enzymes allows precise modulation of biological processes, including scavenging toxins or boosting production of therapeutic molecules. Antioxidant enzymes in their native form are actively studied for managing excitotoxic and inflammatory damage [29-31]. Catalase, superoxide dismutase (SOD), glutathione peroxidase, and other peroxiredoxins all work to eliminate oxidative agents including hydrogen peroxide (H_2O_2), superoxide anion radical (SOX, O_2^-), and peroxynitrite anion ($ONOO^-$) [32]. Catalase provides the additional benefit of producing oxygen, which could be beneficial in the HI environments of stroke, for example [33]. With precisely targeted and controlled metabolic intervention, antioxidant enzymes offer potential for attenuating neurological disease processes.

1.5 The barriers to CNS drug delivery

There are several physiological obstacles that adversely influence neurotherapeutic efficacy, including systemic clearance after intravenous injection and crossing the highly restrictive blood-brain barrier (BBB) [34]. The BBB prevents circulating blood from freely accessing the brain parenchyma, insulating the brain extracellular environment from potential blood composition fluctuations, and providing protection from infiltration of blood-based bacteria, viruses, fungi, or toxic metabolites [35]. The BBB is highly restrictive, ordinarily allowing the passive diffusion of only water, small lipid molecules, and some gases, and active transport of glucose and other small metabolites [35]. Additional barriers to CNS drug delivery are elaborated in Chapter 3.3. These restrictive obstacles have made drug discovery for CNS diseases especially difficult. While 15% of all drugs successfully pass clinical trials, only 8.2% of neuropsychiatric drugs succeed, and for excitotoxicity or Alzheimer’s, the success rate has been 0% [36]. New approaches must be adopted to improve upon neuroscience fundamental discovery and CNS drug development.

1.6 Polymeric nanoparticles for drug delivery

Polymeric nanoparticles hold promise in neurotherapeutic drug delivery, stabilizing enzyme-based therapeutics, demonstrating controlled drug release, and overcoming the barriers to CNS drug delivery [37]. One of the most common biomaterials used for polymeric nanoparticle synthesis is poly(lactic-co-glycolic acid) (PLGA), which has obtained FDA approval for use in drug delivery and biomedical applications [38, 39]. Polymeric PLGA nanoparticles are capable of carrying a variety of hydrophobic or hydrophilic therapeutic cargo within their polymer matrix core, including small molecule drugs and macromolecules such as proteins or DNA [40]. PLGA can be co-polymerized with poly(ethylene glycol) (PEG) to form a block co-polymer, improving nanoparticle circulation half-life for enhanced therapeutic effects [41]. PLGA biodegrades into the metabolic substrates lactic and glycolic acid, and PEG decomposes into smaller PEG units readily excreted by the kidney [38]. The toxicities of these polymer biomaterials are generally well-defined, but further research is warranted to ensure biocompatibility. Utilizing the drug delivery advantages of polymeric nanoparticles, we aim to develop enzyme-encapsulating nanoparticles for the treatment of excitotoxicity.

1.7 Organotypic whole hemisphere brain slice models

Organotypic whole hemisphere (OWH) brain slice models provide a simplified *ex vivo* system for studying therapeutic efficacy by bypassing the BBB yet still retaining most of the *in vivo* brain architecture and interactions. Organotypic hippocampal (OHC) slice cultures have been extensively used in research to study the effects of various toxins and small molecule agonists or inhibitors [42, 43]. We have adapted the OHC techniques to OWH slices to utilize more brain tissue to facilitate quantitative analyses and expanded the applications to serve as a screening tool for potential therapeutics. The *ex vivo* model serves as an intermediate alternative to neuronal/glial cell cultures that fail to capture complexity of the brain microenvironment, and *in vivo* animal models that are costly and suffer from confounding factors that limit mechanistic, systematic analysis, especially when incorporating all engineering and therapeutic controls. Despite the advancements obtained from *in vitro* cell cultures, they fail to resemble a physiological environment, lacking 3D architecture and interaction between neurons, microglia, astrocytes, and oligodendrocytes [44]. On the other hand, intricacies of the *in vivo* brain complicate accurate prediction and measurement of therapeutic transport, efficacy, and inadvertent toxicity [44, 45]. These complexities have potentially caused drug candidates to fail *in vivo* studies not because of ineffective biochemistry, but instead due to failure to overcome delivery obstacles. Simplified yet representative models of the *in vivo* environment with intentionally eliminated barriers provide a platform for systematic therapeutic evaluation [45]. By leveraging the OWH model as a screening tool prior to *in vivo* experimental investigations, we can refine the speed, efficiency, and efficacy of the pre-clinical drug discovery process for CNS diseases.

1.8 Overview of project chapters

In **Chapter 2**, we summarize all methods used throughout the thesis project research.

In **Chapter 3**, we provide a review of the neuropathology of excitotoxicity in acute brain injury, and of the nanotechnology strategies used thus far in combating excitotoxicity and oxidative stress *in vivo*. We also present the pitfalls of previous anti-excitotoxic therapies and provide recommendations towards clinical translation of anti-excitotoxic nanotechnologies.

In **Chapter 4**, we present the OWH rat brain slice model as a platform for disease-induction as well as a screening tool for potential therapeutics. We demonstrate the tailorability of the OWH model to imitate excitotoxicity and neuroinflammation, as well as the therapeutic potential of superoxide dismutase (SOD) in preventing excitotoxicity-induced oxidative stress. OWH models can better guide neurological disease research with high-throughput systematic and mechanistic analyses prior to pursuing time- and cost-intensive *in vivo* investigations.

In **Chapter 5**, we compare polymeric nanoparticles formulated with the double emulsion (DE) and nanoprecipitation (NPPT) method for the encapsulation of catalase and evaluate enzyme protection in the presence of degradative conditions. We use OWH models for toxicity screening of nanoparticle formulation parameters and discover PEG toxicity resulting from DE sonication in dichloromethane on oxidatively stressed brain tissue. We explore the potential causes of PEG toxicity and identify alternative formulations that are biocompatible and enzyme protective.

In **Chapter 6**, we characterize the effects on the brain microenvironment as a function of oxygen-glucose deprivation (OGD) injury severity as well as injury modulation with azithromycin (AZ) and SOD on OWH slices. We find that OGD injury elicits changes in microglial shape and interactions with polystyrene (PS)-PEG, dendrimer, and quantum dot (QD) nanoparticles, while AZ reverts microglial behavior to that of healthy tissue.

In **Chapter 7**, we summarize the thesis project research and other manuscript contributions.

CHAPTER 2: Methods

2.1 Animal work and ethics statement

This study was performed in strict accordance with the recommendations in the Guide for the Care and Use of Laboratory Animals of the National Institutes of Health (NIH). All animals were handled according to approved Institutional Animal Care and Use Committee (IACUC) protocol (#4383-02) of the University of Washington, Seattle, WA, USA. The University of Washington has an approved Animal Welfare Assurance (#A3464-01) on file with the NIH Office of Laboratory Animal Welfare (OLAW), is registered with the United States Department of Agriculture (USDA, certificate #91-R-0001), and is accredited by AAALAC International. Time-mated pregnant female Sprague–Dawley (SD) rats (virus antibody-free CD®, *Rattus norvegicus*, IGS, Charles River Laboratories, Raleigh, NC, USA) were purchased and arrived on estrous (E) day 17. Dams were housed individually and allowed to acclimate to their environment for a minimum of 3 days prior to delivering. The day of birth was defined as postnatal (P) day 0. Litters were culled to 12 animals early after birth. Before the removal for an experiment, each dam and her pups were housed under standard conditions with an automatic 12h light/dark cycle, temperature range of 20–26°C, and access to standard chow and autoclaved tap water *ad libitum*. The pups were checked for health daily.

2.2 Preparation for OWH brain slice culturing

P14 healthy SD rats were injected intraperitoneally with an overdose of 100 µL pentobarbital (Commercial Beuthanasia D, 390 mg/mL pentobarbital, administered >120-150 mg/kg), followed by rapid decapitation with surgical scissors once the body was non-responsive as indicated by no reaction from toe pinch with tweezers. After removing the brain under aseptic conditions, the brain was split into hemispheres with a sterile razor blade and sliced into 300 µm sections with a McIlwain tissue chopper (Ted Pella). Brain slices were separated in dissecting media (0.64% w/v glucose, 100% HBSS (Hank's Balanced Salt Solution), 1% penicillin-streptomycin). Brain slices were transferred onto 35-mm 0.4-µm-pore-sized membrane inserts (Millipore Sigma), and placed within a 6-well plate (CytoOne) containing 1 mL slice culture media (SCM; 50% MEM (minimum essential media), 50% HBSS, 1% GlutaMAX, and 1% penicillin-streptomycin). All media added to slices was pre-warmed at 37°C. For real time polymerase chain reaction (RT-PCR), 8-hydroxy-2-deoxyguanosine (8-OHdG) enzyme-linked immunosorbent assay (ELISA), reduced glutathione (GSH) assay, and flow cytometry measurements, 3 brain slices were plated per membrane insert. For all other experiments, 1 brain slice was plated per membrane insert. For hippocampal slice culture experiments, only the hippocampal sections from 6 adjacent slices were transferred to the membrane insert to obtain approximately the same amount of organotypic tissue as a single whole hemisphere slice. MEM was purchased from Invitrogen, glucose from Sigma, and HBSS, GlutaMAX, and penicillin-streptomycin from Gibco. The slices rested overnight in a CO_2 incubator (ThermoFisher Scientific) at culturing conditions (37°C with constant humidity, 95% air, and 5% CO_2) to equilibrate after the mechanical stress of slicing before proceeding with the next step of the experiments.

For Chapter 6, P7 healthy male SD rats were used and SCM consisted of 5% horse serum (ThermoFisher), 50% MEM, 45% HBSS, 1% GlutaMAX, and 1% penicillin.

2.3 OWH brain slice culturing and disease induction

After slices rested overnight, supernatant was collected (time t=-3h) and replaced with SCM, SCM with 0.1-1 μg/mL lipopolysaccharide (LPS O111:B4, Sigma), SCM with 1-1000 mM monosodium glutamate (MSG, Sigma), or oxygen-glucose deprivation (OGD) SCM for disease induction if applicable. SCM without any additional exposures served as the non-treated (NT) control, and SCM containing 1% Triton X-100 (TX, Cayman Chemical), a surfactant that induces death and membrane permeabilization of all cells, served as the maximum death control. OGD SCM consisted of 150 mM sodium chloride (NaCl, Sigma), 2.8 mM potassium chloride (KCl, Sigma), 1 mM calcium chloride ($CaCl_2$, Sigma), and 10 mM 4-(2-hydroxyethyl)piperazine-1-ethanesulfonic acid buffer solution (HEPES, Gibco) in deionized water (DI) titrated to pH 7.4 with 1 M hydrochloric acid (HCl, ThermoFisher) or 1 M sodium hydroxide (NaOH, ThermoFisher), and bubbled with nitrogen gas (Praxair) for 10 min. For OGD-exposed slices, the 6-well plate was placed in a Hypoxia Incubator Chamber (STEMCELL Technologies) and placed in a 37°C incubator. The chamber was flushed with nitrogen gas (Praxair) for 10 minutes, followed by clamping of the tubing, and continued slice incubation for the rest of the 3h. For slice culturing studies, the end of the 3h incubation was defined as time t=0h. At t=0h, the supernatant was collected and replaced with normal SCM. TX control slices were cultured with NT SCM during the 3h incubation, and then with TX SCM beyond t=0h. At t=0h, 100 µL PBS (1x phosphate buffered saline, Gibco) per slice containing nanoparticles, surfactant, 0.01-0.1 mg superoxide dismutase (SOD, Cu/Zn SOD1 from bovine erythrocytes, Sigma), 0.75 µg (150 mg/kg brain tissue) AZ (Zithromax), or pure SCM as a control, was gently added to the top of the brain slices using a cut-tip pipet. 6-well plates incubated at culturing conditions until further processing.

For Chapter 6, after slices rested overnight in the incubator, supernatant was removed and fresh SCM was added, followed by one or two more days of rest. All samples underwent OGD after 3 days *in vitro* (DIV), except for flow cytometry studies, which underwent 2 DIV. OWH slices underwent OGD for 0.5h, 1.5h, or 3h prior to t=0h. For the healthy condition referred to as normal control (NC) instead of NT, slices proceeded directly to t=0h without OGD media exchange.

2.4 Lactate dehydrogenase (LDH) cytotoxicity of OWH brain slice supernatants

Supernatant collection and SCM replacement were repeated at time 1h, 2h, 4h, 8h, and 24h for LDH. All supernatant samples were immediately stored in -80°C. Supernatant samples were removed and thawed at room temperature to conduct LDH assays (601170, Cayman Chemical). Following the manufacturer's instructions, 100 µL of LDH reaction buffer was added to 100 µL of sample supernatant in triplicate to 96-well plates on ice, and the plates were transferred to a stir plate in a 37°C incubator. After 30 min, the plates were placed on ice, and 490 nm absorbance was measured on a SpectraMax M5 UV-Vis Spectrophotometer (Molecular Devices) to detect the production of colorimetric formazan. Percent cytotoxicity was calculated using Equation 1.

$$\%\,cytotoxicity = \frac{cumulative\ LDH\ absorbance\ of\ sample}{24h\ cumulative\ LDH\ absorbance\ of\ reference\ sample} \times 100\% \qquad (1)$$

2.5 Immunofluorescence (IF) of OWH brain slices

OWH brain slices were fixed in 10% formalin (10% phosphate buffered formalin, ThermoFisher) with 1 mL below membrane insert and 500 µL directly on the slice at room temperature for 1 hour. Slices were washed twice with PBS and stored in 1 mL PBS until IF staining. Recombinant antibodies for neurons (rabbit anti-NeuN 488, Abcam) were prepared 1:250 in PBS with 0.3% TX (PBS+). Primary antibodies for microglia (Wako rabbit anti-Iba1+, Abcam) and neurons (rabbit anti-MAP2, Abcam) were prepared 1:250 in PBS+ with 6% goat serum (Sigma) (PBS-g++). 250 µL primary antibody solutions were added to each tissue section for 6h at room temperature. Sections were washed twice in PBS. Secondary antibodies for microglia or neurons (Alexa Fluor

(AF)-488 IgG goat anti-rabbit, Invitrogen) were prepared 1:500 in PBS+. For microglia and MAP2 neuron staining, 250 μL secondary antibody solutions were added to each tissue section for 2h and washed twice in PBS. Sections were stained with 1 mL of 1:1000 or 1:10000 4′,6-diamidino-2-phenylindole (DAPI, Invitrogen) in PBS for 15 min, washed twice in PBS, and then stored in PBS at 4°C until imaged on a Nikon confocal microscope. 20x confocal z-stack images set to max intensity projection were obtained for NeuN neuronal, Iba1+ microglial, and DAPI nuclei imaging. 40x confocal images were obtained for MAP2 neuronal imaging.

2.6 Mitochondrial morphology of OWH brain slices

Starting with 1 mM MitoTracker Deep Red FM (ThermoFisher) stock solution in dimethyl sulfoxide (DMSO, Sigma), MitoTracker was diluted to a working solution of 500 nM in SCM. After warming to 37°C, at t=0h 1 mL SCM with MitoTracker was added below the membrane insert and 100 μL applied on top of each brain slice followed by 1h at culturing conditions. For SOD-treated slices, the 100 μL SCM with MitoTracker contained 0.1 mg SOD. Slices were then washed once with SCM, and then formalin fixed, stained with DAPI, and stored as described above. 240x (60x lens with 4x zoom) confocal images were obtained for representative mitochondrial morphology.

2.7 RT-PCR analysis of OWH brain slices

Slice culture preparation for RT-PCR was similar to LDH slice preparation. Three slices were plated per membrane insert to obtain sufficient tissue for RNA extraction (~30 mg) and incubated with SCM containing 100-1000 mM MSG, 100-1000 mM NaCl, 100 ng/mL LPS, or 100 μM NMDA for 3h. At t=0h, supernatant was replaced with 1 mL normal SCM, and 300 μL SCM containing 0.3 mg SOD was added on top of the 3 slices for SOD-treated samples. OWH slices were removed from culturing at t=6h. Slices were gently separated from the membrane inserts with a flat spatula and transferred to a 20 mL scintillation vial containing 1 mL of RNALater (Invitrogen) and stored at -80°C. After the slices thawed, RNALater was removed and 1 mL of TRIzol (Invitrogen) was added. RNA extraction was performed following the TRIzol manufacturer protocol. Slices were homogenized by pipetting repeatedly with a Pasteur pipet. Chloroform (Sigma) was then added to the tube followed by centrifugation. The top aqueous phase was collected into another tube and underwent a series of centrifugation and washing steps with isopropanol and ethanol [46]. After measuring RNA concentration with Nanodrop

(ThermoFisher), 2 μg RNA was converted to cDNA with the High Capacity RNA to cDNA kit (Applied Biosystems). mRNA expression fold-changes were measured with the SYBR Green RT-PCR kit (Applied Biosystems) for the mRNAs IL-1β (interleukin-1 beta), IL-6, TNF-α (tumor necrosis factor-alpha), Dlg4 (discs large MAGUK scaffold protein 4), EGR1 (early growth response 1), nNOS (neuronal nitric oxide synthase), HMOX1 (heme oxygenase 1), GCLM (glutamate-cysteine ligase modifier subunit), and SOD1 (copper/zinc superoxide dismutase). ΔΔCt values were calculated, with reference to the NT slice control sample with GAPDH (glyceraldehyde-3-phosphate dehydrogenase) as the housekeeping gene. RT-PCR was conducted using technical duplicates or triplicates, and sample size varied from n=3 to n=12 for the datasets presented in the study. Forward and reverse RNA primers (Table 2.1) were obtained from Integrated DNA Technologies.

Table 2.1. Forward and reverse primer sequences for RT-PCR.

Gene	Accession number	Forward primer	Reverse primer
GAPDH	NM_017008.4	GTC GGT GTG AAC GGA TTT	TGT AGT TGA GGT CAA TGA AGG
IL-1β	NM_031512.2	TTC GAC AGT GAG GAG AAT G	GAT GCT GCT GTG AGA TTT G
IL-6	NM_012589.2	GGA GAC TTC ACA GAG GAT AC	GCC ATT GCA CAA CTC TTT
TNF-α	NM_012675.3	CCT CAG CCT CTT CTC ATT C	GGA ACT TCT CCT CCT TGT T
Dlg4	NM_019621.1	CGG GAA CAG CTC ATG AAT A	TCC TTG GTC TTG TCG TAA TC
EGR1	NM_012551.2	CTG ACC ACA GAG TCC TTT	GGT AGT TTG GCT GGG ATA A
nNOS	NM_052799.1	AGC GTC TCC TCC TAT TCT	ACT GAG AAC CTC ACA TTG G
HMOX1	NM_012580.2	CAC ATC CGT GCA GAG AAT	GGC CAT CAC CAG CTT AAA
GCLM	NM_017305.2	CAG TGG GCA CAG GTA AA	GTG AGT CAG TAG CTG TAT GT
SOD1	NM_017050.1	GTG GTG TCA GGA CAG ATT AC	TGG TAC AGC CTT GTG TAT TG

Primers were designed to have an amplicon size between 50-150 base pairs, 40-60% GC content, no four consecutive nucleotide repeats, melting temperature (T_m) between 58-60°C, and no more than three G or C bases among the last 5 nucleotides of the 3’ end.

2.8 8-OHdG ELISA of OWH brain slices

After removal of the aqueous phase containing RNA, the remainder of the TRIzol/chloroform mixture was used for DNA isolation following the Invitrogen protocol. For each condition, n=3 DNA samples were obtained. The DNA was precipitated with 100% ethanol, and then centrifuged and washed twice with 0.1 M sodium citrate (Sigma) in 10% ethanol, pH 8.5, and once with 75% ethanol. After resuspension in 8 mM NaOH, and pH adjustment to 7.5-8.5 with HEPES (ThermoFisher), DNA purity and concentration was measured with Nanodrop (ThermoFisher).

DNA was then digested with S1 nuclease (ThermoFisher) and alkaline phosphatase (Sigma). The 8-OHdG ELISA kit (Abcam) was performed following the manufacturer's instructions. Dependent on the enzymatic color reaction of 3,3′,5,5′-tetramethylbenzidine (TMB) Substrate, 8-OHdG concentration was measured at 450 nm on a SpectraMax M5 UV-Vis Spectrophotometer (Molecular Devices).

2.9 PLGA-PEG nanoparticle formulation and characterization

The water 1/organic/water 2 (w_1/o/w_2) double emulsion (DE) method was used for enzyme encapsulation. One mg enzyme was dissolved in 100 μL PBS and combined with 100 μL of 1 wt% cholic/deoxycholic acid sodium salt (CHA, bile salts, Sigma) or 1 wt% polyvinyl alcohol (PVA, Sigma) surfactant dissolved in DI for w_1 phase. The w_1 aqueous phase was combined with 25 mg of PLGA copolymerized with PEG (PLGA-PEG, 45k lactic:glycolic 50:50 PLGA-5k PEG, Akina) dissolved in 1 mL dichloromethane (DCM, Fisher Scientific), ethyl acetate (EtAc, Avantor), or trichloromethane (TCM, chloroform, Fisher Scientific) for organic phase and emulsified with a Sonic Dismembrator Ultrasonic Processor (Fisher Scientific). The slightly miscible, but incompatible w_1/o phases were emulsified by 20 kHz probe sonication at 30% amplitude with 1s on:1s off pulses for 1s, 15s, 30s, or 60s on. After adding 4 mL 3% CHA or 5% PVA in DI as the w_2 phase, the second sonication was performed at 20% amplitude with 1s on:1s off pulses for the same length of time. This emulsion was then poured into a beaker with 25 mL PBS (sink) stirred at 500-rotations per minute (rpm) for organic solvent evaporation. After 3h, the nanoparticles were collected with a 1h 100k relative centrifugal unit (RCF) centrifugation step, followed by 5 mL PBS resuspension, 30m 100k RCF centrifugation, and final resuspension in 1 mL PBS. To remove aggregates, the nanoparticle solution was transferred to a new tube after 10 seconds of mini benchtop centrifugation and stored at 4°C until further usage. For a subset of DE formulations, 25 mg of PLGA (45k lactic:glycolic 50:50, Akina) was used instead of PLGA-PEG, or 5 mg methoxy-PEG with a hydroxyl terminus (mPEG-OH, Creative PEGWorks) was dissolved either in the DCM, in the sink phase, or in the PBS final resuspension phase. Nanoparticles were characterized by dynamic light scattering (DLS) to measure hydrodynamic diameter and polydispersity index (PDI), and by laser Doppler anemometry to measure ζ-potential. Both DLS and laser Doppler anemometry were carried out using a Zetasizer Nano ZS (Malvern Panalytical, Malvern, UK).

For the nanoprecipitation (NPPT) method, 1 mg enzyme was dissolved in 100 μL PBS and combined with 400 μL 1% CHA or PVA in DI, and 25 mg PLGA-PEG polymer was dissolved in 500 μL acetone (Sigma). After combining and vortex mixing the aqueous and organic phases for 2 seconds, the solution was added dropwise with a 1 mL Hamilton syringe (Hamilton) to beaker with 25 mL PBS. Nanoparticles were collected via the same methodology as above for DE method.

2.10 Catalase activity assay

Catalase (catalase from bovine liver, Sigma) was used as a model enzyme due to its facile enzymatic activity measurement using a catalase spectrophotometric assay adapted from Beers and Sizer [47]. A pH 7.0 solution of 0.036% w/w H_2O_2 (Sigma) was prepared in 50 mM phosphate buffer (PB) with a 240 nm absorbance between 0.48-0.52. In an optically clear quartz cuvette (Hellma Analytics), 100 μL of catalase sample was added to 2.9 mL of H_2O_2 solution, mixed via pipetting, and 240 nm absorbance was measured at 1s intervals for 3 min using a kinetic spectrometric reading on a SpectraMax M5 UV-Vis Spectrophotometer (Molecular Devices). The active units per mg of catalase were calculated using Equation 2:

$$\frac{Units}{mg\ solid} = \frac{\frac{(3.45)(df)}{(time)(0.1)}}{\frac{mg\ solid}{mL\ enzyme}} \tag{2}$$

In the equation, 3.45 represents the decomposition of 3.45 μmoles of H_2O_2 during 240 nm absorbance decrease from 0.45 to 0.4, *df* is the dilution factor of the sample, and 0.1 is the mL volume of sample added. This assay measures catalase activity even when the enzyme is encapsulated, due to the ability of H_2O_2 to diffuse throughout the polymer matrix [48]. Stock catalase had 2000-3000 active units (AU) per mg of catalase.

2.11 Bicinchoninic acid (BCA) protein concentration assay

100 μL of catalase-loaded nanoparticles was combined with 50 μL of 1 M NaOH (ThermoFisher). The solution was vortexed for 2s, spun down on a minicentrifuge, and then incubated at 37°C for 30 minutes for base-catalyzed hydrolysis of the PLGA polymer to release all loaded catalase. 50 μL PBS was then added to neutralize the solution. The sample was then tested for protein concentration with the Pierce BCA Protein Assay Kit (ThermoFisher). Following the manufacturer's instructions, 25 μL sample was added to 96-well plate in triplicate on ice. After

addition of 200 μL BCA assay working reagent (50:1 reagent A:B), the plate was placed on a shaker plate at 37°C for 30 min. After 30 min, the plate was placed on ice, and 562 nm absorbance was measured on a SpectraMax M5 UV-Vis Spectrophotometer (Molecular Devices).

2.12 Scanning electron microscopy

For CHA 1s and 30s DE and NPPT nanoparticle formulation conditions, nanoparticle samples were further processed for scanning electron microscopy. After the final centrifugation, nanoparticles were resuspended in DI instead of PBS and diluted 100x in 200 proof ethanol (Decon Labs). Subsequently, 100 μL of the diluted nanoparticle solutions were pipetted onto a silicon wafer and allowed to air-dry for 1h in a fume hood. The nanoparticles were sputter coated with palladium under an argon environment and imaged on the FEI XL830 Dual Beam Focused Ion Beam/Scanning Electron Microscope in the UW Molecular Analysis Facility.

2.13 Serum collection from rats

Adult rats were injected intraperitoneally with an overdose of 500 μL pentobarbital for euthanization. Immediately after death, the chest cavity was opened to expose the heart, upon which a 22g needle syringe (BD) was used to puncture the left ventricle for blood draw. Blood was transferred to 1.5 mL microcentrifuge tubes and incubated for 60 minutes at room temperature to permit coagulation. The tubes containing coagulated blood were spun at 2k RCF for 10 min at 4°C. Serum was transferred to a separate tube and immediately stored at -80°C. Serum samples were thawed and mixed with free catalase or used for resuspending nanoparticles, and then assayed for catalase activity as described above.

2.14 Catalase activity stability study

For the catalase activity stability studies, free catalase or catalase-loaded nanoparticles were stir-incubated in PBS with 0.2 wt% pronase (pronase from *Streptomyces griseus*, Sigma) or in rat serum at 37°C. For the activity stability studies with pronase, at 0h, 1h, 2h, 4h, 8h, and 24h, aliquots were collected, placed on ice, and immediately tested for catalase activity. For the activity stability studies in serum, aliquots were tested at 0h, 0.25h, 1h, 2h, and 6h. Enzyme activities were calculated as the sample activity at a given timepoint divided by the initial sample activity at 0h.

2.15 Catalase activity stability in OWH brain slices

Supernatant was not exchanged at any timepoint after t=0h. 100 µL of SCM containing free catalase was applied on top of slices, and 900 µL of normal SCM was applied below the membrane insert. Slices and supernatant were collected at 0h, 2h, and 24h after catalase addition, homogenized, and immediately stored at -80°C. Samples were thawed and assayed for catalase activity as described above.

2.16 GSH assay of OWH brain slices

At t=24h, brain slices were immediately frozen at -80°C for GSH detection with the GSH/GSSG ratio detection assay kit fluorometric green (Abcam). Following the manufacturer's instructions, samples were homogenized in 400 µL of ice-cold mammalian lysis buffer composed of 0.5% NP-40 Surfact-Amps™ Detergent Solution (ThermoFisher) in PBS at pH 6.0 by pipetting up and down with a 200 µL pipetman. After centrifugation and transfer of supernatant to remove tissue debris, enzymes were removed by precipitating proteins with trichloroacetic acid (TCA), centrifugation, and pH neutralization with sodium bicarbonate following the Deproteinizing Sample Kit – TCA (Abcam). Sample supernatants were then diluted 10-fold in assay buffer. 50 µL of GSH standards and diluted sample supernatants were added to a 96-well plate, followed by the addition of 50 µL of GSH Assay Mixture (GAM) to each well while on ice. The 96-well plate was incubated for 60 min at room temperature in the dark, followed by 490/520 excitation/emission fluorescence measurement reading on a SpectraMax M5 UV-Vis Spectrophotometer (Molecular Devices) to measure the extent of thiol green indicator reaction with GSH. Adjusting for volume resuspension and dilutions, GSH concentrations were reported as µmoles GSH per gram of initial brain tissue.

2.17 Hydrogen nuclear magnetic resonance (H-NMR) spectroscopy

One mL non-loaded nanoparticles were frozen at -80°C and lyophilized to a powder in a FreeZone 2.5 Liter -84°C Benchtop Freeze Dryer (Labconco). Powdered nanoparticles were dissolved in 600 µL deuterated chloroform (MilliporeSigma) and added to 5 mm outer diameter economy NMR tubes (Wilmad-LabGlass). One sample per condition tested was scanned for 1H shifts relative to deuterated chloroform with a Bruker AV-300 NMR spectrometer. Measurements were run with 32 scans, recycle delay of 8, sweep width of 15, and time domain of 64k. Spectra were analyzed in Bruker CMC-assist software.

2.18 Differential scanning calorimetry (DSC)

Analogous to the DE formulation process, 25 mg mPEG-OH (Creative PEGWorks) was dissolved in 1 mL DCM and sonicated with 200 µL DI for 0s, 30s, 60s, or 300s, followed by a second sonication of the same duration after the addition of 4 mL DI. Samples stir-incubated for 3h to evaporate off DCM, and were then frozen at -80°C, and lyophilized to a powder in a FreeZone 2.5 Liter -84°C Benchtop Freeze Dryer (Labconco). Between 4-6 mg of PEG lyophilized powder were added and sealed in a Premium Hermetic Pan/Lid (DSC Consumables) sample holder. Samples underwent a heat/cool/heat/cool/heat ramp to a maximum temperature of 80°C and minimum temperature of -60°C with a ramp of 10°C/min. The temperature at which the minimum heat flow occurred on the third heat ramp was recorded as the melting point temperature of the sample.

2.19 pH measurement

25 mg mPEG-OH (Creative PEGWorks) or no polymer was dissolved in 1 mL DCM or EtAc and sonicated with 200 µL DI for 0s, 30s, or 300s, followed by a second sonication of the same duration after the addition of 4 mL DI. Samples stir-incubated for 3h to evaporate off organic solvent. pH was measured with an Accumet pH meter (Fisher Scientific).

2.20 Propidium iodide (PI) of OWH brain slices

At t=24h, slices were stained with 1 mL SCM with 5 µg/mL PI in SCM for 45 min at culturing conditions. Slices were washed twice for 5 min with SCM, followed by a 1h wash with SCM at culturing conditions, and then formalin fixed, stained for microglia, stained with DAPI, and stored as described above. 40x confocal images were obtained for PI, DAPI, and Iba1+. For every slice, five images were acquired from each brain region of interest (cortex and thalamus). Image acquisition settings were consistent for all images. For each image, DAPI+ cell nuclei (total cells) and PI+ cell nuclei (dead cells) that were also DAPI+ were counted manually in ImageJ (NIH) after applying an Otsu threshold and fluorescent cutoff to aid in visualization. The PI+/DAPI+ cell ratio was expressed as the percentage of dead cells in an individual image. Image acquisition and analysis was performed in a blinded manner. Iba1+ images were analyzed separately from PI and DAPI using an adaptation of Visually Aided Morpho-Phenotyping Image Recognition (VAMPIRE) [49].

2.21 VAMPIRE for microglial morphometric analysis

All confocal microscopy images were converted from the Nikon file format (.nd2) to .tiff. Using Python in a Jupyter Notebook, all images were separated by RGB channel and labeled with the appropriate cell stain: DAPI for the blue channel and Iba1+ for the green channel [50-52]. Every image was then split into four quadrants using Image_slicer. Scikit-learn was used to split all images in an 80:20 test-to-train ratio [53], assuring at least two images for each slice of the three experimental conditions: NC, 0.5h OGD, and 0.5h OGD+AZ. Cells from each image were segmented using Cell Profiler and the Cell Profiler pipeline from the Denis Wirtz Group associated with the VAMPIRE package [54]. A model of shape modes was built from all training images with the VAMPIRE package and associated protocol (https://github.com/kukionfr/VAMPIRE_open) [49], and then applied to all images. The shape mode frequencies of individual slices were averaged for resulting distribution plots. Equation 3 was used to calculate the difference in sample shape mode frequency from NC shape mode frequency:

$$Absolute\ difference = |x_n - x_{NC,n}| \tag{3}$$

where *n* is the shape mode (1 through 5), x_n is the sample frequency for shape mode *n*, and $x_{NC,n}$ is the NC frequency for shape mode *n*. Circularity was calculated with equation 4:

$$Circularity = \frac{4\pi A}{P^2} \tag{4}$$

where *A* is the area and *P* is the perimeter for each microglia.

2.22 Polystyrene (PS), dendrimer, and quantum dot (QD) nanoparticle preparation and characterization

40 nm dark red fluorescent carboxylate (COOH)-modified PS latex nanoparticles (PS-COOH) (Thermo Fisher Scientific, Waltham, MA) were covalently modified with methoxy (MeO)-PEG-amine (NH_2) (5 kDa MW, Creative PEG Works, Durham, NC) by a carboxyl amine reaction [55]. Generation-4 hydroxyl modified polyamidoamine (PAMAM) dendrimers labeled with Cy5 (D-Cy5) were provided by Dr. Rangaramanujam Kannan and Dr. Anjali Sharma at the Johns Hopkins University Center for Nanomedicine [56, 57]. These conjugates are stable at physiological conditions and have been validated for *ex vivo* application at the concentration used in our study (10 ng/uL) [58]. CdSe/CdS core-shell QDs with PEG-methoxy functionality were provided by Dr.

Vince Holmberg in the Department of Chemical Engineering at the UW, which were proven stable at physiological conditions for *ex vivo* application [59]. Nanoparticles were measured with a Malvern Zetasizer for hydrodynamic diameter and ζ-potential.

2.23 Multiple particle tracking (MPT) in OWH brain slices

At t=24h for NC, 0.5h, 1.5h, and 3h OGD samples, SCM was exchanged for a nuclear staining solution consisting of 1 mL SCM and 5 drops NucBlue Live ReadyProbes Reagent (Hoechst 33342, ThermoFisher). Slices were stained for 1h at culturing conditions then washed twice with 1 mL warm SCM for 5 min each. Following the second wash, 0.5 µL injections of 40 nm PS-PEG nanoparticle stock diluted in PBS to a concentration of ~0.0011% (w/w) solids were carried out in each slice using a 10 µL glass syringe (model 701, cemented needle, 26 gauge, Hamilton Company, Reno, NV). Four injections were made in the cortex and three in the striatum. Slices were transferred to a temperature-controlled imaging incubation chamber maintained at culturing conditions, where they remained throughout the imaging window. Video acquisition began 30 min after nanoparticle injection and was completed within 2h. A total of five videos were collected from the cortex and striatum of each slice. Videos were collected at 30.3 frames-per-second and 100x magnification (0.07 µm/pixel) for 651 frames via fluorescent microscopy using a cMOS camera (Hamamatsu Photonics, Bridgewater, NJ) mounted on a confocal microscope. Nanoparticle trajectories, trajectory mean squared displacement (MSD), effective diffusion coefficient (D_{eff}), and features were calculated via diff_classifier, a Python package developed within our group [60]. To obtain distributions of brain extracellular matrix (ECM) pore sizes, the measured D_{eff} were fit using an obstruction-scaling model described by Amsden and coworkers [61]. This method has previously been applied to MPT data to characterize pore sizes of the ECS in *ex vivo* brain tissue [34].

2.24 Flow cytometry of OWH brain slices

Flow cytometry was performed on NC, 0.5h OGD, and 0.5h OGD+AZ OWH slices. Each group included n=5 samples per condition and 3 slices per sample. At t=1h, nanoparticles were topically pipetted on the OWH slices (10 µL of 1 ng/µL PS-PEG, D-Cy5, PS-COOH, or QD). Slices for each condition were placed in 1 mL Accutase (Millipore Sigma) at t=5h. Samples were homogenized and filtered with a 250 µm Pierce Tissue Strainer (ThermoFisher) to remove large debris. Following a wash step, microglia were isolated using a Percoll (Sigma-Aldrich) gradient.

The cells were then stained with DAPI (1:10,000) and FITC anti-rat CD11b antibody (BioLegend, 1:200). Appropriate controls for CD11b gating were done with an aliquot of the control sample. The BD LSRII (BD Biosciences) machine recorded cells in each sample with fluorescence in the DAPI, CD11b, and Cy5 channels until 100,000 events (live cells) were reached. Analysis of the cytometry data was performed in FCS Express 7 Research. For microglial number data, slices with PS-COOH were processed at t=25h.

2.25 IF for nanoparticle co-localization in microglia and neurons

To probe nanoparticle interactions with microglia, at t=1h PS-PEG, D-Cy5, and QDs (10 µL of 1 ng/µL) were topically pipetted on NC, 0.5h OGD, and 0.5h OGD+AZ OWH slices. The slices were rested for 4h at culturing conditions to allow the nanoparticles to diffuse through the brain tissue and interact with microglia. At t=5h, the slices were washed with PBS to remove excess nanoparticles that were not taken up intracellularly. After fixation, the slices were washed twice and stained with 200 µL primary antibodies for neurons (mouse anti-MAP2, Abcam) and microglia (rabbit anti-Iba, Wako) prepared 1:200 in PBS+ with 6% donkey serum (Sigma) (PBS-d++) for 6h. Secondary antibodies for neurons (AF-488 donkey anti-mouse, Invitrogen) and microglia (AF-546 donkey anti-rabbit, Invitrogen) prepared 1:500 in PBS+ were applied to slices for 2h, followed by DAPI staining and storing as described above. 240x (60x lens with 4x zoom) confocal z-stack images of nanoparticles and cells were performed with a z-step of 0.1-0.2 µm.

2.26 Statistics

All statistical analyses were carried out in GraphPad Prism (GraphPad Software Inc, Version 8.4.0). The D'Agostino-Pearson omnibus K2 test was used to test for normality for MPT and n=18 LDH datasets. The null hypothesis that the data were sampled from a normally distributed population was rejected for MPT and the LDH NT condition. The Kruskal-Wallis test was thus used to test for significance across groups and Dunn's method to correct for multiple comparisons. For all other datasets, normality was assumed, and significance was assessed using parametric unpaired t-tests with Welch's correction. Data were plotted as mean ± standard error of the mean (SEM) error bars displayed on the graphs, unless the error bars were too small to visualize. Statistical significance was reported at two *p*-value levels: $p<0.05$ (*) and $p<0.001$ (**).

CHAPTER 3: Nanotherapeutic modulation of excitotoxicity and oxidative stress in acute brain injury

3.1 The impacts and challenges of neurological disease

Acute brain injury is a common phenomenon associated with significant morbidity and mortality. Each year in the United States, around 800 thousand people suffer from a hemorrhagic or ischemic stroke, 60 thousand newborns experience hypoxic-ischemic (HI) encephalopathy, and 3 million people suffer from a traumatic brain injury (TBI) [62-64]. The costs associated with these diseases total over $113 billion per year [62, 65, 66]. Acute brain injuries exhibit a set of characteristic mechanisms that contribute to neurological damage. The pathological sequelae include immediate cell death and tissue loss followed by ongoing excitotoxicity, inflammation, and oxidative stress [67, 68]. Excitotoxicity is the pathological process of neuronal death due to dysregulated neuronal overstimulation by excitatory amino acids (EAAs) such as glutamate. Excitotoxicity leads to oxidative stress, where an excess of reactive oxygen species (ROS) exhausts native antioxidant systems. Understanding the etiology of neurological disease progression, especially the role of excitotoxicity and oxidative stress, is essential for determining ideal points of intervention for the development and implementation of effective therapeutics.

There have been extensive efforts in the fundamental sciences of pathology, immunology, and neuroscience to expand knowledge of excitotoxic neuronal death to elucidate key stages of intervention. Promising candidates include natural antioxidant, inorganic antioxidant-mimetic, and growth factor therapeutics, among others. However, developing a successful therapeutic requires a drug that not only has biochemical efficacy, but also effectively accumulates at the target site at therapeutic concentrations. In neurological disease, free drugs often fail to reach the target site due to *in vivo* degradation, systemic clearance mechanisms, and the barrier properties of the neurovascular unit [69]. Consequently, despite the research progress achieved, there are currently no approved therapeutics for targeting excitotoxicity or its direct sequelae after acute neurological injury. Nanotechnology can be leveraged to help overcome each of the aforementioned delivery obstacles to the brain. By conjugating drugs to nanoparticle surfaces, encapsulating drugs within nanoparticles, or utilizing materials with intrinsic therapeutic effects in nanoparticle form, nanoparticle therapeutics can stabilize labile free drugs and traverse steric obstacles to reach diseased sites [69]. Here, we provide an overview of the relevant disease mechanisms and points of intervention in excitotoxicity and subsequent oxidative stress including the advantages of nanotechnology, a summary of nanotherapeutic progress achieved thus far with a focus on *in vivo* work, and research strategies to implement for effective clinical translation.

3.2 Mechanisms of excitotoxicity in acute brain injury

During neuronal activity, vesicles with neurotransmitters in the presynaptic neuron merge with the membrane, expelling their contents, namely glutamate, into the synaptic cleft [70]. Glutamate then rapidly diffuses across the synapse to bind to ionotropic glutamate receptors on the postsynaptic neuron, eliciting an influx of sodium, which triggers an action potential that propagates down the neuron, forming the basis of neuronal communication [6]. Astrocytic end feet enveloping the synapse rapidly uptake glutamate to recycle back to the presynaptic neuron to replenish vesicular stores [71]. Upon neuronal excitation, calcium also influxes and binds to post synaptic density protein 95 (PSD-95) to initiate the recruitment of neuronal nitric oxide synthase (nNOS) and production of nitric oxide (NO) [7]. NO then activates the nicotinamide adenine dinucleotide phosphate oxidase (NOX) complex that generates superoxide radical anion (SOX, O_2^-) [72].

In acute brain injury, a number of pathological processes result in excitotoxicity depending on the nature of the insult. During stroke and HI encephalopathy, asphyxiation reduces ATP production leading to sodium/potassium ATPase pump failure and subsequent anoxic depolarization-induced glutamate release [73]. Under hypoxia, as cells switch to lactic acid production and undergo acidosis, ATP generation further decreases, inhibiting ATP-dependent astrocytic glutamate reuptake [74]. In TBI, direct trauma induces immediate necrotic death of neurons and glia resulting in neuronal release of their glutamate stores, and subsequent dysregulation of cerebral blood flow leading to similar energy deficits as occurs in stroke and HI [75, 76]. Once blood flow returns after a hypoxic event, reperfusion injury may exacerbate neuronal damage [77]. Regardless of the injury, excessive synaptic glutamate accumulation causes excitotoxicity [7, 8]. Substantially elevated intracellular glutamate, ROS, and calcium levels lead to cell death, increased glutamate release from dying neurons, and propagation of excitotoxicity [7, 78].

Mitochondria play a prominent role in excitotoxicity, oxidative stress, and cell death processes due to energy, calcium, and ROS dynamics [79]. During excitotoxicity, mitochondria uptake excess cytosolic calcium and produce high concentrations of SOX during mitochondrial respiration in response to excitatory postsynaptic currents [80]. NOX-derived SOX triggers even greater SOX production from mitochondria [81-84]. SOX mediates mitochondrial damage, resulting in electron transport chain failure as well as reverse electron transport leading to greater SOX production [81]. Other sources of SOX include production by xanthine oxidase or invading neutrophils during reperfusion, monoamine oxidase, and uncoupled nNOS by SOX oxidation of the nNOS cofactor tetrahydrobiopterin [77, 85-88]. Abundant SOX reacts with NO to form peroxynitrite, which can cause lipid peroxidation, protein deactivation, DNA mutation, and poly(ADP ribose) polymerase (PARP) activation [89, 90]. High intracellular calcium and SOX levels lead to extensive mitochondrial fission and mitochondrial permeability transition pore (mPTP) formation [80, 91]. The exact mechanism of mPTP formation remains to be elucidated, but ROS contributes several roles [92-94]. mPTP formation results in burst release of SOX, calcium, and other necrosis and apoptosis effectors into the cytosol [95]. Constituting a reinforcing cycle, mitochondrial burst release of SOX further induces NOX SOX production and neighboring mitochondrial stress, reducing mitochondrial antioxidant functions [81, 96]. As excitotoxicity, ROS generation, and mPTP formation are intimately linked to death processes, ROS scavenging is a promising therapeutic strategy after acute brain injury.

After acute neurological injury, a number of neuroinflammatory processes occur both alongside and due to excitotoxicity. Oxidative stress plays a prominent role in neuroinflammation as well. SOX generated from NOX and subsequent oxidation to hydrogen peroxide (H_2O_2) elicit microglial proliferation and other downstream inflammatory signaling pathways [97, 98]. For instance, in perinatal asphyxia models, HIE induces both excitotoxic neuronal death as well as neuroinflammatory microglial proliferation [99]. Inflammation can in turn cause further delayed excitotoxicity, as occurs in depression and Parkinson’s disease [100, 101]. Therefore, therapies that manage oxidative stress seen after acute neurological injury have the combined promise of alleviating excitotoxicity as well as neuroinflammation. An in-depth discussion of neuroinflammation is beyond the scope of this chapter, and we refer readers to other reviews [14, 102, 103]. Figure 3.1 illustrates the major processes of excitotoxicity along with therapeutic points of intervention, while Table 3.1 introduces promising therapeutic candidates at these points of intervention and the potential benefits that nanotechnology can provide.

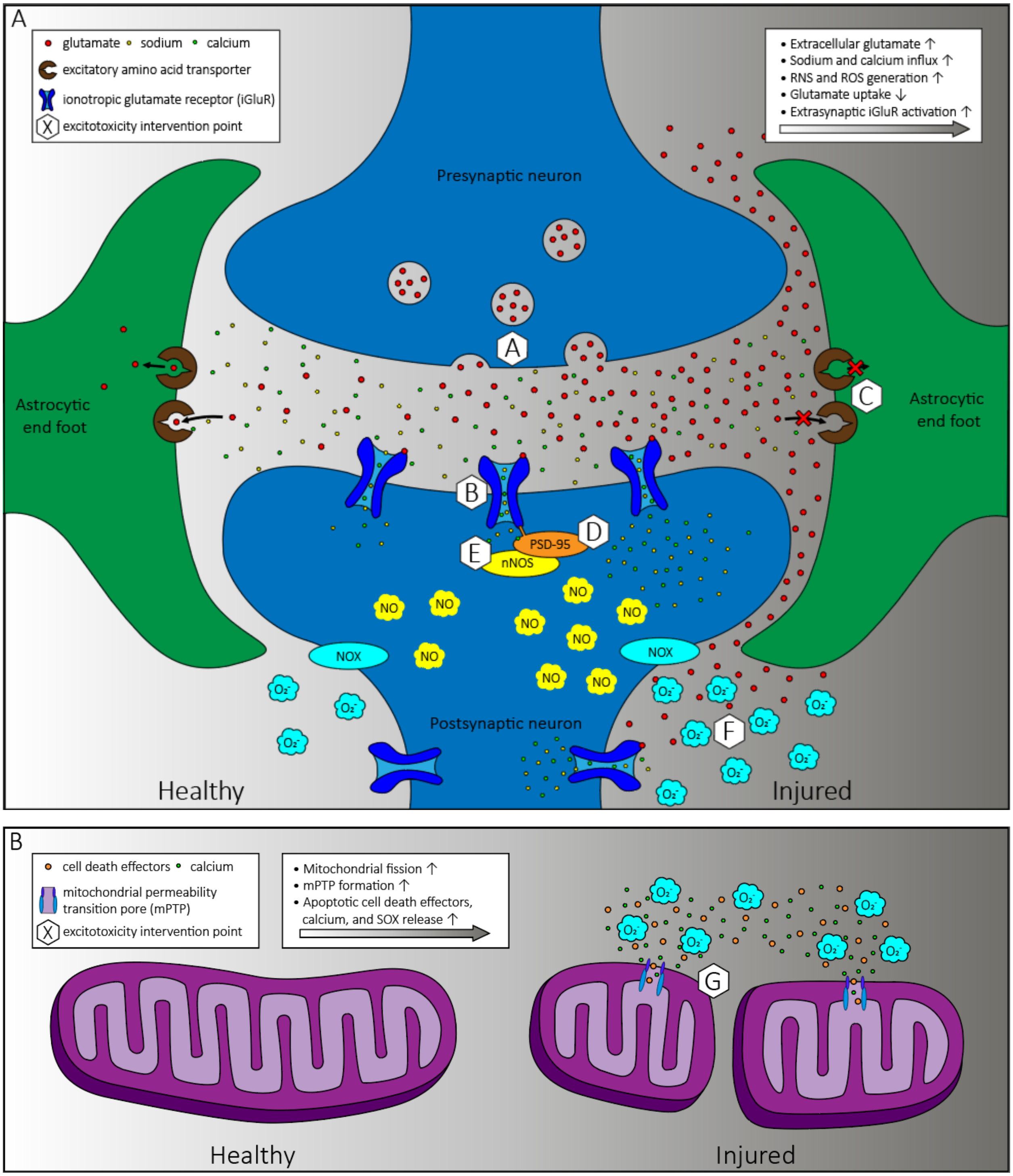

Figure 3.1: Schematic overview of excitotoxic and oxidative stress processes in acute brain injury with points of intervention (white hexagons labeled A-G) at the A) synapse and B) mitochondria, where the left side is healthy, and the right side is injured. Excessive glutamate concentrations in the synapse can lead to excitotoxicity through enhanced ionotropic glutamate receptor activation, sodium and calcium influx, and

generation of NO and SOX. These processes amplify mitochondrial ROS stress, resulting in mitochondrial fragmentation and mPTP formation, and release of calcium, SOX, and apoptotic cell death effectors.

Table 3.1. Promising treatments for excitotoxicity in acute brain injury corresponding to Figure 3.1 points of intervention, labeled in white hexagons as A-G. These therapeutics could potentially benefit from nanoparticle strategies to surpass biological barriers and increase site specific localization.

	Point of intervention	**Therapeutic candidates**	**Mechanistic effect**	**Nanocarrier benefit**
A	Presynaptic glutamate release	levetiracetam [104, 105]	Presynaptic glutamate release inhibitor	Sustained release
B	Ionotropic glutamate receptor	selfotel, aptiganel, eliprodil, licostinel, gavestinel [106]	N-methyl-D-aspartate (NMDA) receptor antagonist	Target site specific delivery
C	Glutamate uptake	ceftriaxone [107-109]	Astrocytic EAAT2 expression upregulation	Target site specific delivery
D	PSD-95	Tat-NR2B9c [110-112]	PSD-95 inhibitor	Protease protection
E	nNOS	2-iminobiotin [113-116]	iNOS and nNOS inhibitor	Aqueous solubility
F	SOX generation	allopurinol [117, 118]	Xanthine oxidase inhibitor	Controlled release
		apocynin [94, 119, 120]	NOX inhibitor	Target site specific delivery
G	Mitochondrial metabolism	creatine [121-123]	Improve mitochondrial bioenergetics	BBB permeability
		nicotinamide riboside [124]	Precursor for NAD+, improve mitochondrial bioenergetics	Target site specific delivery

3.3 Therapeutic requirements for overcoming CNS barriers

To combat oxidative stress in excitotoxicity, a therapeutic must perform its biochemical function of scavenging ROS or inhibiting ROS generation but also be capable of reaching the diseased area. The mammalian body is highly efficient in the clearance of foreign substances. The kidneys readily filter out molecules smaller than 5 nm, while the liver metabolizes any molecule above 200 nm before reaching the brain [125]. Therapeutics also require an inert near-neutral surface charge to avoid non-specific adsorption to circulating serum proteins, extracellular matrix components, or cell membranes [126]. Without an inert surface, therapeutics can readily be opsonized for digestion by resident macrophages within many organs [127]. Furthermore, the *in vivo* microenvironment may affect drug stability with potential deactivation due to proteases, oxidation/reduction, hydrolysis, pH, and unfavorable binding. Therapeutic proteins are especially susceptible to rapid degradation from *in vivo* proteases [48, 128, 129]. Even after overcoming systemic clearance, a therapeutic must be capable of crossing the highly restrictive blood-brain barrier (BBB) [130]. The

BBB inhibits passage of all macromolecules such as proteins, and 98% of small molecule drugs [131]. However, in acute brain injuries such as stroke and TBI, there is some BBB breakdown, resulting in “leakiness” of the BBB to a wider range of molecules [132-134]. After admittance to the brain, a therapeutic must avoid expulsion by efflux transporters such as the P-glycoprotein, ATP-binding cassette, and solute carrier transporters, and then subsequently navigate the brain parenchyma to reach diseased areas [135, 136]. Depending on the ultimate target, a therapeutic may also require a specific surface chemistry to undergo cell-type specific uptake.

3.4 Application of nanoparticles and their therapeutic benefits

As introduced in Chapter 1.6, nanotechnology can assist in maintaining therapeutic stability and overcoming the barriers to brain delivery. There are a wide variety of nanoparticle platforms used for therapeutic delivery to the brain, including polymeric nanoparticles, liposomes, hydrogels, and dendrimers. Polymeric nanoparticles can provide controlled drug release, targeting capabilities, and prolonged drug action by protection from proteases, and have been shown to cross an intact or impaired BBB [37, 48]. Nanoparticle size, shape, flexibility, and surface charge can be tailored to overcome steric clearance and non-specific binding to alter pharmacokinetics and improve brain accumulation [137-139]. With a dense poly(ethylene glycol) (PEG) coating, nanoparticles exhibit increased systemic circulation time by reducing interactions that lead to clearance and opsonization [130]. Densely PEG-coated nanoparticles up to 114 nm are also capable of diffusive and convective transport through the brain parenchyma [41, 140]. Drug-incorporation strategies include loading within nanoparticle matrices, cores, or lipophilic bilayers, or covalent conjugation to surface end groups [69]. To improve pharmacokinetics or cellular uptake, nanoparticles can also be further decorated with surface ligands or surfactants, while incorporation of biology-responsive materials can further specialize therapeutic delivery [37, 141]. Incorporation of pH-sensitive groups can imbue nanoparticles with triggered release capabilities, only releasing drug when reaching the acidotic ischemic area, or when internalized within an acidic lysosome [142, 143]. Similar strategies apply for attachment of protease-cleavable linkers and oxidation/reduction-sensitive bonds [144, 145]. Superparamagnetic nanoparticles can also be guided to diseased tissue regions using magnetic resonance (MR) [146]. Nanoparticles may also serve as biomarkers of disease, however, biomarker applications are outside of the scope of this chapter and have been covered in other reviews [147, 148]. By leveraging the benefits of nanoparticle drug delivery and understanding neurological disease processes at the biomolecular level, therapeutic agents can be better designed to combat excitotoxicity.

3.5 ROS scavenging antioxidant enzyme-loaded nanoparticles

Nanoparticles have been investigated for delivering therapeutics in *in vivo* models of stroke, TBI, and HI. One of the most promising enzyme therapeutic candidates is superoxide dismutase (SOD), a native antioxidant enzyme that converts SOX into H_2O_2 and water. SOD-loaded polymeric poly(lactic-co-glycolic acid) (PLGA) nanoparticles reduced infarct volume by 65% in a middle cerebral artery occlusion (MCAO) rat model, compared to only a 25% reduction from free SOD alone [149]. While 0% of rats survived without treatment after 4 weeks, SOD-nanoparticle application resulted in 75% survival [149]. Similarly, Yun et al. evaluated SOD delivery in liposomes, polybutylcyanoacrylate (PBCA) nanoparticles, and PLGA nanoparticles in a mouse model of multi-vessel ischemia (MVI). All three platforms resulted in 35-45% infarct volume reduction, with 50-60% reduction when conjugated with N-methyl-D-aspartic acid receptor 1 (NMDA-R1) antibodies [150]. The efficacy of SOD-loaded liposomes against bilateral common carotid artery occlusion (BCCAO) was also evaluated in gerbils, where treatment prevented a decrease in endogenous SOD levels and mitigated mitochondrial membrane lipid peroxidation but failed to reduce brain swelling [151]. From other studies, SOD-loaded liposomes reduced infarct size by 18-33% after focal cerebral ischemia in rats, and reduced BBB permeability and brain edema in cold-induced TBI rats [152, 153]. In a MCAO mouse model, SOD-encapsulating polyion condensation complexes of PEG-b-poly(aspartate diethyltriamine) (PEG-DET) or PEG-b-poly(L-lysine) (PEG-PLL) followed by crosslinking reduced infarct volume by 50-60% [154, 155].

Even though SOD converts SOX into H_2O_2, there is evidently a therapeutic benefit in reducing SOX levels at the expense of increasing H_2O_2 levels, by reducing mitochondrial oxidative stress and fragmentation [156]. Catalase scavenging of H_2O_2 by itself or in tandem with SOX scavenging has also shown positive effects in reducing acute brain injury. Catalase delivery via PLGA polymer or polyion complexed micelle nanoparticles has been explored *in vitro*, but *in vivo* application has been limited [157, 158]. Zhang *et al.* observed a reduction in infarct size with cross-linked dendrigraft poly-L-lysine (DGL) nanoparticles containing cis-aconitic anhydride-modified catalase after MCAO in mice, with further infarct reduction when nanoparticles were decorated with N-acetyl-proline-glycine-proline tripeptides with a high affinity for neutrophils, which enhanced BBB penetration [159]. SOD and catalase loaded separately into PLGA nanoparticles were administered after tissue plasminogen activator (tPA) in a thromboembolic stroke rat model, resulting in reduced number of caspase-positive cells, neutrophils, and hippocampal swelling, and an increase in nestin-positive neuron progenitor cells [160]. Combinatorial delivery of SOD nanoparticles and catalase nanoparticles offers promise in disrupting neuronal death processes via interruption of SOX-mediated primary damage as well as longer time-scale inflammatory processes caused by H_2O_2 accumulation [161]. Although enzyme-encapsulating nanoparticles are promising for combating excitotoxicity with their precise and continuous catalytic functions, enzyme delivery still faces many challenges including poor hydrophilic macromolecule loading in hydrophobic matrices, and enzyme deactivation from high-energy mixing and organic/aqueous interfaces during formulation processes [162-164]. Researchers are exploring other antioxidant-capable nanoparticle strategies that circumvent some of these challenges.

3.6 ROS scavenging antioxidant-mimetic materials as nanoparticles

Nanoparticles themselves may be composed of therapeutic materials that exhibit antioxidant capabilities [165, 166]. Cerium oxide nanoparticles of 4 nm diameter exhibit SOD- and catalase-mimetic activity, and can scavenge NO, and peroxynitrite [167]. They have been shown to reduce infarct size by over 50% after MCAO in rats at 0.5 mg/kg and 0.7 mg/kg doses [168]. Interestingly, higher concentrations of 1 mg/kg and 1.5 mg/kg provided no significant change in infarct volume compared to no treatment [168]. Cerium oxide nanoparticles have been covered in-depth in other reviews [167, 169, 170]. Platinum nanoparticles are also SOD- and catalase-mimetics and result in reduced infarct size in the cortex after transient MCAO in mice [166]. Yttrium oxide nanoparticles have similar antioxidant effects as cerium oxide nanoparticles in *in vitro* cell culture and could warrant further exploration [171].

Fullerene nanoparticles, which are carbon allotropes consisting of sixty carbons in a spherical arrangement, have also been investigated for their free radical scavenging capabilities of neutralizing hydroxyl radicals, SOX, and NO by transferring radicals into stable conformations within the fullerene nanoparticle [172-174]. Hydroxylated fullerene nanoparticles reduced neuronal death in the CA1 hippocampal region after MVI in rats [175]. Vani *et al.* applied hydroxylated fullerene nanoparticles before or after MCAO in rats, yielding a 53% or 81% reduction in infarct volume, respectively, a reduction in malondialdehyde levels, and rescuing of glutathione (GSH) content and SOD activity [176]. Carboxyfullerene nanoparticles decreased cortical infarction and prevented GSH depletion and lipid peroxidation, but also had adverse effects including writhing and even cell death in rats after MCAO and BCCAO [173]. Fullerenes can also produce pro-oxidant SOX and singlet oxygen in the presence of UV light, which could lead to adverse effects if fullerene nanoparticles localize in skin epithelium [174]. This UV-induced radical producing capability warrants further study of fullerene nanoparticles in the presence of other biologically relevant radical-generating conditions such as free iron.

PEG-functionalized hydrophilic carbon clusters (PEG-HCCs) consisting of 40 nm by 2-3 nm carbon nanotubes have also been explored for excitotoxic and immunomodulation applications due to their SOD-mimetic and hydroxyl radical scavenging properties [177, 178]. Interestingly, PEG-HCCs are inert towards NO and peroxynitrite, holding potential as selective ROS scavengers that avoid NO scavenging and consequent vasodilatation and blood flow interference [177]. PEG-HCCs can also load hydrophobic molecules into their hydrophobic core for combinatorial therapy [179]. PEG-HCCs administered during reperfusion of transient MCAO rats under hyperglycemic conditions resulted in a 42% reduction in infarct size, and reduced edema and hemorrhage [180]. PEG-HCCs furthermore normalized NO and SOX levels and restored cerebral blood flow after controlled cortical impact (CCI)-induced TBI in rats [181]. With self-regenerating ROS-specific rapid antioxidant capacity, PEG-HCCs warrant further investigation as a viable excitotoxicity therapeutic for stroke and TBI applications [179]. Due to the non-biological origin of antioxidant-mimetic material nanoparticles and their relatively recent application in the neurological disease fields, further research is also needed to assess their long-term biocompatibility, clearance and pharmacokinetics, and maximum tolerated dosing before translation to clinical trials can be achieved [182, 183].

3.7 Broad-acting antioxidant-loaded nanoparticles

While the antioxidant nanoparticle strategies covered thus far have focused on specific scavenging of SOX and/or H_2O_2, there are also several broad-acting antioxidants that have utilized nanoparticle delivery to improve therapeutic accumulation at the target site to enhance efficacy. Erythropoietin (EPO) exerts its neuroprotective effects for acute brain injury by chelating iron to reduce radical formation, modulating inflammation in multiple brain cell types, and acting as a neurotrophic agent [184-186]. EPO delivery within PLGA nanoparticles has been shown to reduce infarct volume in a perinatal rat model of HI encephalopathy at 10-times lower doses than recombinant EPO [187].

Curcumin is a small molecule found in the culinary spice turmeric that has broad-acting anti-inflammatory and antioxidant effects. Curcumin has been associated with activation of the antioxidant response element pathway in mice after closed-skull impact-induced TBI, ~50% infarct volume reduction after MCAO in rats, and microglial polarization towards the anti-inflammatory state after distal MCAO in mice [188-190]. However, curcumin's direct application for acute brain injury is suboptimal due to its hydrophobicity and consequent low aqueous solubility. Curcumin incorporation within PLGA-PEG nanoparticles permitted curcumin penetration across the BBB, diffusion effectively to disease sites, and a decreased infarct size in neonatal rats with unilateral HI brain injury while free curcumin provided no significant therapeutic efficacy [99]. Curcumin loaded within solid lipid nanoparticles administered orally to rats after BCCAO also improved neurological scoring by 79% and restored SOD, GSH, and catalase levels to sham control levels [191]. Curcumin-loaded N-isopropyl acrylamide (PNIPAM) nanoparticles administered intranasally after MCAO in rats restored grip strength, locomotor activity, glutathione peroxidase, glutathione reductase, SOD, and catalase activity, and reduced lipid peroxidation and neuronal loss by ~40% [192].

Multiple other antioxidants have also shown promise for acute brain injury when incorporated into nanoparticle platforms. Melanin exhibits broad antioxidant activity against SOX, H_2O_2, hydroxyl radical, peroxynitrite, and NO [193]. Injection of PEGylated melanin nanoparticles before MCAO injury in rats resulted in ~50% infarct reduction and showed no immediate toxicity in preliminary *in vitro* and *in vivo* studies [193]. N-acetylcysteine (NAC) is a precursor to GSH and therefore an antioxidant and free radical scavenger, as well as a pleiotropic anti-inflammatory agent [194]. Once internalized into cells, NAC is hydrolyzed to release cysteine which is then used for GSH production [194]. NAC-conjugated dendrimers (D-NAC) administered to neonatal mice that underwent permanent unilateral carotid artery ligation with mild hypoxia improved white matter myelination [195]. Adenosine provides neuroprotection by binding to inhibitory adenosine A_1 receptors to hyperpolarize neurons and reduce glutamate release, mitigating downstream excitotoxic processes [196, 197]. The hydrophilic small molecule adenosine is readily metabolized and cleared in the bloodstream, but when conjugated to squalene and formed into nanoparticles, these adenosine complexes significantly improved neurologic deficit scores after MCAO in mice

[198]. Broad-acting antioxidants are promising in mitigating ROS damage in acute brain injury, and many also exhibit broad anti-inflammatory properties as well, which may further improve therapeutic efficacy. However, because pleiotropic drugs enact efficacy via multiple neuroprotective mechanisms, gleaning broader understanding of therapeutic strategies to combat excitotoxicity from these studies is limited.

3.8 Pitfalls of translating anti-excitotoxic therapies

Despite having been described as a key component of the pathophysiology of acute neurological injury mechanisms for several decades, there remains a distinct lack of therapeutics targeting excitotoxicity in routine clinical use. A large part of this lack of successful translation is likely due to the issues outlined above – the requirement of more targeted or stable delivery of therapeutics to the site of injury. However, a number of other obstacles or common problems exist in the translational pipeline that should be addressed as new therapeutics are developed. These include the timing of the therapeutic, adequate control of confounding physiological factors in preclinical studies, and the number and heterogeneity of animal models assessed prior to clinical trials.

The timing of therapies with respect to the specific pathophysiological processes that occur after injury is a crucial component of successful clinical translation. This is likely to be particularly important for therapies that directly target the accumulation of EAAs such as glutamate. For instance, in piglet models of perinatal HI brain injury, a small increase in extracellular glutamate is seen during the insult itself as a result of primary energy failure, followed by a decrease after resuscitation until a significant increase as secondary energy failure occurs 6-12h later [199]. Preclinically, therapeutic hypothermia (TH) is significantly neuroprotective in a wide range of acute brain injuries, at least in part due to its ability to suppress the release of EAAs [200-202]. However, TH has only shown clinical success after perinatal asphyxia, and must be initiated within 6h of the injury or earlier for maximum benefit [203].

Similarly, the NMDA-R antagonist xenon augments hypothermic neuroprotection in rat and piglet models of perinatal asphyxia when given at a concentration of 50% and initiated within 3h of resuscitation [204-206]. Yet, the TOBY-Xe trial found no benefit of adding xenon to TH for infants after birth asphyxia, with significant confounders including that median time of xenon onset was 10h (range: 4.0-12.6h), and that it was given at a concentration of 30% [207]. Overall, the data therefore suggest that any directly anti-excitotoxic therapy must be in place as soon as possible after reperfusion [203]. This may be because of ongoing excitotoxicity that occurs even in the absence of measurable increases in extracellular glutamate. For instance, despite the relatively delayed rise in glutamate after injury, others have shown that an "excitotoxic index" consisting of relative levels of glutamate and glycine to γ-aminobutyric acid (GABA) begins to increase almost immediately after resuscitation in a piglet model of perinatal HI brain injury [208]. In the clinical setting, it is likely that any anti-excitotoxic therapeutic should therefore be at high local concentrations within 3-6h of the initial injury, and this must be incorporated into the design of both preclinical and clinical studies. Importantly, therapies that target downstream mitochondrial dysfunction, neuroinflammation, and oxidative stress, which continue to occur over hours to days, may have an extended therapeutic window as long as they can be reliably delivered to the site of injury [209].

The history of anti-excitotoxic therapies, particularly when used in rodent studies, is significantly confounded by issues with temperature regulation because hypothermia, which is known to be neuroprotective, spontaneously occurs after brain injury and is rarely adequately controlled [203, 210-212]. Additionally, glutamate signaling plays a dominant role in thermoregulation and maintenance of normal temperature, with pharmaceutical inhibition of glutamate signaling generally associated with loss of cold-evoked temperature responses (e.g. brown fat thermogenesis), and subsequent hypothermia [213-215]. In both animal models and humans, early spontaneous hypothermia is a common occurrence after global brain injury, with greater decreases in core temperature generally seen with a greater extent and severity of injury [210, 216-219]. In preclinical models at least, this spontaneous hypothermia can result in neuroprotection, with enforced periods of temperature regulation required after injury to standardize the degree of injury seen [210, 220]. However, in one analysis of studies assessing neuroprotective strategies in adult rodent models of both global and focal ischemia, only around 30% of studies did temperature measurements after the injury procedure [211]. A more recent analysis of preclinical studies examining neuroprotective agents in neonatal HI brain injury found similar results [212].

In their seminal paper in 2006, O'Collins *et al.* described "1,026 Experimental Treatments in Acute Stroke", the vast majority of which had not been translated to clinical trials [221]. Anti-excitotoxic therapies provided, on average, about 25% neuroprotection, which was a similar magnitude to thrombolysis, the current standard of care for acute ischemic stroke. The general lack of successful translation of anti-excitotoxic therapies in this setting may either be due to problems with timing relative to injury, or that the majority of benefit from directly anti-excitotoxic therapies, for instance those that regulate glutamate release or signaling, result in hypothermia that is not controlled for in the preclinical setting [211, 212]. Hypothermia has not been shown to be robustly beneficial after stroke, TBI, or global brain ischemia (e.g. after cardiac arrest) in pediatric or adult populations [200, 202, 219]. However, rigorous temperature management is commonplace in hospitalized adults after global and focal acute brain injuries due to the benefit of preventing hyperthermia (fever) [200, 219, 222, 223]. Therefore, more evidence is still required to examine whether directly anti-excitotoxic therapies will have their place in routine clinical use by providing neuroprotection above and beyond their effects on thermoregulation. Although promising, antioxidant-nanoparticle therapies will also necessarily undergo the same rigor of evaluation before clinical translation.

3.9 Barriers to clinical translation of nanotechnologies for acute brain injury

As with the majority of putative therapies developed for treating neurological disorders, any lack of success in the clinical setting could potentially be determined earlier by developing an adequate preclinical pipeline [224]. This was the goal of the STAIR (Stroke Therapy Academic Industry Roundtable) criteria when they were developed more than two decades ago. To fully meet the criteria, a therapy had to be successfully tested: i) in two or more laboratories, ii) in two or more species, iii) in animals at a disease-appropriate life stage, iv) in both sexes, v) in both temporary and permanent models of ischemia, vi) at least 1 hour after reperfusion, vii) at two or more doses, viii) using a clinically-relevant mode of delivery, ix) using both histological and behavioral outcomes, and x) with outcomes at least 4 weeks after injury. Unfortunately, these criteria, as well as the ARRIVE (Animal Research: Reporting of *In Vivo* Experiments) criteria for design and reporting of preclinical studies, are still rarely applied today [224].

In addition to these criteria, any use of nanotechnology to transport therapeutic cargo must also include the necessary controls to account for the nanoparticle vehicle and any component of the nanoparticle that could result in toxicity, off-site effects, or added therapeutic benefit. For nanoparticles encapsulating a therapeutic, this typically involves adding treatment groups for the empty nanoparticle and the free drug. For therapeutics chemically linked to nanoparticles, controls might also need to include the nanoparticle with and without the linker chemistry. Further complicating pre-clinical studies, the use of nanoparticles to deliver therapeutics should decrease the necessary dose of the therapeutic; yet, this difference in dose between the therapeutic nanoparticle and the therapeutic in free form introduces an additional variable. Inevitably, the more multifunctional the nanoparticle delivery system, the more controls are needed to account for the potential effects of each component of that system.

While nanotechnologies might increase drug bioavailability and reduce dosing needs over the longer-term, initial preclinical studies often require more experimental groups. Meeting these needs increases costs substantially, especially when scaling nanotherapeutic formulation methods to test in multiple animal models with increasingly larger species. By not testing therapies in multiple animal models, including both rodent species and larger gyrencephalic animals (pigs, sheep, dogs, nonhuman primates, etc.) at multiple different time points in relation to the initial injury, the preclinical pipeline is unlikely to capture the heterogeneity of acute brain injury populations seen clinically. As preclinical work often focuses on reproducibility of injury to maintain statistical power whilst using small group sizes, without testing a therapy in the variety of settings outlined in the STAIR criteria, the likelihood of failure in the clinic will remain high [224]. Any anti-excitotoxicity therapy must achieve target site delivery at the right dose at the right timing of injury. Therefore, a robust preclinical pipeline including a combination of complementary models (Table 3.2) is paramount in the translation of nanotherapeutics for the treatment of excitotoxicity and oxidative stress.

3.10 Conclusions and looking forward

Delivering drugs that act specifically at diseased target sites at the appropriate dose at the right time is crucial for neurotherapeutics given the sensitivity and precision of brain function. Antioxidant intervention by scavenging injury-associated SOX and other ROS provides alleviation of multiple subsequent neuronal death pathways. Many studies have already shown the therapeutic potential of SOD-loaded nanoparticles or SOD-mimetic platforms, as well as various other antioxidants. However, despite promising inhibition of excitotoxic damage, further work needs to be performed to identify the ideal intervention point for therapeutic efficacy.

Understanding the mechanisms involved in excitotoxicity and oxidative stress can assist the nanoparticle drug delivery field in identifying promising points of intervention. Therapeutic development to inhibit ROS production can be guided by pinpointing the threshold at which ROS overwhelms antioxidant defenses and whether antioxidant uptake would enhance therapeutic effect. Determining whether excessive SOX elevation is primarily generated by NOX after glutamate receptor activation, by respiring mitochondria, or by xanthine oxidase after reperfusion, or whether the SOX source even matters, would better inform how to target the downstream pathology. However, it is imperative to remember that excitotoxicity is not the only disease hallmark at play. Inhibition of ROS in neuroinflammatory pathways could also assist in preventing delayed neurodegeneration that can arise days, months, or even years later [225, 226]. Since neuronal excitation and inflammation play roles in survival and growth, there is risk of injuriously over-inhibiting basal neuronal function or over-scavenging ROS and interrupting cell signaling [98, 225, 227, 228].

Preclinically, most antioxidant nanoparticle therapies achieved no greater than 60% reduction in infarct size on ischemia/reperfusion, HI brain injury, or TBI injury *in vivo*. It remains to be elucidated whether ~60% reduction is a practical limit, or whether additional strategies could further reduce damage. Therapeutic advances achieving greater than 60% infarct reduction could consist of increasing drug concentrations at injured sites, using targeting ligands for improved accumulation or cell-specific uptake at the target site, optimization of the timing of administration, or applying combination therapies with anti-inflammatory agents, pro-regenerative growth factors, or stem-cell based therapies. Furthermore, despite extensive preclinical evidence of antioxidant nanoparticle efficacy in acute brain injury, research must comply with STAIR and ARRIVE criteria before translation to clinical studies. Finally, though excitotoxicity is a primary mechanism of brain damage in stroke, TBI, and HI encephalopathy, the process may be present in the majority of neurological diseases [73]. Therefore, even when excitotoxicity is not the primary mechanism of pathology, neurological diseases more broadly could benefit from the development of antioxidant nanoparticle therapies to reduce neuronal injury.

In the next chapter, we demonstrate the utility of OWH models for inducing and studying neurological disease processes. Furthermore, we confirm the therapeutic efficacy of SOD in alleviating cell death and restoring healthy mitochondrial morphology to combat excitotoxicity.

Table 3.2. *in vitro* and *in vivo* models of excitotoxicity, stroke, TBI, and HI encephalopathy. For each model, the method in which the injury was created, the species that have been tested, the brain macrostructure (lissencephalic or gyrencephalic), the injury type, and the pros and cons of the model have been specified to enable identification of complimentary multi-species models to evaluate promising therapeutics. Abbreviations: AMPA, α-amino-3-hydroxy-5-methyl-4-isoxazolepropionic acid; BCCAO, bilateral common carotid artery occlusion; CCI, controlled cortical impact; CHIMERA, Closed-head impact model of engineered rotational acceleration; ICP, intracranial pressure; LPS, lipopolysaccharide; MCAO, middle cerebral artery occlusion; OGD, oxygen-glucose deprivation; Poly(I:C), polyinosinic:polycytidylic acid; TBI, traumatic brain injury; TLR, Toll-like receptor.

Setting	Target Disease	Model	Species	Brain type	Injury type	Pros	Cons
in vitro	Hypoxia-ischemia (general)	OGD	Rodents (rats, mice)	Organotypic brain slices	Global (whole brain/hemisphere slice) Focal (region-specific e.g. hippocampus)	Amenable to a wide range of biochemical assessments; Can perform electrophysiology and live cell imaging of subcortical structures; Fewer animals required for initial screening of therapies; Can maintain many cytoarchitectural features of the intact brain; Inflammatory stimuli can be added to media to target TLR4 (e.g. LPS), TLR3 (e.g. Poly(I:C)), and TLR1/2 (e.g. PAM3CSK4)	Specific culturing conditions affect slice stability and outcome assessments; Correlates with long-term or behavioral outcomes not possible
	Excitotoxicity (general)	Specific excitotoxins e.g.: NMDA Kainate MSG AMPA	Rodents (rats, mice)		Global (whole brain/hemisphere slice) Focal (region-specific e.g. hippocampus)		
	TBI	Traumatic slice culture injury	Rodents (rats, mice)		Global (e.g. rolled weight) Focal (e.g. targeted impact)		
in vivo	TBI	CCI	Rodents (rats, mice) Ferrets Pigs Nonhuman primates Sheep Rabbits	Lissencephalic Gyrencephalic	Focal	Controlled impact reduces variability in injury between animals; Different cortical areas can be targeted in larger animals; Ferret model allows for long-term assessments in gyrencephalic brain	Long-term outcomes limited in large animal models; Requires craniotomy; Focal injury is not representative of most closed-skull TBIs; Not amenable to repeat injuries; Ferret behavioral deficits may decrease over time

		Fluid percussion	Rodents (rats, mice) Cats Dogs Sheep Rabbits	Lissencephalic Gyrencephalic	Focal/Global	Controlled impact reduces variability in injury between animals; Different cortical areas can be targeted in larger animals; Fluid impact can reproduce effects of shearing stress; Recapitulates some aspects of systemic physiological changes after TBI	Long-term outcomes limited in large animal models; Requires craniotomy; Exogenous fluid in the skull cavity interferes with assessment of edema/ICP; Focal necrosis at site of impact is not representative of most closed-skull TBIs
		Closed skull impact (small animal)	Rodents (rats, mice)	Lissencephalic	Global	Etiology similar to many clinical TBIs (direct impact); Rodents are amenable to wide range of short- and long-term outcome assessments	High risk of skull fracture; May not replicate the axonal and white matter injuries seen clinically; High inter-animal and inter-laboratory variability
		Acceleration injury (large animal)	Sheep Pigs Nonhuman primates	Lissencephalic	Global	Etiology similar to many clinical TBIs (direct impact with rotational component); Gyrencephalic animals better replicate axonal and white matter injuries; Amenable to assessing systemic physiological and cerebrovascular/ICP changes	Long-term outcomes limited in large animal models; Antibody-based biochemical assessments more limited in large animals
		Blast injury	Rodents (rats, mice) Ferrets Rabbits Dogs Pigs	Lissencephalic Gyrencephalic	Global	Accurately replicates blast-style injuries including lung pathology and systemic inflammatory responses; Ferret model allows for long-term assessments in gyrencephalic brain	Requires significant technical expertise and equipment; Less relevant model for non-blast TBIs
		CHIMERA	Rodents (rats, mice) Ferrets	Lissencephalic Gyrencephalic	Global	Provides ability to standardize impacts in small animals across laboratories; Etiology similar to many clinical TBIs (direct impact with rotational component); Allows for multiple exposures; Amenable to a wide range of short- and long-term outcome assessments; Ferret model allows for long-term assessments in gyrencephalic brain	High risk of skull fracture with higher impact energies or repeat exposures; Less well validated compared to more-established TBI methodologies Ferret model has not been reproduced in multiple labs

	Stroke	MCAO	Rodent (rats, mice)	Lissencephalic	Focal	Can model both permanent and transient ischemia; Replicates major vessel occlusions seen clinically; Amenable to a wide range of short- and long-term outcome assessments; Well-validated histopathological and behavioral outcomes; Unaffected contralateral hemisphere can act as internal control for certain assessments	Must be performed in aged/diseased animals to ensure clinical relevance; Significant intra-operator variability in injury
		Photocoagulation or thrombosis	Rodents (rats, mice)	Lissencephalic	Focal	Models microvascular ischemia without altering surrounding tissue; Replicates effects of micro-infarcts; Can be used to examine effects in highly circumscribed areas	Does not model large vessel stroke; Typically restricted to the peripheral cortex; Does not result in behavioral deficits
		Multi-vessel ischemia	Rats	Lissencephalic	Focal	Models transient global ischemia (+/- permanent vessel occlusion); Amenable to a wide range of short- and long-term outcome assessments; Well-validated histopathological and behavioral outcomes	Must be performed in aged/diseased animals to ensure clinical relevance; Technically more challenging than focal stroke models
		BCCAO	Rodents (rats, mice)	Lissencephalic	Global	Models transient global ischemia; Amenable to a wide range of short- and long-term outcome assessments; Well-validated histopathological and behavioral outcomes	Must be performed in aged/diseased animals to ensure clinical relevance
	Neonatal stroke/HI encephalopathy	MCAO	Rodents (rats, mice)	Lissencephalic	Focal	Replicates major vessel occlusions seen clinically; Amenable to a wide range of short- and long-term outcome assessments; Well-validated histopathological and behavioral outcomes; Unaffected contralateral hemisphere can act as internal control for certain assessments	Must be used in age-appropriate animals to model neonatal stroke; Significant intra-operator variability in injury

		Unilateral hypoxia-ischemia (e.g. "Vannucci model")	Rodents (rats, mice)	Lissencephalic	Global (hemisphere)	Amenable to a wide range of short- and long-term outcome assessments; Well-validated histopathological and behavioral outcomes; Unaffected contralateral hemisphere can act as internal control for certain assessments; Can model inflammatory exposures via TLR4 (e.g. LPS), TLR3 (e.g. Poly(I:C)), and TLR1/2 (e.g. PAM3CSK4);	Injury pattern does not accurately replicate HIE pathology; High degree of intra-laboratory and inter-laboratory variability
		BCCAO	Ferrets Piglets Fetal sheep	Gyrencephalic	Global	Gyrencephalic models more accurately model clinical pathologies; Large animals are amenable to more clinically-relevant (several day) treatment times; Large animals support a range of clinically-relevant physiological monitoring; Can model inflammatory exposures via TLR4 (e.g. LPS), TLR3 (e.g. Poly I:C), and TLR1/2 (e.g. PAM3CSK4); Can model systemic illness if model incorporates systemic hypoxia/hypotension; Ferret and sheep models can be used to model multiple term/preterm equivalent ages	Ferret model currently less well validated compared to others; Ferret model has not been reproduced in multiple labs; Long-term outcomes limited in large animals (piglets, fetal sheep); Often limited by outcomes after 18-24h; Multi-day experiments in piglets require significant technical and personnel expertise

		Umbilical cord occlusion	Nonhuman primates Fetal sheep	Gyrencephalic	Global	Gyrencephalic models more accurately model clinical pathologies; Large animals are amenable to more clinically-relevant (several day) treatment times; Large animals support a range of clinically-relevant physiological monitoring; Can model inflammatory exposures via TLR4 (e.g. LPS), TLR3 (e.g. Poly I:C), and TLR1/2 (e.g. PAM3CSK4); Primate models are amenable to long-term technical imaging and behavioral assessments	Term primate model developmentally older than term human; Experiments in primates require significant technical and personnel expertise; Long-term outcomes limited in fetal sheep
	Cerebral Palsy	Intrauterine hypoxia	Rabbits Rodents (rat, mouse)	Lissencephalic	Global	Intrauterine LPS may be administered before/during hypoxia period to increase injury; Rodent model mimics early-life intra-uterine exposures/premature brain injury; Rodent model amenable to a wide range of short- and long-term outcome assessments; Rabbit model mimics a motor phenotype similar to cerebral palsy (not seen in rodent models)	Rabbit model not fully characterized with respect to pathological outcomes; Rodent behavioral deficits may decrease over time; High degree of mortality; Lissencephalic animals poorly model white matter injury seen in preterm infants Rabbit model has not been reproduced in multiple labs
		Intrauterine inflammation	Rabbits	Lissencephalic	Global	Largely inflammatory model - Intrauterine LPS administration as main injury stimulus; Mimics a motor phenotype similar to cerebral palsy (not seen in rodent models)	White matter focused injury so does not capture pathological changes in gray matter; Model has not been reproduced in multiple labs

	Cardiac Arrest	Cardiac arrest/resuscitation	Rodents (rats, mice) Dogs Pigs Nonhuman primates	Lissencephalic Gyrencephalic	Global	Clinically-relevant global injury model; Gyrencephalic models more accurately model clinical pathologies; Large animals are amenable to more clinically-relevant (several day) treatment times; Large animals support a range of clinically-relevant physiological monitoring; Rodent model amenable to a wide range of short- and long-term outcome assessments	Resuscitation can be technically challenging; Long-term outcomes limited in large animal models; Must be performed in appropriately aged/diseased animals to ensure clinical relevance
	Excitotoxicity (general)	Intracranial excitotoxin injection, for example: Kainate AMPA Ibotenate	Rodents (rats, mice)	Lissencephalic	Global (systemic) Focal (intracerebral)	Allows for mechanistic evaluation of excitotoxic pathophysiology; Can either be global (e.g. kainate-induced seizures) or focal (e.g. intracerebral ibotenate) injury; Amenable to a wide range of short- and long-term outcome assessments	Does not capture the wide-ranging pathological mechanisms encountered clinically

CHAPTER 4: Superoxide dismutase reduces monosodium glutamate-induced injury in an organotypic whole hemisphere brain slice model of excitotoxicity

4.1 Introduction

Elaborated in detail in Chapter 3.2, in excitotoxicity, excessive glutamate release over-activates neuronal postsynaptic glutamate receptors, causing sodium and calcium to flood into the neuron, generation of reactive oxygen species (ROS), and mitochondrial damage, ultimately initiating neuronal death processes [6-8]. Excitotoxicity can mediate cell death through both acute necrosis due to cell swelling upon uptake of sodium and chloride, and apoptosis involving calcium-induced downstream pathways [229, 230]. Combating excitotoxic cell death holds potential in ameliorating neuronal death in many neurological diseases.

As mentioned in Chapter 1.4, enzymes in their native form are actively studied for their role in managing neurological damage, specifically involving oxidative stress [30, 31, 161, 231]. Exogenously delivered antioxidant enzymes can help reestablish redox equilibrium within cells to mitigate excitotoxic brain damage. SOD has been widely studied and shows therapeutic potential in multiple disease models that exhibit excitotoxicity, including *in vitro* NMDA-induced neuronal cell culture, and *in vivo* MCAO models in rats [149, 150, 232, 233]. In this chapter, we use *ex vivo* organotypic whole hemisphere (OWH) brain slices as a high-throughput tool for monosodium glutamate (MSG)-induced excitotoxicity disease model development and therapeutic efficacy screening of SOD.

4.2 Results

4.2.1 Establishment of the MSG-induced excitotoxicity slice model

While OHC and cortical slices are widely used in the field, OWH slices have not previously been used for studying neurological disease [234]. Therefore, we determined the variation of OWH slice weight to support OWH reliability for quantitative analyses. Slice weight and LDH release after 1 day of culturing exhibited no significant difference based on slice location, as determined by the Kruskal-Wallace with Dunn's Multiple Comparisons test (Figure 4.1A-B; p>0.9999 for all). Slices were numbered 1 through 6 based on rostral to caudal slice location, starting with the first slice to contain a full hippocampal section. Slices exhibited a linear correlation in LDH release during the overnight rest period (r^2=0.5465), after 1D of culturing (r^2=0.6416), and during the combined rest + 1D Total (r^2=0.6733) as a function of slice weight (Figure 4.1C). After the slice preparation process of slicing, resting overnight, and culturing for 6h, non-treated slices exhibited healthy cellular morphology, as indicated by morphologically normal NeuN+ neurons and Iba1+ microglial cells. Representative images from the hippocampus are shown (Figure 4.1D-E).

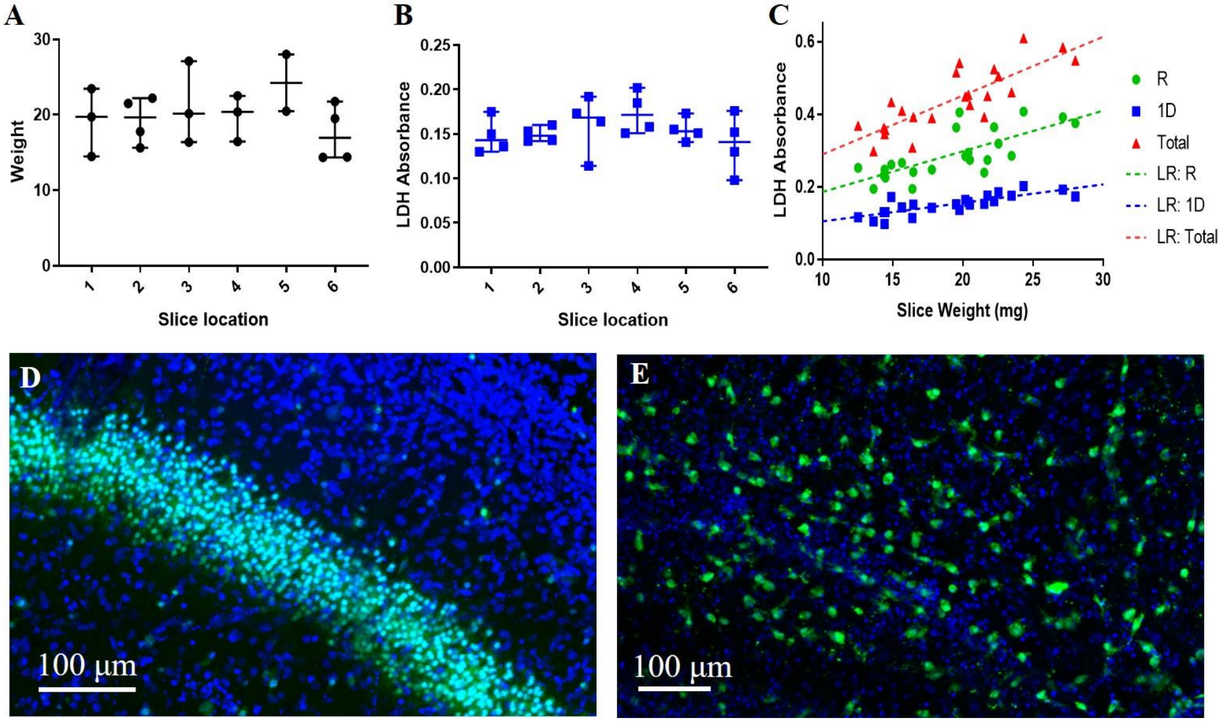

Figure 4.1: Establishment of the *ex vivo* whole hemisphere slice model. A) Brain hemisphere tissue weight based on slice location (n=2-4, median with 95% CI). B) LDH absorbance variability based on slice location (n=4, median with 95% CI). C) LDH absorbance of slices as a function of slice weight. R: overnight rest; 1D: after 24h; LR: linear regression. Cellular morphology of D) neurons stained with NeuN (green) and E) microglia stained with Iba+ (green) after 6h culturing. Slices were additionally stained with the nuclear marker, DAPI (blue). Scale bar is 100 µm.

Slices were incubated with a gradient of MSG concentrations to induce excitotoxicity (Figure 4.2A). 100 mM and 1000 mM MSG exhibited a significant increase in cell death compared to the NT control (p<0.0001 for both). Because 1000 mM MSG exhibited a greater increase in cytotoxicity than 100 mM MSG exhibited (p<0.0001; parametric unpaired t-test with Welch's correction), 1000 mM MSG was used as the concentration for LDH cytotoxicity studies, with all non-specified MSG conditions at 1000 mM. NT slices exhibited 5.04% cytotoxicity compared to

TX-induced complete cell death (Figure 4.2A). Because OHC slices are the most commonly used organotypic brain slice platform in the field, OWH slice responses to exposures were compared to OHC slice responses to establish OWH slices as a reliable and alternative model [234]. Compared to the respective condition of 1000 mM MSG, 1000 mM NaCl, and 100 ng/mL LPS, OHC and OWH slices exhibited no significant difference in cytotoxicity profiles (Figure 4.2B-C). 1000 mM MSG-treated slices elicited 8.28% greater cytotoxicity than 1000 mM NaCl-treated slices (*p*=0.0004). Figure 4.2D-E display representative photos of OHC slice cultures and OWH slice cultures, respectively.

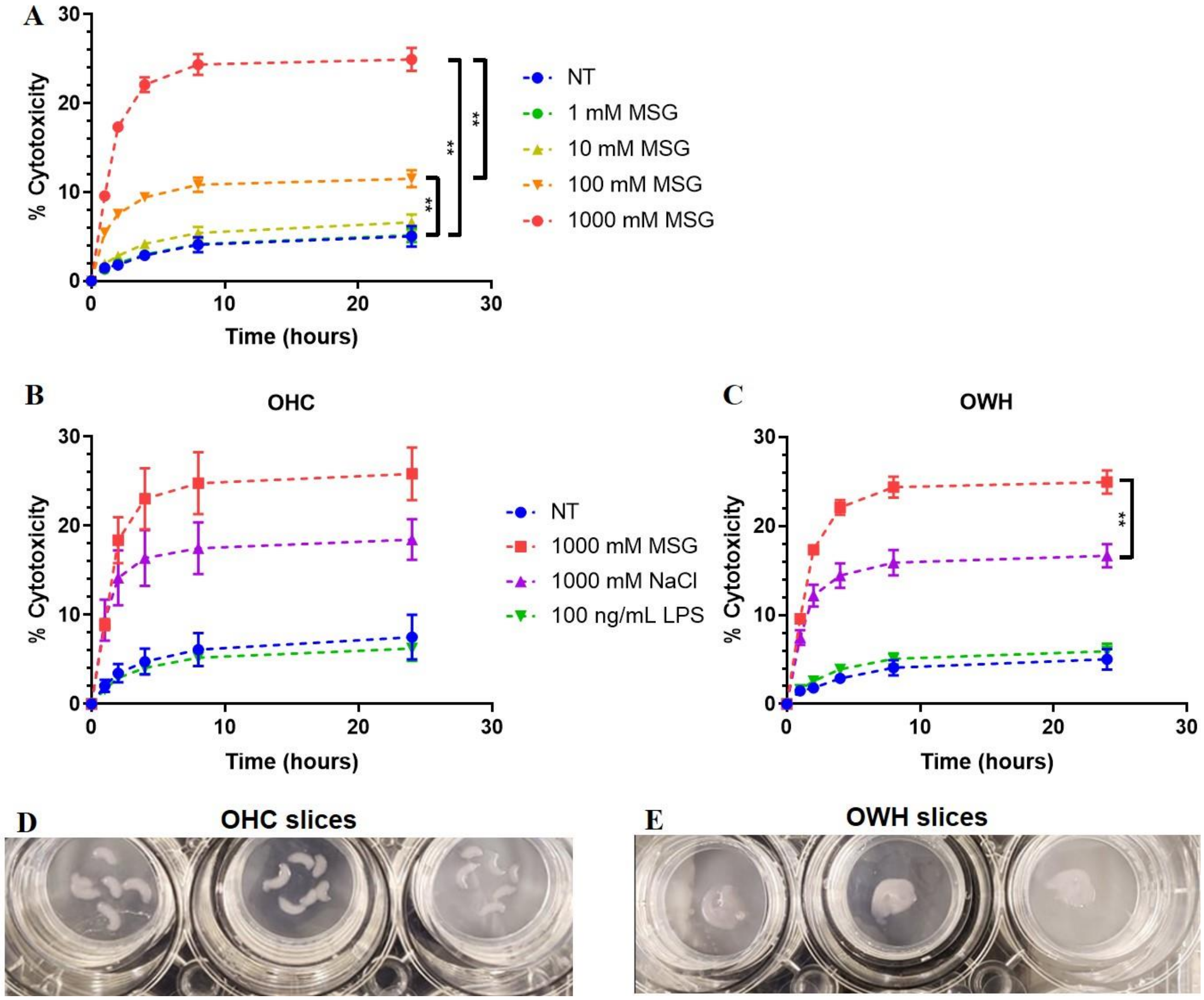

Figure 4.2: Establishment of the MSG-induced excitotoxicity slice model. Percent cytotoxicity was calculated from LDH absorbance for A) slices treated with gradient of MSG concentrations (n=18; mean ±

SEM), and B) OHC (n=3; mean ± SEM) and C) OWH (n=6 NaCl, LPS; n=18 NT, MSG; mean ± SEM) *ex vivo* slice cultures treated with various exposures, referenced to the 24h cumulative 1% TX LDH absorbance as 100%. Representative photos of D) OHC slice cultures and E) OWH slice cultures.

For RT-PCR analyses, 100 mM MSG and NaCl were used instead of 1000 mM due to the fact that at 1000 mM Na^+ concentrations, mRNA expression for all antioxidant enzymes was almost completely suppressed (Figure S4.1). After 3h incubation in NT, 100 mM MSG, 100 mM NaCl (hyperosmolar stress positive control), or 100 ng/mL LPS (inflammation positive control) conditions, and then 6h after exposure removal, slices were collected for RT-PCR analysis. MSG-treated slices exhibited a significant decrease in pro-inflammatory cytokine mRNA expression in comparison to NT and LPS-treated slices for IL-1β (NT: $p<0.0001$; LPS: $p=0.0097$), IL-6 (NT: $p<0.0001$; LPS: $p=0.0142$), and TNF-α (NT: $p=0.002$; LPS: $p=0.0354$) (Figure 4.3A). Furthermore, MSG-treated slices exhibited a fold-decrease in expression in comparison to NT slices for the excitation-related mRNAs EGR1 ($p=0.0122$) and nNOS ($p<0.0001$), and to NaCl-treated slices for EGR1 ($p=0.0112$) (Figure 4.3B). In comparison to NT slices, there were no significant differences in expression of antioxidant enzymes GCLM and HMOX1 for any treatment condition. MSG exposure elicited a significant decrease in SOD1 expression compared to NT ($p=0.0117$) and NaCl-treated slices ($p=0.0271$). 100 mM NaCl-exposed and 100 µM NMDA-exposed slices also exhibited a significant fold-decrease in pro-inflammatory mRNA expression (Figure S4.2). 100 µM NMDA-exposed slices showed no change in Dlg4, EGR1, or antioxidant enzyme mRNA expression, and a decrease in nNOS mRNA expression (Figure S4.3).

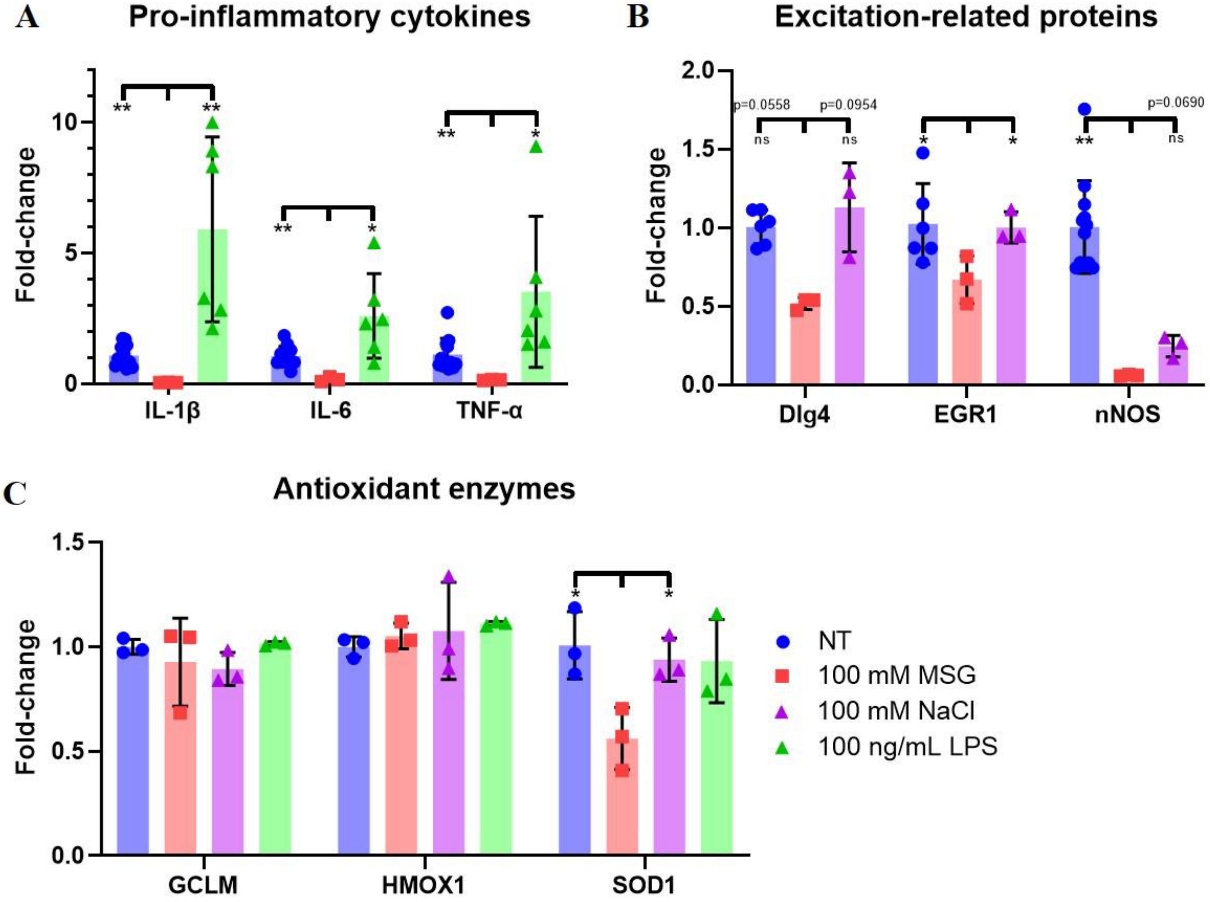

Figure 4.3: Fold-changes of mRNA markers for inflammation-, excitation-, and antioxidant-related proteins of NT, 100 mM MSG, 100 mM NaCl, and 100 ng/mL LPS slices at 6h. A) Fold-change of mRNAs for inflammatory cytokines of NT, MSG, and LPS slices (n=12 NT; n=3 MSG; n=6 LPS; mean ± SEM). B) Fold-change of mRNAs for excitation-related proteins of NT, MSG, and NaCl slices (n=6-12 NT; n=3 MSG and NaCl; mean ± SEM). C) Fold-change of mRNAs for antioxidant enzymes of NT, MSG, NaCl, and LPS slices (n=6 NT; n=3 MSG, NaCl, and LPS; mean ± SEM). ns: not significant.

4.2.2 Superoxide dismutase antioxidant effects on MSG-induced excitotoxicity

Application of SOD to MSG-induced excitotoxic OWH slices reduced cell death. Application of 0.01 mg and 0.1 mg SOD at 0h reduced toxicity to 43.72% (*p*=0.0304) and 23.99% (*p*<0.0001) respectively (Figure 4.4A), relative to 1000 mM MSG LDH release as 100% cytotoxicity. There was no significant difference between the NT (18.02%) and MSG + 0.1 mg SOD sample (*p*=0.5858). SOD's therapeutic effect was further explored based on timing of administration. Whether applied at 0h, 2h, or 4h after exposure to MSG, cytotoxicity was reduced compared to MSG without SOD treatment and reached a plateau by 24h (Figure 4.4B). Administration of SOD at 2h significantly decreased cytotoxicity to 59.39% (*p*=0.0005), while 4h treatment reduced toxicity to 79.24%, but not significantly (*p*=0.5092).

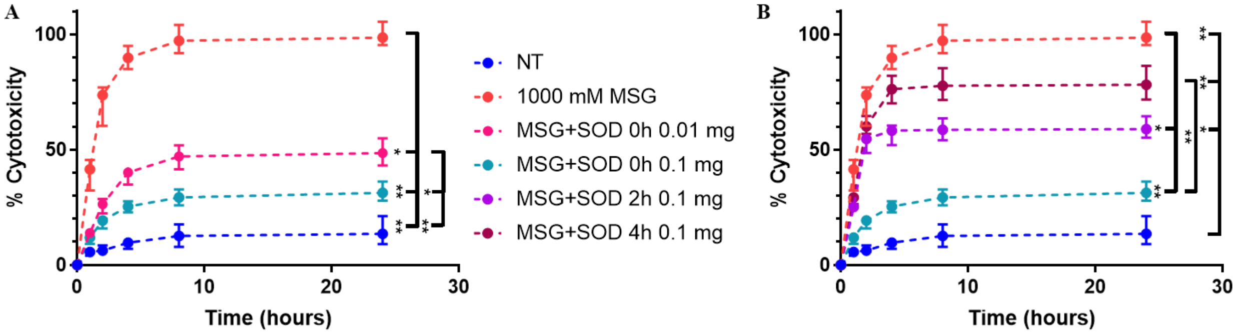

Figure 4.4: Therapeutic effect of SOD application on MSG-induced excitotoxic OWH slices. Percent cytotoxicity from LDH release was calculated with 24h cumulative LDH release from 1000 mM MSG-induced slices as 100%. A) MSG-induced slices treated with 0.01 mg and 0.1 mg SOD, and B) MSG-induced slices treated with 0.1 mg SOD at 0h, 2h, and 4h timepoints (n=18; median with 95% CI).

Furthermore, SOD treatment improved mitochondrial health. Figure 4.5A-C displays representative images of a cell from non-treated, 1000 mM MSG-treated, and 1000 mM MSG + 0.1 mg SOD-treated slices, where cell nuclei are stained with DAPI and mitochondria with MitoTracker Deep Red FM. Compared to control slices, MSG-treated slices exhibited extensive mitochondrial fission, yielding more numerous and smaller mitochondria. Upon application of 0.1 mg SOD at t=0h to the slice incubated with MSG from -3h to 0h, a return to NT mitochondrial morphology was observed, with larger and less numerous mitochondria in MSG+SOD-treated slices than the observed mitochondria incubated with MSG alone. To investigate the role of peroxynitrite-mediated toxic downstream products, 8-OHdG concentration in DNA extracted from NT, MSG, and MSG+SOD slices at the 6h timepoint was assessed. However, there was no significant difference in any of the three conditions, with concentrations of 9.770, 10.080, and 9.995 ng/mL respectively (Figure 4.5D). MSG did not elicit a significant increase in 8-OHdG concentration compared to NT slices (*p*=0.0895), and SOD did not significantly decrease 8-OHdG concentration compared to MSG alone (*p*=0.6767). Treatment of MSG slices with SOD did not significantly affect the mRNA expression of SOD1 compared to MSG (*p*=0.4303) (Figure 4.5E).

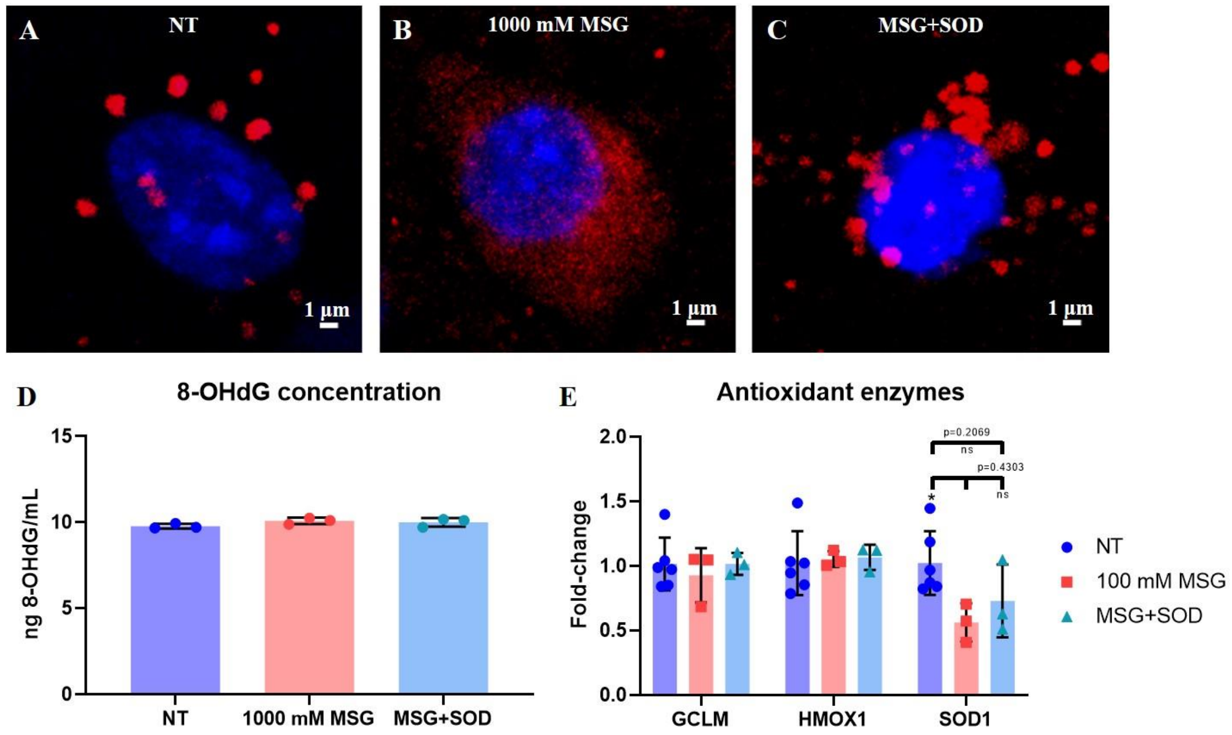

Figure 4.5: The exploration of mechanistic effects of SOD administration. Mitochondrial morphology of A) NT, B) 1000 mM MSG, and C) 1000 mM MSG with 0.1 mg SOD applied at t = 0h slices. Slices were stained with MitoTracker Deep Red FM (red) and DAPI (blue). Scale bar is 1 µm. D) Concentration of 8-OHdG in DNA extracted from NT, 100 mM MSG, and 100 mM MSG + 0.1 mg SOD/slice conditions at 6h as determined by 8-OHdG ELISA kit (n=3; mean ± SEM). E) Antioxidant enzyme mRNA fold-change expression at 6h for NT, 100 mM MSG, and 100 mM MSG + 0.1 mg SOD/slice (n=3-6; mean ± SEM).

4.3 Discussion

Glutamate excitotoxicity is a factor in the etiology of multiple neurological disorders, with multiple proposed pathways involved in inflicting damage. Here, we use an OWH brain slice model as a high-throughput tool for MSG-induced excitotoxicity disease model development and therapeutic efficacy screening. The *ex vivo* model has enabled us to isolate components of the naturally convoluted disease processes of glutamate excitation, inflammation, and hyperosmolar stress to better understand and treat excitotoxicity. Extracellularly administered SOD was effective in inhibiting cell death and restoring healthy mitochondrial morphology after exposure to MSG. However, based on early 8-OHdG concentrations, we also show that peroxynitrite-mediated DNA damage may not play a primary role in initiating excitotoxic cell death in this model.

Organotypic brain slice models enable more representative study of excitotoxicity, where glutamate and oxidative stress regulation involves multiple cell types [235, 236]. Even with improving technologies permitting *in vitro* co-cultures, culturing neurons, microglia, astrocytes, oligodendrocytes, pericytes, and brain microvascular endothelial cells together is still not feasible [237, 238]. Organotypic brain slices have commonly been dissected to culture the hippocampus, cortex, or striatum in isolation to study cell population subsets using single-cell resolution methods such as electrophysiology or IF [42, 239]. However, whole hemisphere cultures have not been popularized, missing the opportunity for performing bulk and regionally variable quantitative analyses. OWH slice culturing also utilizes a greater quantity of processable tissue from an individual brain than OHC slice culturing, reducing animal numbers needed for multi-modal tissue processing such as LDH, RT-PCR, and ELISA. Regardless of rostral to caudal position, the six coronal OWH slices containing the hippocampus used in our studies exhibit minimal variation in tissue weight, providing consistency for quantitative analyses (Figure 4.1). One P14 brain hemisphere can produce about six OWH slices containing the hippocampus before the enlargement of ventricles affects slice separation integrity. However, one OWH slice occupies approximately the same area as six OHC slices, requiring one whole hemisphere to obtain a comparable volume of hippocampal tissue (Figure 4.2C-D). Furthermore, OWH slices behave similarly in cytotoxicity response to MSG, NaCl, and LPS compared to OHC slices (Figure 4.2B-C).

We applied 1-1000 mM MSG to induce glutamate excitotoxicity (Figure 4.3A). Although presynaptic neuronal vesicles contain glutamate concentrations of ~70-200 mM [240], we selected 1000 mM MSG dose for LDH studies to examine a near-maximal cytotoxic response to MSG for therapeutic analyses. Additionally, we analyzed mRNA expression levels of slices after exposure to 100 mM MSG, 100 mM NaCl, 100 ng/mL LPS, or 100 μM NMDA. NaCl and NMDA exposures were performed to discern the effects of glutamate receptor activation as opposed to hyperosmolar sodium stress alone, while LPS treatment was performed to compare MSG excitotoxicity to a model of neuroinflammation [241, 242]. At 1000 mM salt concentrations the housekeeping gene GAPDH retained baseline expression levels, suggesting that mRNA transcript stability was maintained; however, expression of the target transcripts under investigation was reduced compared to NT slices for both MSG and NaCl treatment, preventing meaningful differentiation between the two exposures due to excitotoxicity mechanisms (Figure S4.1) [243, 244]. It is important to emphasize that all RT-PCR work was conducted with only female brain slices, and that there are significant gender differences in vulnerability to excitotoxicity, oxidative stress resistance, and mitochondrial function [245-248]. MSG-induced mRNA responses in males could vary greatly from the results obtained in females, and hence are not encompassed in this study, but need to be further explored.

As discussed in Chapter 1.3, excitotoxicity and inflammation are intimately intertwined *in vivo* where excitotoxicity can cause or be caused by inflammation, and both involve oxidative stress [99-101, 249]. After excitotoxic neuronal death, cells release pro-inflammatory cytokines and danger-associated molecular patterns that activate microglia and astrocytes [16-18]. Activated glia proliferate and migrate to damaged areas, and release molecules that exacerbate excitotoxicity, including NOX2-generated SOX, excitatory glutamate, and TNF-α [10, 20-24]. These interrelated pathologies make identification of the primary pathological players in excitotoxicity a complex process. By administering exogenous MSG, we induced excitotoxicity without the induction of pro-inflammatory cytokines. While LPS elicited upregulation of inflammatory IL-1β, IL-6, and TNF-α, MSG treatment significantly decreased expression for these same cytokines (Figure 4.3A). A similar decrease in pro-inflammatory cytokine expression was observed with exposure to 100 mM NaCl and 100 μM NMDA (Figure S4.2). The lack of inflammatory cytokine expression suggests glial NOX2-generated SOX may not be a requisite contributor to pathological SOX levels in excitotoxic death. The OWH model can therefore assist in isolating the primary excitotoxic core injury from the inflammatory penumbra observed *in vivo* [250].

One potential confounder of the MSG model is the associated sodium load. Although glutamic acid is found physiologically in its anionic form, exogenous sodium is also a relevant aspect of the model, as extensive sodium uptake leading to cell swelling and lysis is an important phenomenon in necrotic excitotoxic death [8]. Additionally, hyperosmolarity and excitotoxicity converge in pathological mechanisms through dysregulated calcium homeostasis and mitochondrial oxidative stress [251]. Morland *et al.* have shown that the replacement of chloride with the inert anion gluconate had no effect on sodium hyperosmolar neurotoxicity [252]. Therefore, comparison of MSG versus NaCl allows us to observe the effects of specifically the glutamate anion, where MSG exposure elicited greater cytotoxicity than NaCl exposure (Figure 4.2C). Hyperosmolar conditions result in the uptake of anionic osmolytes including chloride, glutamate, and taurine, to minimize water efflux and cell shrinkage [252]. At 0h, upon removal of 1000 mM MSG or NaCl and return to normo-osmolar conditions, cells then efflux accumulated osmolytes including glutamate, leading to greater extracellular glutamate levels conducive to further excitotoxicity. It reasonably follows that the presence of excess glutamate in MSG-treated slices could lead to exacerbated uptake and subsequent efflux of glutamate back into the extracellular space for increased toxicity.

Upon oxidative stress due to injury or inflammation, the antioxidant response element known as nuclear factor erythroid 2-related factor 2 (NRF2) translocates to the nucleus to upregulate the transcription of HMOX1 and GCLM antioxidants [253]. The OWH slices are already in a state of acute oxidative stress due to injury in the tissue chopping process, which overnight resting partially mitigates [241]. HMOX1 and GCLM expression in MSG slices exhibited no significant difference from the NT condition (Figure 4.3C). Under oxidative stress conditions, many transcriptional pathways downregulate to prioritize only survival-related proteins [253, 254]. The retention of NRF2 target expression, but not pro-inflammatory mRNA expression, suggests that MSG mediates damage primarily through oxidative stress independent of inflammation. Further studies are needed to determine whether microglial depletion from MSG injury accounted for the lack of inflammation. However, SOD1 mRNA expression decreased for 100 mM MSG-treated slices compared to NT and 100 mM NaCl-treated slices (Figure 4.3C). The severe MSG-induced oxidative stress could upregulate activating factor 1 (AP-1) and AP-2, repressing SOD1 mRNA expression [30, 255, 256].

The 100 mM MSG slices reduced expression of excitation-related transcripts, decreasing EGR1 mRNA expression compared to NT and NaCl-treated slices, and decreasing nNOS expression compared to NT slices (Figure 4.3B). EGR1 is an immediate early gene (IEG) indicator of excitation activity, and Dlg4 is a NMDAR-associated synaptic scaffolding protein that recruits nNOS to produce NO [29, 257]. OWH MSG exposure potentially preferentially damaged neurons compared to other cell populations [258]. The MSG-induced oxidative stress could interfere with neuronal RNA stability and transcription [243, 259-261], or selectively increase neuronal death, ultimately reducing the neuronal population contributions to mRNA transcripts of excitation-related proteins. However, *in vivo* studies show increases in expression of nNOS and other IEGs after excitotoxic insults [262-265]. The discrepancy could be explained by the direct exposure of OWH slices to MSG throughout the entire slice, as opposed to exposure only at the localized primary insult *in vivo*. The primary insult elicits increased excitatory activity among neighboring neurons, and hence could explain overall nNOS and IEG mRNA upregulation *in vivo* [262]. The definitive cause of reduced mRNA expression of excitation-related proteins in MSG-exposed OWH slices requires further exploration.

Despite the severe oxidative stress environment and decreased SOD1 mRNA expression due to MSG exposure, we found that exogenously applied SOD provided a neuroprotective effect against MSG-induced excitotoxicity. Furthermore, the decrease in cytotoxicity was directly dependent on the timing of SOD administration and elicited a plateau in cytotoxicity whether administered at 0h, 2h, or 4h (Figure 4.4A-B). This further confirms the efficacy of SOD against excitotoxicity, supporting previous *in vitro* and *in vivo* studies of SOD amelioration of excitotoxic death [149, 233, 266]. Although administered extracellularly, SOD effectively inhibits SOX toxicity, suggesting that extracellular delivery is sufficient for inhibition, as opposed to requiring targeted cellular uptake and mitochondrial localization [81]. For potential clinical translation of SOD for neurological disorders, it is important to note that macromolecular enzymes are prone to protease degradation and fail to cross the blood-brain barrier. Therefore, SOD would require assistance in drug delivery to reach the disease site through the use of nanoparticles or alternative approaches, before its exogenous therapeutic effect in brain tissue could be realized [69, 131]. The therapeutic effect of SOD on MSG-induced excitotoxicity was further confirmed by observing mitochondrial morphology (Figure 4.5A-C). It is important to note that not all NT and MSG+SOD mitochondria were non-fragmented, and not all MSG mitochondria were fragmented, but Figure 4.5A-C represents the large majority of cells imaged. During oxidative stress, mitochondria undergo extensive fission to isolate damaged portions of the mitochondria, resulting in more numerous and smaller mitochondria as seen in MSG-treated slices (Figure 4.5B) [267]. By scavenging SOX, SOD reduces mitochondrial damage, reducing extensive fission to yield mitochondria resembling those of NT cells (Figure 4.5C). Interestingly, the SOD reaction produces 50% molar concentrations of H_2O_2, which does not appear to affect overall cell death in our model.

Studies have shown that elevated SOX production from mitochondrial respiration in combination with elevated NO production generates the highly reactive species peroxynitrite [89]. Peroxynitrite reacts with biological molecules causing protein, lipid, and nucleic acid oxidative and nitrosative damage [89]. However, we observed no significant changes in 8-OHdG, a peroxynitrite-mutated DNA product, concentration at 6h (Figure 4.5D). This suggests that peroxynitrite may not hold a primary role in the early pathogenesis of excitotoxicity. Supporting this idea, Choi *et al.* demonstrated that nNOS and NOX2 inhibition prevented NMDAR hypersensitivity but peroxynitrite inhibition did not, suggesting peroxynitrite is downstream of the cause of excitatory dysfunction [268]. The absence of a positive control for 3-NT downstream products is a limitation of our analysis. Future work could confirm the lack of a role for peroxynitrite in initial excitotoxic injury with a model that differentially expresses 8-OHdG at later timepoints beyond 6h. Despite SOD providing a neuroprotective effect in reducing cell toxicity, SOD did not restore SOD1 mRNA expression. However, SOD1 expression was no longer significantly different from NT slices for SOD-treated slices (Figure 4.5E). We suspect SOD interrupts the pathological pathway towards cell death, rather than inhibiting initial excitation pathways when applied 3 hours after MSG treatment. It remains possible that earlier SOD administration could more effectively inhibit MSG pathology and SOD1 mRNA downregulation. Whether exogenous addition of SOD revitalizes native antioxidant systems requires further exploration.

4.4 Conclusion

Using OWH brain slice models, we can bypass the many obstacles associated with drug delivery to the brain to reliably screen therapeutics in high-throughput fashion prior to *in vivo* evaluation. OWH brain slices exhibit healthy cellular architecture after culture and respond to exposures similarly to widely studied OHC slices, while reducing animal numbers for quantitative analyses. With RT-PCR, distinguishing glutamate excitotoxicity from inflammation and sodium hyperosmolarity enables us to better understand primary pathological mechanisms in excitotoxicity. SOD administration reduced cytotoxicity and restored healthy mitochondrial morphology. Supported by the absence of increased 8-OHdG residues upon MSG treatment, peroxynitrite-mediated damage may not play a primary role in initial excitotoxic damage. SOD can help inhibit cell death, but a fully effective therapeutic strategy could benefit by utilizing a combinatorial therapy with another drug that targets excessive neuroinflammation, and delivery within a nanoparticle platform. Altogether, SOD is a very promising enzyme therapeutic for combating excitotoxicity in a plethora of neurological diseases.

In the next chapter, we optimize our polymeric nanoparticle formulation, comparing the enzyme loading and protection of nanoparticles formulated via the double emulsion (DE) and nanoprecipitation (NPPT) methods. We further apply OWH models as a screening tool for nanoparticle biocompatibility in various biologically relevant microenvironments.

CHAPTER 5: Enzymatic protection and biocompatibility screening of enzyme-loaded polymeric nanoparticles for neurotherapeutic applications.

5.1 Introduction

Therapeutic enzymes are of special interest due to their precise catalytic functions, but oral and intravenous administration of free enzymes have had limited success due to proteolytic degradation and poor brain biodistribution [269]. Attempts to overcome these issues include administering greater drug concentrations that exceed proteolysis rates, and covalent conjugation of ligands to the enzyme for enhanced targeting [48, 270, 271]. However, even if enzymes survive the journey into and through systemic circulation, 100% of large therapeutic molecules fail to cross the intact BBB [131]. Altogether, these obstacles demand the use of drug-carrier vehicles such as polymeric PLGA-PEG nanoparticles to effectively deliver enzyme therapeutics. As discussed in Chapter 1.6 and 3.4, polymeric nanoparticles have been extensively researched for drug delivery applications to the CNS due to their ability to overcome physiological barriers including the BBB and to favorably alter drug metabolism and clearance kinetics [48, 272-275]. For PLGA-PEG block copolymer, the most common nanoparticle formulation approaches for hydrophilic cargo encapsulation are the double emulsion (DE) and the nanoprecipitation (NPPT) methods [40, 276].

Despite the fact that PLGA-PEG nanoparticles are known to be biocompatible and protective of enzymatic cargo, similar formulation conditions do not guarantee the same advantageous characteristics. Thus, each distinct formulation should be appropriately screened to ensure enzyme protection and biocompatibility in various environments representative of the *in vivo* landscape. Failure to do so could lead to an enzyme-encapsulating nanoparticle failing clinical trials due to ineffective enzyme protection, or worse, due to inadvertent toxicity exacerbating the disease outcome. Here, we compare DE and NPPT nanoparticle formulations and show varying efficacy in protecting enzymatic activity. Using OWH brain slice models of neurological disease as a tool for toxicity screening of nanoparticle formulations, we discovered the toxicity of PLGA-PEG DE nanoparticles formulated with dichloromethane (DCM) organic solvent on excitotoxicity-induced brain environments. We further utilized the excitotoxicity-induced OWH model to screen and ultimately identify alternative formulation conditions that exhibit biocompatibility and retain enzymatic protection.

5.2 Results and Discussion

5.2.1 Formulation optimization for nanoparticle enzyme activity and protection

With the end goal of maximizing therapeutic effect, it is important to optimize polymeric nanoparticle formulations to maximize drug loading. We first formulated catalase-loaded nanoparticles with the DE method with various sonication times or the NPPT method, with CHA or PVA surfactants. For the DE method, sonication times of 15s, 30s, and 60s sonication times yielded similar sized nanoparticles for both CHA (58.4-70.8 nm) and PVA (109.8-113.3 nm) surfactants (Figure 5.1A-B), while 1s sonication resulted in overall much larger diameters. The NPPT method also yielded larger nanoparticles than the 15-60s double emulsion nanoparticles. Importantly, except for the 1s DE and PVA NPPT conditions, all nanoparticle formulations were sub-114 nm in size. All nanoparticle formulations exhibited a near-neutral ζ-potential between 0 and -10 mV, as expected with a dense PEG coating (Figure 5.1C-D). Nanoparticles with a sub-114 nm size and neutral surface charge exhibit rapid diffusion in the brain parenchyma [41, 130, 140].

We used catalase as a model enzyme for studying enzyme activity and degradation within the nanoparticle. CHA 30s sonication formulations exhibited an inverted U trend with a significantly greater catalase activity of 45.19AU compared to all other CHA DE formulation activities (Figure 5.1E-F). 30s sonication also exhibited the highest catalase activity of 80.14AU for PVA formulations, compared to the 1s, 60s, and NPPT activities. The active/total protein ratios present in the CHA nanoparticle formulations was also measured (Figure S5.1). 30s conditions had the highest active/total protein ratio among the DE conditions, but there was only a significant difference between 1s and 30s DE conditions (p=0.041). Interestingly, the active/total protein ratio followed a similar trend as the total activity trend for the CHA nanoparticle formulations. It is likely that a minimum threshold sonication time is requisite to provide enough mixing to encapsulate enzyme and produce stable nanoparticles, with 1s formulations containing more aggregates and a larger diameter. On the other hand, excessive sonication time at 60s can lead to further enzyme deactivation due to more interaction time with high energy sonication waves and organic/aqueous interfaces. Scanning electron micrographs of 1s, 30s, and NPPT nanoparticles (Figure 5.1G-I) confirm nanoparticle sizes as presented in Figure 5.1A. Interestingly, the surface of the NPPT nanoparticles appears to be rougher than the DE formulations.

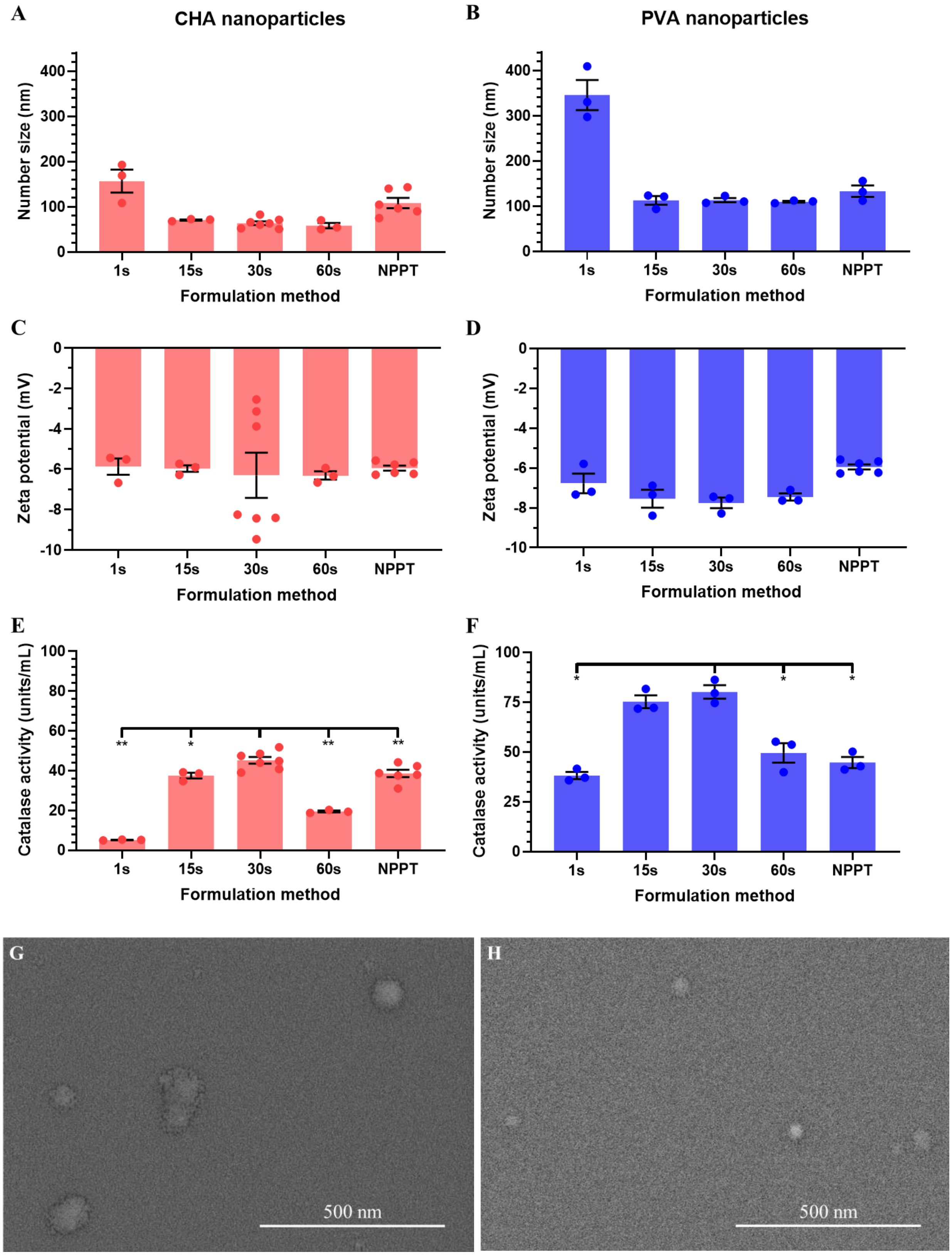
A
CHA nanoparticles
Number size (nm)
0
100
200
300
400
1s
15s
30s
60s
NPPT
Formulation method
B
PVA nanoparticles
Number size (nm)
0
100
200
300
400
1s
15s
30s
60s
NPPT
Formulation method
C
Zeta potential (mV)
0
-2
-4
-6
-8
-10
1s
15s
30s
60s
NPPT
Formulation method
D
Zeta potential (mV)
0
-2
-4
-6
-8
-10
1s
15s
30s
60s
NPPT
Formulation method
E
Catalase activity (units/mL)
0
20
40
60
80
100
**
*
**
**
1s
15s
30s
60s
NPPT
Formulation method
F
Catalase activity (units/mL)
0
25
50
75
100
*
*
*
1s
15s
30s
60s
NPPT
Formulation method
G
500 nm
H
500 nm

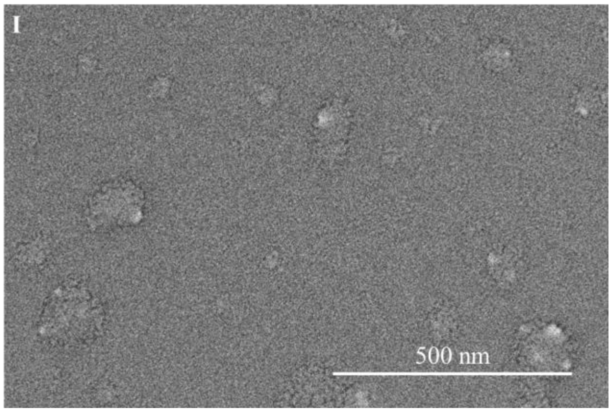

Figure 5.1: Characteristics of nanoparticles formulated with DE and NPPT methods. A) CHA and B) PVA nanoparticle number mean sizes, C) CHA and D) PVA nanoparticle ζ-potentials, and E) CHA and F) PVA nanoparticle catalase activities were determined for 1s, 15s, 30s, and 60s DE and NPPT formulations (n=7 CHA DE 30s, n=6 CHA NPPT, n=3 all others). Data are reported as mean ± SEM. Scanning electron micrographs of nanoparticles formulated with CHA under the conditions of G) 1s DE, H) 30s DE, and I) NPPT.

Bilati et al. previously characterized protein loading via DE and NPPT methods but did not assess enzymatic activity [277], which is crucial for determining nanoparticle protection of encapsulated protein. Catalase-loaded nanoparticle formulations were subsequently used for the catalase activity stability studies. We performed a catalase activity stability study over several hours in biologically relevant media at 37°C for the catalase-loaded 30s sonication DE and NPPT nanoparticles as well as for free catalase (Figure 5.2). In the presence of 0.2 wt% pronase, a mixture of proteases from *Streptomyces griseus*, catalase-DE-nanoparticle activity was significantly greater than free catalase activity for all timepoints after t=0h (Figure 5.2A). After 2h of incubation with pronase, free catalase showed almost no measurable activity (2.9%), while CHA and PVA catalase-nanoparticles made via the 30s sonication DE method retained 75.7% and 18.6% activity, respectively. Even after 24h, CHA and PVA catalase-nanoparticles had 6.1% and 7.5% activity, respectively. The CHA DE retained significantly greater activity than the PVA DE activity at 1h, 2h, 4h, and 8h. NPPT with either CHA or PVA surfactant however provided no extension in catalase activity, decreasing to 5.4% (p=0.278) and 2.5% (p=0.639) activity, respectively, compared to free catalase activity of 2.1% at 4h (Figure 5.2B). These results suggest that the high energy mixing during DE encapsulates catalase into the matrix interior of the nanoparticle where proteases cannot immediately penetrate. The lack of high energy mixing results in only surface-associated catalase for the NPPT formulation where the enzymes are still accessible and vulnerable to protease degradation. Our work is the first to exhibit this protective effect with polymeric nanoparticles under 100 nm in the presence of pronase, as well as in serum representative of degradative *in vivo* circulation conditions.

In the physiologically representative environment of serum extracted from rat blood, free catalase deactivated to 46.9% activity after incubating for 6h in serum, while catalase loaded within CHA nanoparticles exhibited no enzyme deactivation after 6h (Figure 5.2C). Perhaps surprisingly, free catalase underwent no significant difference in activity between 0h and 2h (p=0.131) or 24h (p=0.136) when incubated with OWH slices directly (Figure 5.2D), despite the documented presence of proteases in the brain [278-280]. The peculiar but insignificant increase in catalase activity at 2h and 24h could be from improvement of the ox/redox environment with exogeneous catalase addition, increasing native catalase or glutathione peroxidase functions, obscuring the activity of exogenous catalase alone [281]. However, exploring the relative contributions of native hydrogen peroxide scavenging versus exogenous catalase addition was outside the scope of this chapter. The significant difference in catalase stability of free versus DE nanoparticle-encapsulated conditions in pronase and serum exemplifies the promising delivery improvements imbued by DE polymeric nanoparticles for enzyme delivery. PLGA nanoparticles are widely studied for protein delivery, with the assumption that they are cargo-protective, but here we find that protective abilities are formulation method-dependent, with NPPT providing no protection for the enzyme assessed in this study.

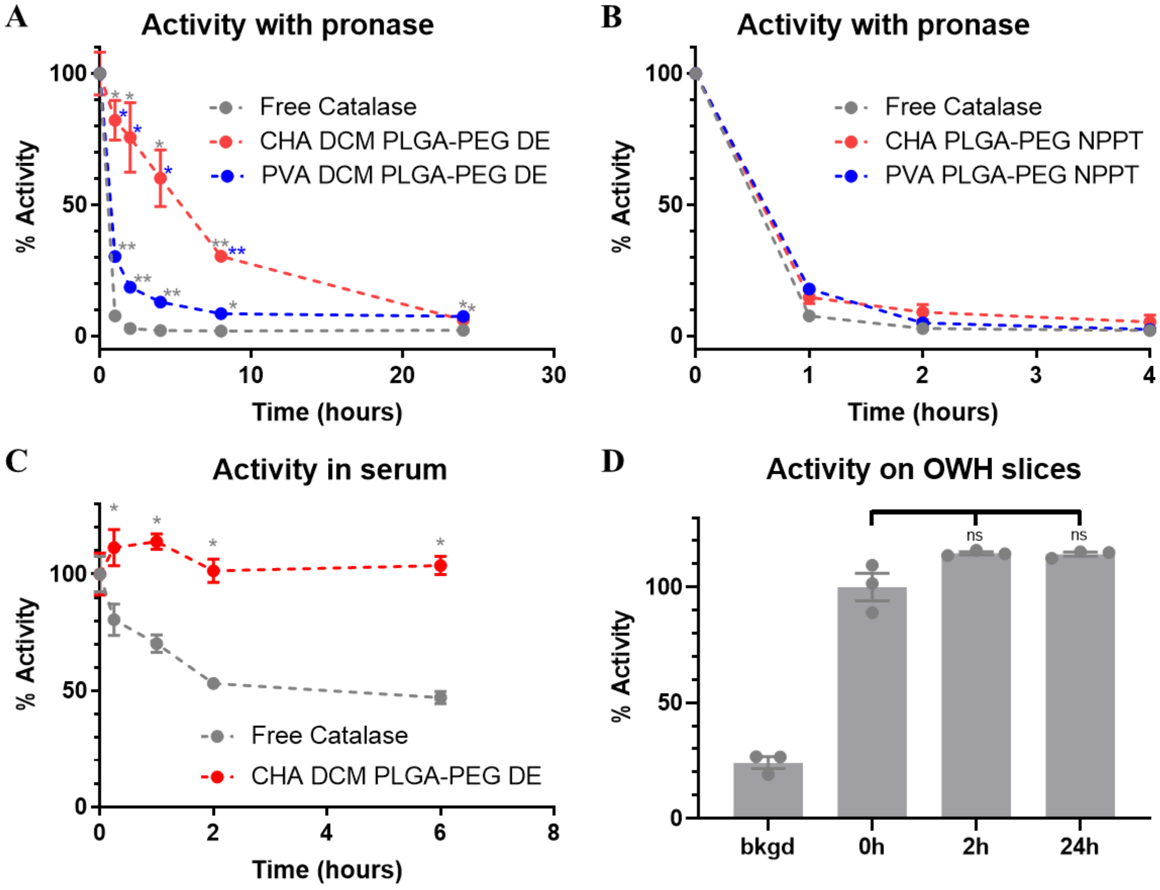

Figure 5.2: Nanoparticle protection of catalase activity in biologically relevant environments. Free catalase and catalase-loaded nanoparticle activity in PBS with 0.2 wt% pronase at 37°C A) over 24h for DE nanoparticles, and B) over 4h for NPPT nanoparticles. The same free catalase curve is presented for A) and B) for comparison. C) Free catalase and CHA DE nanoparticle activity over 6h in rat serum at 37°C. For A) – C), at the respective timepoint, a grey * denotes compared to free catalase and a blue * denotes compared to PVA DE NP. D) Free catalase activity when incubated with OWH NT slices at 37°C. The condition bkgd represents the baseline catalase activity of the OWH slice without exogeneous catalase addition. The sample numbers are the following: n=9 PVA DE NP in pronase conditions, n=5 CHA NPPT NP in pronase conditions, n=3 all other data. Data are reported as mean ± SEM.

5.2.2 Biocompatibility screening of DE and NPPT nanoparticles

Nanoparticle therapeutics administered to the brain encounter various neurological disease environments ranging from healthy tissue to regions of neuroinflammation or excitotoxicity [282]. To mimic these various environments, we used OWH slice models of LPS-induced neuroinflammation, MSG- and OGD-induced excitotoxicity, and NT healthy tissue. These OWH slices primarily consist of neurons, microglia, astrocytes, oligodendrocytes, pericytes, and endothelial cells, encompassing almost of the major cell types in the brain [234] – importantly these cells exist within a 3D architecture that mimics the *in vivo* local environment. We assessed the biocompatibility of non-loaded blank nanoparticle (bNP) formulations made via DE or NPPT with CHA as the surfactant on the four OWH slice models. On NT and LPS-exposed slices, neither DE nor NPPT bNPs significantly increased cytotoxicity (Figure 5.3A-B). However, despite displaying the greatest protection of catalase activity, DCM PLGA-PEG DE bNPs significantly increased toxicities on the OWH models of excitotoxicity. For MSG-exposed slices there was a significant 1.7-fold increase in cytotoxicity upon addition of DE bNPs, while NPPT bNPs exhibited no effect (Figure 5.3C). OGD-exposed slices exhibited the same trend with only DE bNPs significantly increasing cytotoxicity 1.4-fold (Figure 5.3D). The 3h OGD-exposed slices elicited 1.8-fold lower cytotoxicity compared to 1000 mM MSG-exposure induced cytotoxicity. Similar to the need to assess each specific nanoparticle formulation for enzymatic cargo protection, thorough screening for biocompatibility is necessary for each formulation variant to ensure that a given nanoparticle formulation is not toxic in healthy or diseased environments. Figure 5.3E-G show immunofluorescence images of neurons for NT, 1000 mM MSG, and MSG + toxic DE bNPs, respectively. MAP2 colocalization with PI provides a qualitative assessment of neuronal viability. While MAP2+ neurons had cell nuclei lacking PI colocalization with an extended soma, 1000 mM MSG with or without DE bNP application resulted in dying or dead neurons with PI+ cell nuclei and a retracted soma. MSG + DE bNP application further reduced neuronal soma area compared to neurons exposed to MSG alone.

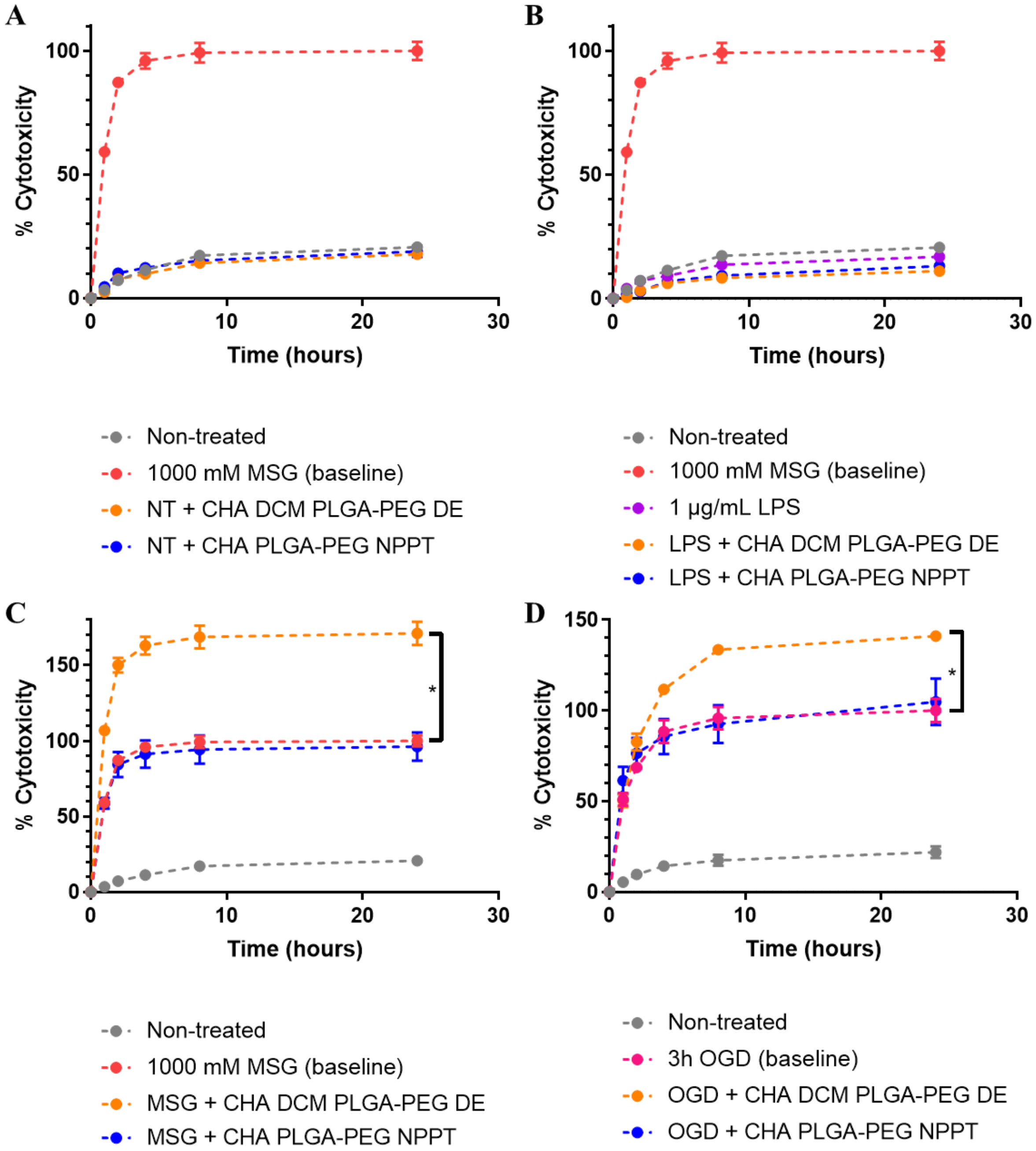
A
% Cytotoxicity
100
50
0
0
10
20
30
Time (hours)
Non-treated
1000 mM MSG (baseline)
NT + CHA DCM PLGA-PEG DE
NT + CHA PLGA-PEG NPPT
B
% Cytotoxicity
100
50
0
0
10
20
30
Time (hours)
Non-treated
1000 mM MSG (baseline)
1 µg/mL LPS
LPS + CHA DCM PLGA-PEG DE
LPS + CHA PLGA-PEG NPPT
C
% Cytotoxicity
150
100
50
0
0
10
20
30
Time (hours)
*
Non-treated
1000 mM MSG (baseline)
MSG + CHA DCM PLGA-PEG DE
MSG + CHA PLGA-PEG NPPT
D
% Cytotoxicity
150
100
50
0
0
10
20
30
Time (hours)
*
Non-treated
3h OGD (baseline)
OGD + CHA DCM PLGA-PEG DE
OGD + CHA PLGA-PEG NPPT

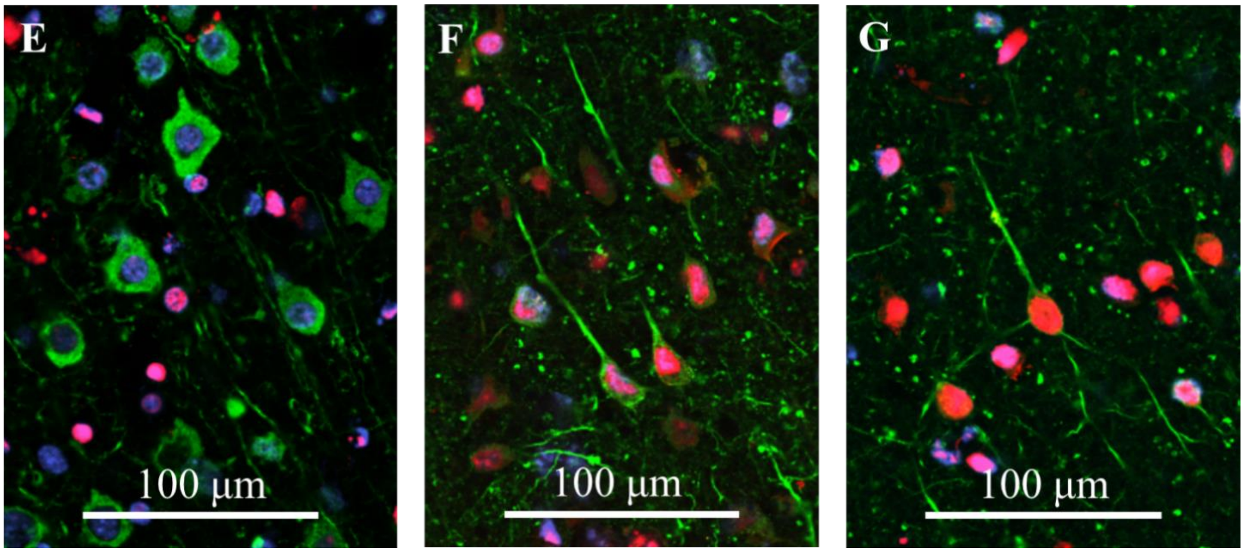

Figure 5.3: Biocompatibility assessment of blank DE and NPPT nanoparticles. Percent cytotoxicity of A) NT, B) LPS-exposed, C) MSG-exposed, and D) OGD-exposed slices after bNP application. For A) – C), cytotoxicity values are referenced to 1000 mM MSG as the 100% cytotoxicity baseline, and the NT and 1000 mM MSG curves are identical. For D), cytotoxicity values are referenced to 3h OGD as the 100% cytotoxicity baseline (n=3). 100% cytotoxicity does not indicate that all cells are dead, hence some values above 100%. Data are reported as mean ± SEM. Immunofluorescence of all cell nuclei stained with DAPI (blue), dead cell nuclei stained with PI (red), and neurons stained with MAP2 (green) for E) NT, F) 1000 mM MSG, and G) MSG + toxic DE bNP slices at t = 24h. Scale bars are 100 μm.

We next sought to determine the cause of toxicity on MSG-exposed slices, starting with assessing the biocompatibility of the surfactants. While 1% PVA had no significant effects on cytotoxicity on NT (p=0.394) or MSG-exposed slices (p=0.419), 1% CHA caused a 5.2-fold increase for NT (p<0.001), and 3.0-fold increase for MSG-exposed slices (p=0.001) (Figure 5.4A). However, upon evaluating the effects of nanoparticles made with PVA surfactant we observed similar toxicity to that induced by CHA nanoparticles. PVA NPPT nanoparticles were inert, while PVA DE nanoparticles were highly toxic (p=0.005) (Figure 5.4B). In attempt to narrow down the toxic component of the system, we further assessed toxicity of control formulations and found that nanoparticles composed of PLGA polymer with PVA surfactant (p=0.072), as well as sonicated PEG in DI/DCM and no surfactant elicited no change in toxicity (p=0.685) (Figure 5.4C). PVA PLGA-PEG bNPs emulsified in EtAc instead of DCM as the organic solvent also did not significantly increase cytotoxicity on MSG-exposed slices (p=0.188) (Figure 5.4C). In the presence of pronase however, similar to other PVA formulations, PLGA with DCM and PLGA-

PEG with EtAc formulations failed to provide any extension of catalase activity (Figure 5.4D). Figure S5.2 displays the size, ζ-potential, and catalase activity characteristics of PLGA with DCM and PLGA-PEG with EtAc formulations. Thus, we concluded that the specific conditions of sonicated PLGA-PEG polymer dissolved in DCM organic solvent formulates nanoparticles with high toxicity on excitotoxic brain tissue. DCM is popularly used in nanoparticle emulsion methodologies highlighting the importance of awareness of and screening for unintentional toxicity [276, 283, 284]. Furthermore, PEG toxicity has previously been reported upon sonication of Pluronic surfactants that contain PEG chains during the synthesis of multi-walled carbon nanotubes [285].

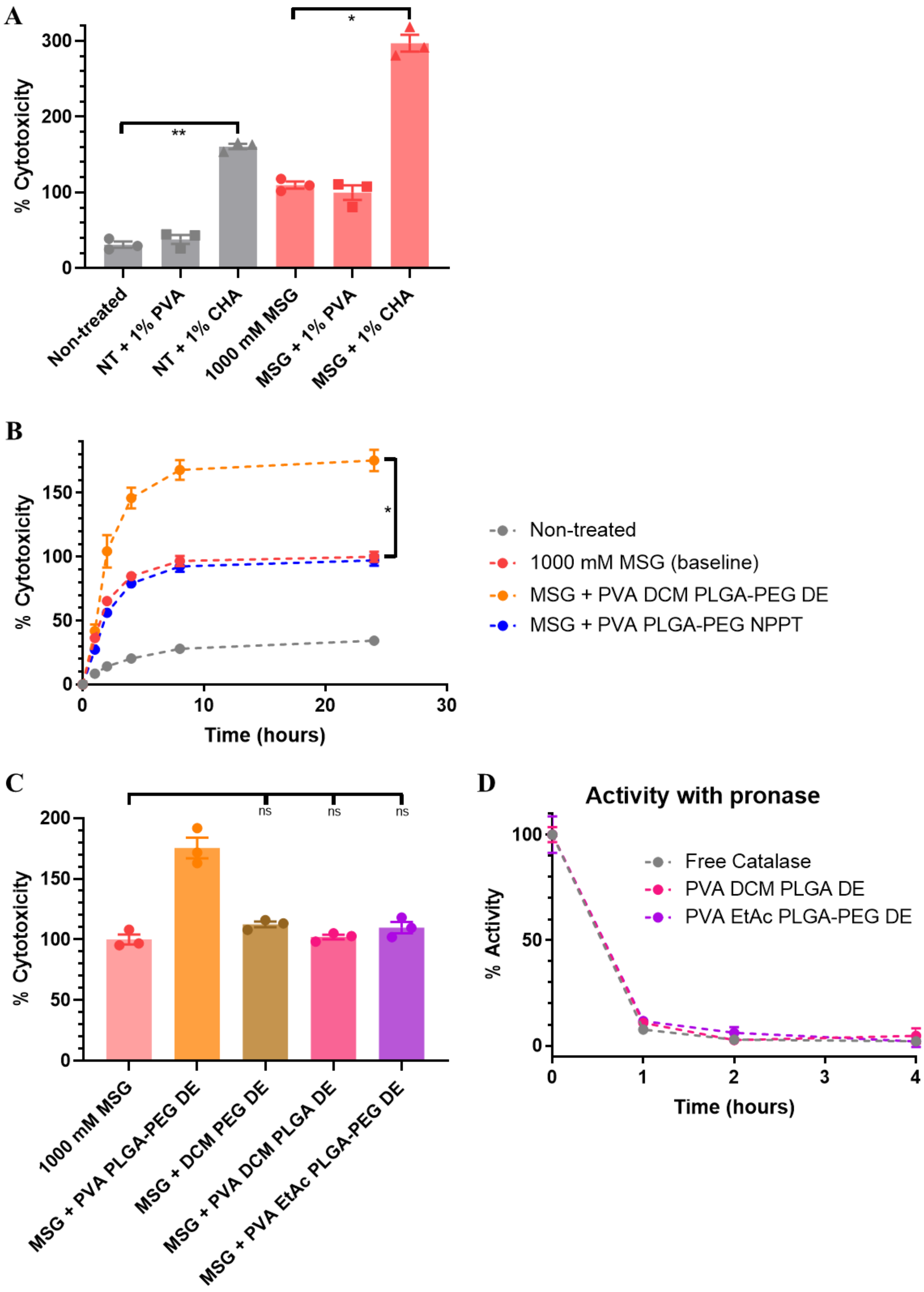A
% Cytotoxicity
300
200
100
0
**
*
Non-treated
NT + 1% PVA
NT + 1% CHA
1000 mM MSG
MSG + 1% PVA
MSG + 1% CHA
B
% Cytotoxicity
150
100
50
0
*
0
10
20
30
Time (hours)
Non-treated
1000 mM MSG (baseline)
MSG + PVA DCM PLGA-PEG DE
MSG + PVA PLGA-PEG NPPT
C
% Cytotoxicity
200
150
100
50
0
ns
ns
ns
1000 mM MSG
MSG + PVA PLGA-PEG DE
MSG + DCM PEG DE
MSG + PVA DCM PLGA DE
MSG + PVA EtAc PLGA-PEG DE
D
Activity with pronase
% Activity
100
50
0
0
1
2
3
4
Time (hours)
Free Catalase
PVA DCM PLGA DE
PVA EtAc PLGA-PEG DE

Figure 5.4: Determination of toxicity from DE nanoparticles. Percent cytotoxicity of A) NT and MSG-exposed slices to PVA and CHA surfactant, B) MSG-exposed slices to PVA DE- and NPPT-bNPs, and C) MSG-exposed slices to 5k mPEG solution that underwent 60s DE in DI/DCM, PVA bNPs with PLGA instead of PLGA-PEG, and PVA bNPs formulated with EtAc instead of DCM as organic solvent at 24h. D) To evaluate enzymatic protection, catalase activity was measured for catalase-loaded PLGA nanoparticles and PLGA-PEG with EtAc nanoparticles in the presence of 0.2 wt% pronase in PBS at 37°C (n=3). Data are reported as mean ± SEM.

5.2.3 The role of oxidative stress in DCM PLGA-PEG DE nanoparticle toxicity

Because the toxic DCM PLGA-PEG nanoparticles enhanced cytotoxicity on only MSG-exposed and OGD-exposed slices, but not NT or LPS-exposed slices, we investigated the mechanism of the excitotoxicity-induced vulnerability. It is well documented that both MSG and OGD induce excitotoxicity-representative disease environments in organotypic *ex vivo* brain tissue [156, 286]. Treatment of both MSG- and OGD-exposed slices with 0.1 mg superoxide dismutase (SOD) returned cytotoxicity levels to that of NT slices, confirming the role of superoxide-mediated oxidative stress in excitotoxicity (Figure 5.5A). SOD application in addition to MSG+bNP exposure slices reduced cytotoxicity from 156.2% to 25.6%, which was still significantly greater than NT slice cytotoxicity of 11.3% (*p*=0.001) (Figure 5.5B). Reduced glutathione (GSH) concentrations were significantly different for all three conditions, with $1.29\text{x}10^{-5}$, $3.47\text{x}10^{-5}$, and $3.84\text{x}10^{-5}$ µmoles of GSH per gram of brain tissue for NT, for MSG, and for MSG+bNP slices, respectively (Figure 5.5C). NT GSH levels were 3.7x greater than that of MSG (*p*=0.021), while MSG+NP GSH levels were 1.1x greater than that of MSG (*p*=0.030).

It is possible that with MSG exposure in combination with DCM PLGA-PEG bNP addition, the large dose of 0.1 mg SOD was inadequate for fully counteracting superoxide-induced damage. Generation of additional superoxide or other reactive oxygen species (ROS) would have elicited a further decrease in GSH levels as GSH is expended to scavenge ROS [287]. However, both MSG and MSG+bNP slices had similar GSH concentrations more than 3-fold less than the NT GSH level. Therefore, it is unlikely that the toxic nanoparticles increased the overall oxidative stress levels. The difference between NT versus MSG+bNP+SOD slice cytotoxicity (14.2%) was less than the difference between MSG versus MSG+bNP slice cytotoxicity (56.2%). We were unable to definitively identify whether the residual cytotoxicity difference between NT and MSG+bNP+SOD was due to MSG contributions, toxic nanoparticle contributions, or a combination of both. However, considering SOD fully inhibited MSG-induced cytotoxicity, we suspect that MSG-exposure with SOD treatment induced vulnerability to toxic bNP damage, but to a lesser extent than without SOD treatment. The DCM PLGA-PEG nanoparticles that were toxic on MSG- and OGD-exposed slices could be useful as protein delivery vehicles for inflammatory or regenerative environments without excessive ROS where they may not induce toxicity, or cancer applications where enhanced cancer cell death would be favorable.

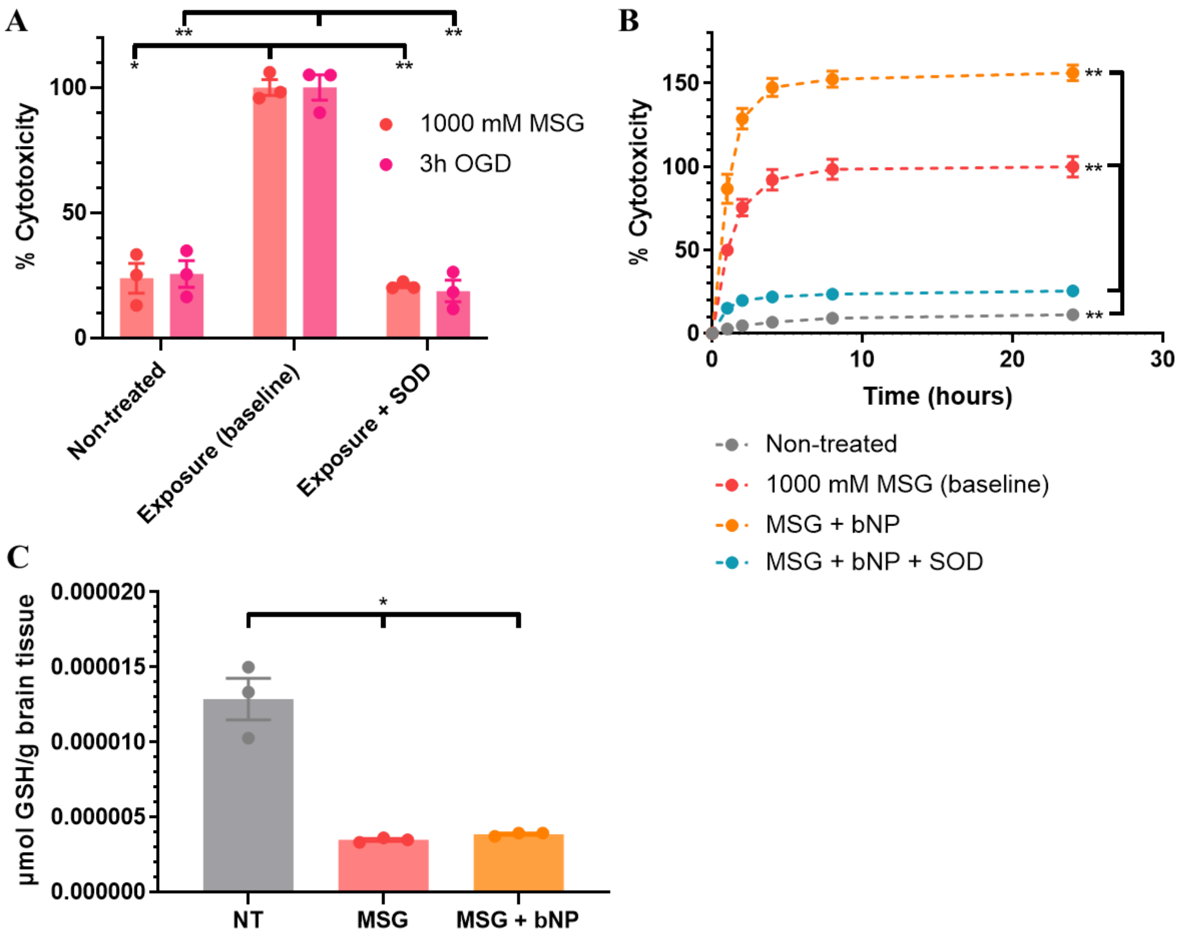

Figure 5.5: The role of oxidative stress in CHA PLGA-PEG DE nanoparticle toxicity. Percent cytotoxicity of A) NT, MSG- or OGD-exposed, and MSG- or OGD-exposed with 0.1 mg SOD slices at 24h (n=3), and B) NT, MSG-exposed, MSG-exposed with bNPs, and MSG-exposed with bNPs and 0.1 mg SOD slices (n=3-4). C) Glutathione levels of NT, MSG-exposed, and MSG-exposed with bNPs slices at 24h (n=3). bNP nanoparticles are formulated with CHA, DCM, and PLGA-PEG. Data are reported as mean ± SEM.

5.2.4 Exploration of PEG degradation and toxic product formation

Furthermore, we explored whether the PEG chain of the nanoparticle underwent any reactions from the sonication process that could account for ROS-dependent toxicity. Probe sonication inputs high energy into aqueous solution causing the formation and cavitation of gas bubbles that can produce high local temperature and pressure fluctuations that can split water molecules to form hydroxyl radicals [288, 289]. These hydroxyl radicals can then react with PEG, leading to degradation via C-O chain scission and the formation of acid, alcohol, or aldehyde functional groups [285, 290-292]. However, using H-NMR we did not detect any characteristic shifts indicative of the presence of carboxylic acid, alcohol, or aldehyde functional groups. The NMR spectra looked identical for nanoparticles formulated via toxic conditions of 15s, 30s, and 300s PLGA-PEG DE sonication in DCM, and via non-toxic conditions of NPPT and 30s DE sonication in EtAc (Figure 5.6A). In a model system of free PEG dissolved in DI/DCM, there was no decrease in melting temperature as a function of sonication time as determined by DSC (Figure 5.6B). Since PEG melting temperature decreases with molecular weight, this indicated no significant PEG degradation had occurred [293, 294]. Furthermore, there was no decrease in pH for DI/EtAc solutions with or without PEG (Figure 5.6C), suggesting that no appreciable concentrations of formic acid or acetic acid, or other carboxylic acid degradation products formed as would be expected upon PEG degradation [295]. Instead, pH decreased as a function of sonication time for only DI/DCM solutions, independent of the presence of PEG (Figure 5.6C), suggesting hydrochloric acid formation upon DCM degradation [296]. There are several potential explanations as to why we did not observe PEG degradation consistent with literature: (1) we studied free PEG alone instead of PEG as a copolymer with a hydrophobic segment such as in PLGA-PEG or Pluronic surfactants, (2) our sonication times of 30s are at least an order of magnitude shorter than the multiple minute- to hour-long sonication times explored in other studies, and (3) our sonication times are pulsed for 1s:1s on/off [285, 291, 292].

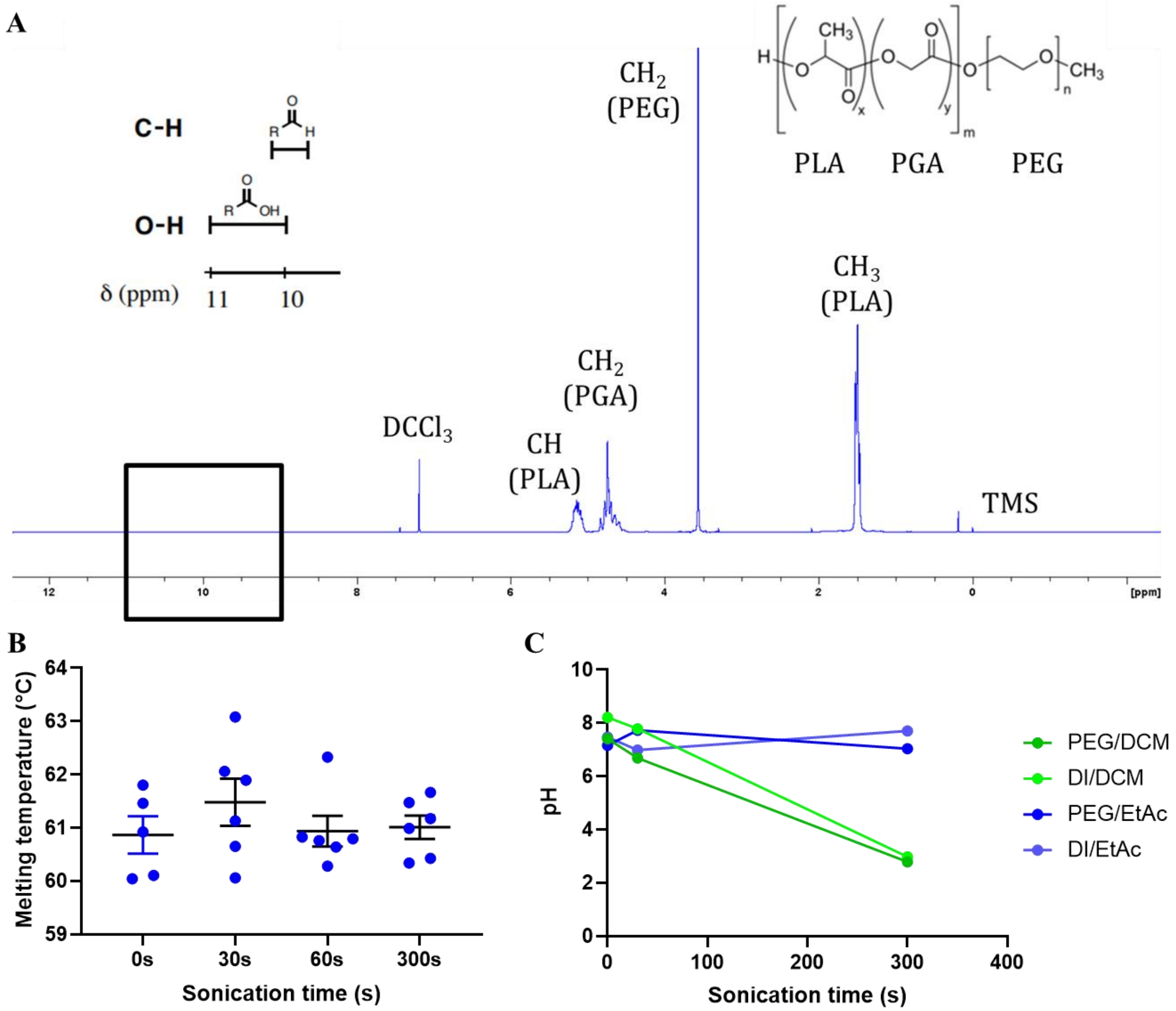

Figure 5.6: Characterization methods to detect potential PEG degradation and toxic product formation. A) Representative H-NMR spectrum of PLGA-PEG nanoparticles dissolved in deuterated chloroform, formulated via DE with sonication times of 15s, 30s, and 300s in DCM, and formulated via NPPT and 30s DE sonication in EtAc (n=1). All profiles exhibited no differences and lacked the detection of carboxylic acid or aldehyde functional groups. B) Melting temperature of free PEG as a function of DE sonication time as determined by DSC (n=5-6). Data are reported as mean ± SEM. C) pH as a function of DE sonication time for pure DI or PEG dissolved in DI/DCM or DI/EtAc and sonicated for 0s, 30s, or 300s (n=1).

The mechanism as to how the nanoparticles enact their cytotoxicity remains to be elucidated. To best gain insight into potential mechanisms of DCM-dependent toxicity, we compared the characteristics of DCM, EtAc, and TCM. Solvents with higher vapor pressure and lower surface tension undergo vapor bubble formation and subsequent cavitation at less extreme pressures [297, 298]. Because DCM has the highest vapor pressure of the three solvents as calculated from the

Antoine equation (DCM: 353 mmHg, TCM 158 mmHg, EtAc 74 mmHg at 20°C) [299], we speculate that under the nanoparticle formulation parameters used in our experiments, the sonication energy input was mild enough that cavitation only occurred with DCM as the organic solvent. Cavitation can induce the formation of reactive radical species for aqueous and organic solvents [300]. We propose that under DCM PLGA-PEG DE conditions, cavitation caused reactions with PLGA-PEG to yield currently unidentified toxic intermediates. Future work in organic solvent sonochemistry would be valuable to further investigate this theory. Nanoparticle toxicity is likely dependent on oxidative stress but may not exacerbate damage via increasing oxidative stress. There are a variety of potential mechanisms that remain to be explored, potentially involving excitotoxicity-induced altered behavior in the cellular uptake of nanoparticles, or nanoparticle upregulation of apoptotic or necrotic pathways. However, discerning the mechanism of toxicity may be challenging without identification of a toxic molecular signature of the DCM PLGA-PEG DE nanoparticles.

Additionally, for future work, it is important to evaluate the toxicity of DCM PLGA-PEG DE nanoparticles *in vivo* on healthy, neuroinflammatory, and excitotoxic brain tissue, as well as the liver, kidney, and other organs. However, both intravenous and intracranial administration routes may need to be explored to determine if biocompatibility is dependent on total accumulation at sites within the brain microenvironment that have susceptible brain cells. We speculate that potential toxic byproducts associated with the toxic DE nanoparticle might get cleared or neutralized in circulation when administered systemically prior to reaching the brain, whereas local intracranial administration may pose a potential risk to oxidatively stressed brain cells.

5.2.5 Alternative biocompatible nanoparticle formulations with enzymatic protection

We next investigated whether the addition of 5 mg free PEG during the sonication steps (PLGA-PEG+PEG) or replacement of DCM with TCM would yield biocompatible nanoparticles that protect enzymatic cargo. Both the PLGA-PEG+PEG and TCM formulations elicited no significant change in cytotoxicity (p=0.573 and p=0.103 respectively) (Figure 5.7A). While sonicated PLGA-PEG causes toxicity, free PEG holds characteristics that could improve formulation conditions and account for the elimination of nanoparticle-mediated toxicity. Due to PEG miscibility in both water and DCM, PEG readily diffuses to the aqueous/organic interfaces and also competitively occupies the interface to reduce protein denaturation [301]. It is possible that the presence of free PEG at the interface could substitute for the PLGA-PEG co-block and undergo the unknown toxicity-inducing reaction, followed by subsequent washout of free PEG-scapegoat, yielding biocompatible nanoparticles from the PLGA-PEG+PEG formulation condition. Both PLGA-PEG+PEG and TCM formulations also exhibited elevated catalase activity compared to free catalase at every measured timepoint across 24h in the presence of 0.2 wt% pronase, with a final percent initial activity of 30.6% ($p<0.001$) for PLGA-PEG+PEG and 32.1% ($p<0.001$) for TCM (Figure 5.7B). Similar formulation conditions to the enzyme-protecting DCM PLGA-PEG formulation, but with the addition of free PEG or replacement of DCM with TCM, could account for the retention of enzyme protective capabilities.

In attempt to further elucidate the role of additional free PEG incorporation in the formulation, we assessed nanoparticle cytotoxicity of bNPs with 5 mg free PEG added to the formulation after the sonication steps in the aqueous sink phase (PEG$_S$), bNPs with 5 mg free PEG added to the final 1 mL nanoparticle resuspension in PBS (PEG$_F$), and free PEG alone. PEG$_S$ and PEG$_F$ conditions exhibited intermediate toxicities of 121.8% and 124.0% respectively between 1000 mM MSG alone (100%) and MSG with toxic bNP addition (149.4%), while MSG with free PEG alone exhibited no significant difference in cytotoxicity from MSG exposure alone ($p=0.767$) (Figure 5.7C). However, at 24h timepoint only PEG$_F$ cytotoxicity was significantly different from MSG alone ($p=0.034$) while PEG$_S$ cytotoxicity differences trended towards significance ($p=0.075$). Interestingly, compared at the 4h earlier timepoint, PEG$_S$ and PEG$_F$ were both significantly greater than MSG alone ($p=0.037$ and $p=0.014$ respectively) (Figure 5.7C). PEG$_S$ and PEG$_F$ cytotoxicity were not significantly different from MSG with toxic bNP addition at 24h ($p=0.191$ and $p=0.217$ respectively) (Figure 5.7C), however the differences in percent cytotoxicity increase at 4h ($p=0.029$ and $p=0.032$ respectively) and 8h ($p=0.021$ and $p=0.020$ respectively) were significant (Figure 5.7D). Size, ζ-potential, and catalase activity characteristics of the PLGA-PEG+PEG with DCM and the PLGA-PEG with TCM formulations, and the size and ζ-potential characteristics of PEG$_S$ and PEG$_F$ bNPs are provided in Figure S5.3. It is possible that free PEG is still incorporated into the nanoparticle matrix for the PLGA-PEG+PEG, PEG$_S$, and PEG$_F$ formulations. If so, free PEG could reduce cytotoxicity by enhancing axonal repair, with studies demonstrating the neuroprotective ability of PEG in spinal cord injury and severe TBI *in vivo* via promoting cell membrane repair [302, 303]. Further exploration is needed to understand the exact mechanisms as to why PEG addition or TCM replacement results in nontoxic nanoparticle formulations.

Regardless these formulations provide promising alternatives for biocompatible, enzyme-protecting polymeric nanoparticles for the treatment of excitotoxicity in neurological diseases.

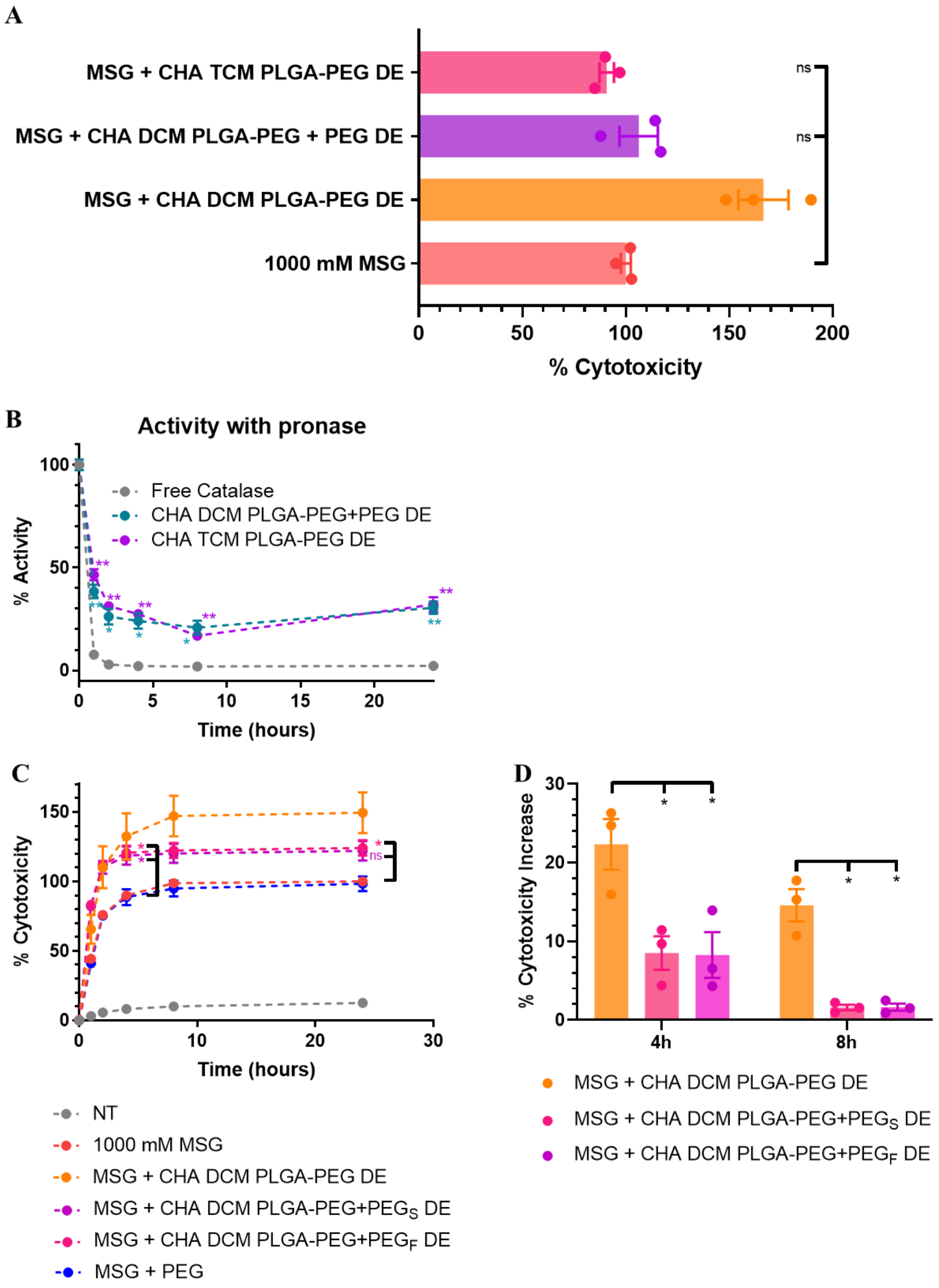

Figure 5.7: Identification of non-toxic DE nanoparticles with enzymatic protection. Percent cytotoxicity of A) MSG-exposed slices with the addition of PLGA-PEG nanoparticles with 5 mg PEG added during the sonication steps and PLGA-PEG nanoparticles formulated with TCM instead of DCM at 24h (n=3), and B)

the catalase activity of PLGA-PEG+PEG and PLGA-PEG with TCM nanoparticles in the presence of 0.2 wt% pronase in PBS over 24h at 37°C (n=6). Percent cytotoxicity of C) MSG-exposed slices with the addition of bNPs with 5 mg PEG added during the final resuspension (PEG_F), or sink phase (PEG_S), or 5 mg PEG alone (n=3), and D) the percent cytotoxicity increase of the toxic PLGA-PEG, PEG_F, and PEG_S bNP supernatants at 4h and 8h (n=3). Data are reported as mean ± SEM.

5.3 Conclusions

There is an urgent demand for therapeutics against neurological disease, and a high interest in the therapeutic potential of enzymes. The use of polymeric nanoparticle carriers is highly promising for enzyme delivery to the brain with their ability to bypass many obstacles to therapeutic delivery to the brain injury target site. We found an optimal sonication time of 30s for the DE formulation method to maximize enzymatic activity loading. As evidenced in the presence of pronase and in rat blood derived serum, catalase-loaded CHA DCM PLGA-PEG DE nanoparticles extended catalase activity across several hours while free catalase and catalase-loaded NPPT nanoparticles rapidly deactivated. However, independent of surfactant, DCM PLGA-PEG DE nanoparticles were also highly toxic on MSG- and OGD-exposed OWH brain slice models of excitotoxicity, but not on NT or LPS-exposed slices. A dense PEG coating for stealth-imbuing properties is requisite for an effective therapeutic but was also found to be a source of nanoparticle toxicity in DE formulations. We elucidated the role of oxidative stress in the vulnerability of excitotoxicity-induced OWH slices but found that the toxic DCM PLGA-PEG DE nanoparticles did not further increase oxidative stress, and that there was no indication of PEG degradation. Interestingly, incorporation of free PEG in addition to the PLGA-PEG in DCM during the DE sonication steps or replacement of DCM with TCM as the organic solvent yielded non-toxic nanoparticle formulations on MSG-exposed slices that still effectively extended catalase activity across 24h. Polymeric PLGA-PEG nanoparticles formulated via the DE method present an effective strategy for enzyme delivery against neurological diseases, but these formulations must be thoroughly screened to ensure protective capabilities and biocompatibility.

In the next chapter, we utilize the *ex vivo* model as a tool to study changes in the brain microenvironment due to oxygen-glucose deprivation (OGD) injury severity and therapeutic modulation. We use the OWH model to observe the effect of injury on microglial shape and nanoparticle uptake and demonstrate our ability to tailor microglial behavior for desired nanoparticle interactions for enhanced therapeutic strategies.

CHAPTER 6: Nanoparticle-microglial interaction in the ischemic brain is modulated by injury duration and treatment

6.1 Introduction

Cerebral ischemia is a major cause of death in both neonates and adults [304, 305]. Unfortunately, treatments for both neonatal hypoxia-ischemia (HI) and adult stroke provide only modest benefits in mortality and morbidity [306, 307]. Investigation of effective treatments for HI continues to be a critical area of research. Microglia, the resident immune cells of the brain, are of more recent and special interest for therapeutic targeting in HI [308]. Microglia become activated after ischemic injury, exhibit increased phagocytic behavior, and contribute to neuroinflammatory and reactive oxygen species (ROS) stress that may exacerbate damage in the brain [21]. Thus, an opportunity exists to provide neuroprotection after ischemic injury by designing therapeutics to target and modulate microglial behavior.

As discussed in Chapter 1.6 and 3.4, several distinct nanoparticle types have shown an ability to overcome biological barriers to drug delivery in the brain. Adequate intracellular trafficking of therapeutics also presents a major drug delivery challenge, but nanoparticles can leverage existing endocytosis pathways in microglial cells for internalization. Quantum dots (QDs) and poly(amidoamine) (PAMAM) dendrimer nanoparticles, among others, have shown accumulation within activated microglia [58, 59, 195, 309, 310]. While nanoparticles can facilitate and enhance drug transport in the brain, these effects are dependent on both nanoparticle characteristics and disease state [69], requiring further screening and study.

We investigate the role of injury, treatment, and nanoparticle type in driving nanoparticle-microglial interactions in ischemic conditions. As discussed in Chapter 1.7, OWH brain slice models of injury have emerged as a high-throughput platform for modeling disease processes and screening therapeutic platforms, including nanoparticles [59, 156]. Importantly, oxygen-glucose deprivation (OGD) has been widely used to model ischemic injury in organotypic slices [311]. OGD brain slice models mimic *in vivo* pathological processes including extracellular glutamate release, neuronal damage, and production of cytokines and oxidative stress markers [312-314].

Thus, OGD-exposed OWH slices are an optimal platform for studying nanoparticle-microglia interactions in ischemic injury.

In this chapter, to establish the degree of injury and microglial response following OGD exposure, we evaluate cytotoxicity and oxidative stress in healthy, OGD-exposed, and azithromycin (AZ)-treated OWH brain slices. AZ is an FDA-approved therapy that can suppress both acute and chronic pathologic microglial activation in response to ischemic stroke injury [315, 316]. Because microglial behavior correlates with disease severity [317, 318], AZ modulation of microglia provides one avenue to study microglia-nanoparticle interaction in response to treatment [319]. We use a Python-based image analysis technique to quantify the degree of microglial morphological heterogeneity following injury and treatment. We next investigate how injury alters the ability of nanoparticles to diffuse within the brain, an important factor for maximal distribution to target microglial cells. Lastly, we use flow cytometry and immunofluorescent imaging to quantify nanoparticle uptake in microglia based on injury and treatment. We compare 3 distinct nanoparticle platforms, polystyrene (PS)-PEG, PAMAM dendrimers, and cadmium selenide/ cadmium sulfide (CdSe/CdS) core/shell QDs, to determine the influence of nanoparticle physical characteristics on microglial uptake. In using OWH slices to probe nanoparticle-microglial interaction after disease and treatment, our study informs the design of nanoparticles to leverage the brain microenvironment and target microglial cells for enhanced therapeutic outcome in ischemic conditions.

6.2 Results

6.2.1 OGD time-dependent severity

HI duration can drastically change disease outcomes [320]. Therefore, we first investigated the impact of OGD time on cell viability and the oxidative stress environment. Compared to NC slice cytotoxicity of 11.2%, 0.5h, 1.5h, and 3h OGD exposure times resulted in significant increases in cytotoxicity of 54.3%, 33.8%, and 32.9% respectively, as determined by PI staining (Figure 6.1A). The 0.5h OGD cytotoxicity was also significantly higher than that of 1.5h or 3h OGD. 0.5h, 1.5h, and 3h OGD exposure times also yielded significantly decreased GSH concentrations of 1.7-fold, 4.1-fold, and 2.3-fold reductions respectively (Figure 6.1B). I performed OWH slicing and culturing, and Joseph and I exposed OWH slices to OGD for this chapter. Zhang and Filteau obtained the images, while Filteau and I performed the analysis for PI+/DAPI+ percent cytotoxicity. I obtained and analyzed the data for GSH concentration.

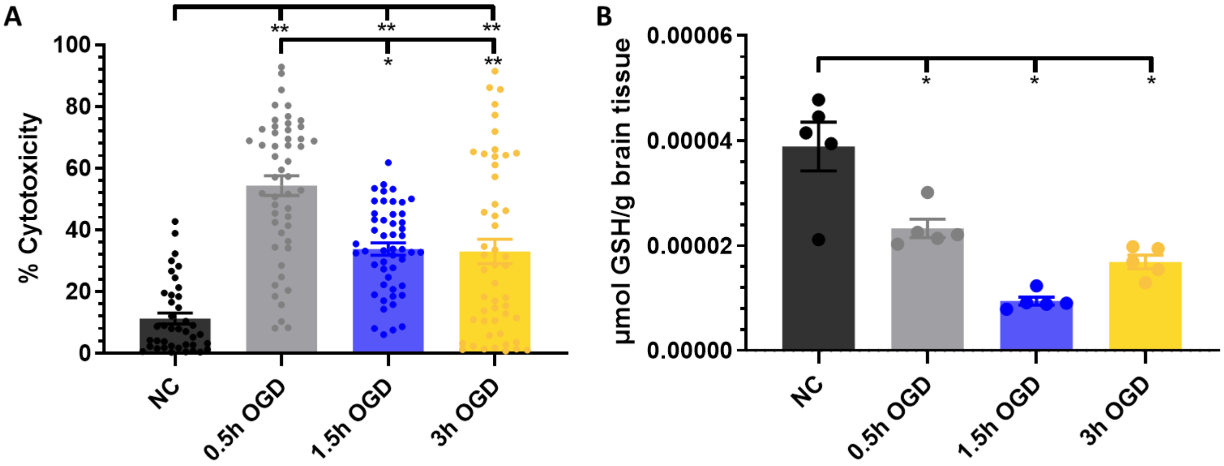

Figure 6.1: OGD exposure-dependent effect on cell death and oxidative stress environment. A) Percent cytotoxicity as determined by PI+/DAPI+ cell ratio (n=40-50 per condition) and B) GSH concentration (n=5) for NC, 0.5h, 1.5h, and 3h OGD exposed brain slices.

6.2.2 Therapeutic effect of SOD and AZ on OGD-induced injury

Prior to the investigation of AZ effects on nanoparticle interaction with microglia, we evaluated the effect of AZ and SOD on OGD-induced cytotoxicity to confirm therapeutic effects seen in literature. We have previously shown SOD can attenuate excitotoxic damage in OWH brain slices [156]. SOD addition to 3h OGD-exposed slices significantly reduced cytotoxicity of 17.1% (*p*=0.036) (Figure 6.2A). Having observed the greatest cytotoxicity induced by 0.5h OGD compared to NC, we proceeded to investigate the cytotoxicity effect of AZ on 0.5h OGD-exposed slices. AZ treatment significantly reduced cytotoxicity to 14.0% (*p*<0.001) (Figure 6.2B). AZ treatment also significantly increased GSH concentration 1.5-fold compared to that of 0.5h OGD (*p*=0.013) (Figure 6.2C).

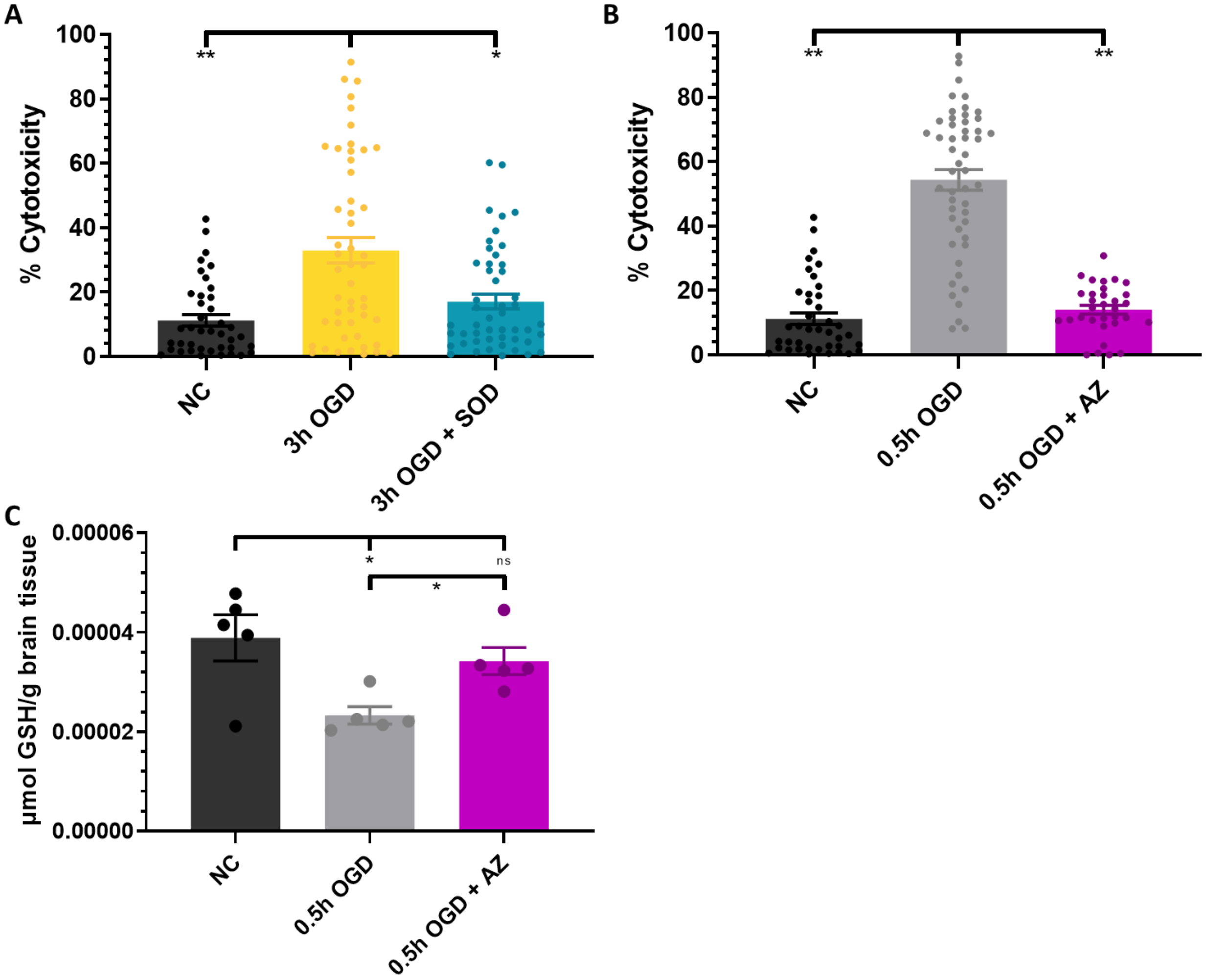

Figure 6.2: Therapeutic effects on OGD exposure-induced injury. Percent cytotoxicity of A) NC, 3h OGD, and 3h OGD with SOD addition (n=40-50 per condition) and B) NC, 0.5h OGD, and 0.5h OGD with AZ addition (n=33-50 per condition) measured by PI+/DAPI+ cell ratio. C) GSH concentrations of NC, 0.5h OGD, and 0.5h OGD with AZ addition (n=5). NC, 0.5h OGD, and 3h OGD conditions are the same as presented in Figure 6.1.

6.2.3 OGD and AZ effects on microglial shape as determined by VAMPIRE

To better understand microglial response to OGD injury, we characterized microglial morphological heterogeneity across disease states. Microglial morphology and heterogeneity are dependent on the disease environment and are one indicator of microglial phenotype and function [321, 322]. Relevant to this study, nanoparticle uptake has been correlated to microglial activation state [58, 323], with similar findings in liver-derived macrophages, where phenotype determined nanoparticle uptake [324]. Confocal images of microglia from each group were used to train a model via VAMPIRE [49], which resulting in 5 distinct microglial shape modes and subsequent classification of each microglial cell into its closest matching shape mode. The frequency of the 5 shape modes for each group is the percentage of microglia that exhibited the given shape mode (Figure 3A). 0.5h OGD with AZ treatment resulted in a distribution of shape modes similar to that of NC microglia: shape modes 3, 4, 5, 1, and 2 in order of increasing frequency. Overall, 0.5h OGD showed a reduced spread in shape mode frequencies, indicating an increase in microglial shape heterogeneity since all 5 shape modes were more equally represented. The absolute difference of shape mode frequency from NC shape mode frequency was 4.5% and 2.2% for 0.5h and 0.5h OGD+AZ respectively, although the difference between the two groups was not significant (p=0.083) (Figure 3B). Circularity was calculated directly from individual microglia. Upon 0.5h OGD exposure, microglia exhibited a significantly increased circularity of 0.69 compared to NC circularity of 0.50 (p<0.001) (Figure 3C). AZ treatment reversed the extent of microglial circularity to 0.53, significantly lower than that of 0.5h OGD (p<0.001). NC and OGD+AZ circularity were also significantly different (p<0.001). Furthermore, circularity did not correlate to shape mode, with a greater circularity for the 0.5h OGD condition for each of the 5 shape modes (Table S6.1). Zhang obtained the microglia images for VAMPIRE and microglial morphology analyses. Using the microglia images, Helmbrecht executed the VAMPIRE package and analyzed the microglial morphology shape frequency data. Helmbrecht and I analyzed the absolute difference in shape mode frequencies and microglia circularity data.

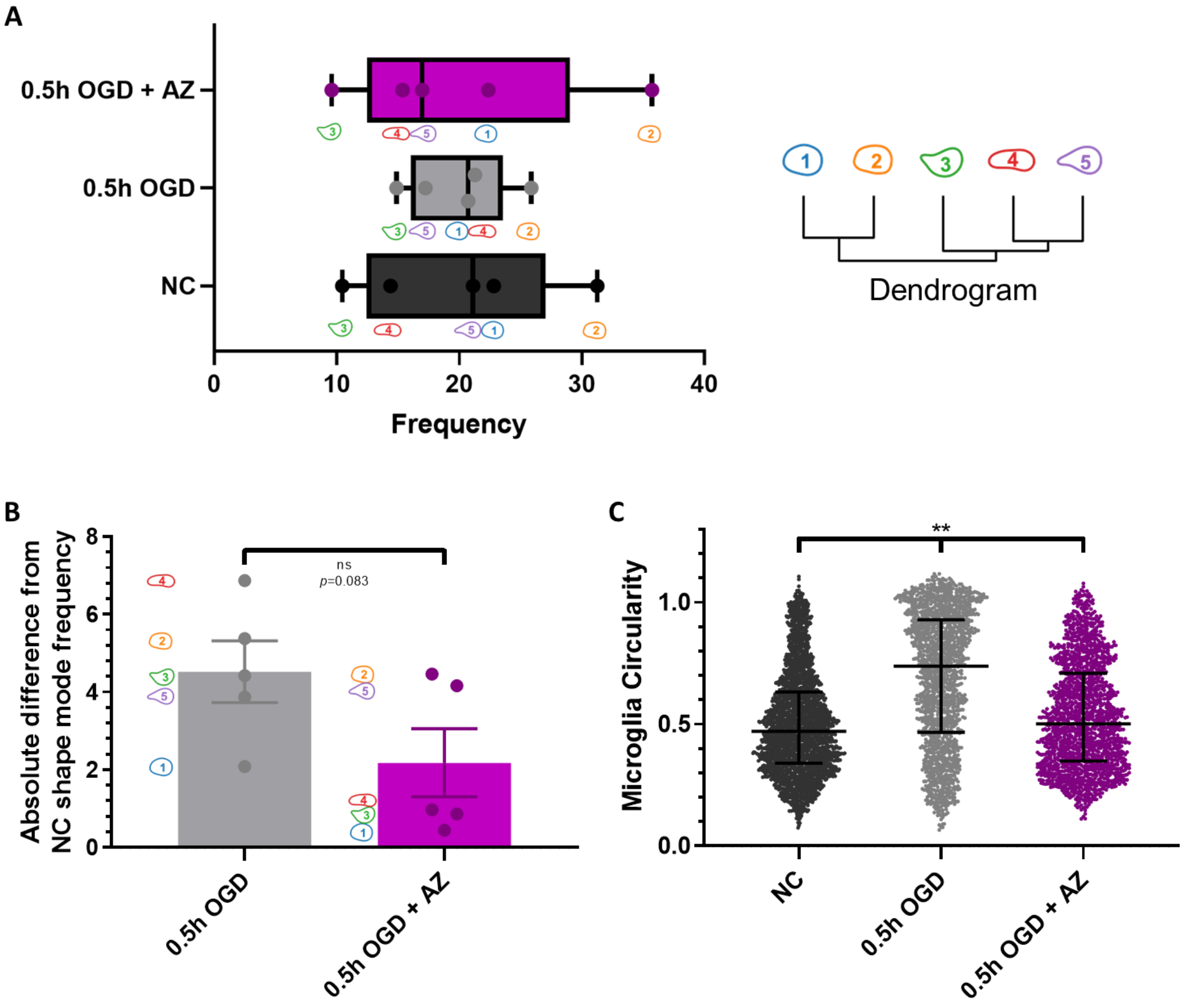

Figure 6.3: AZ reverses microglial heterogeneity and circularity after 0.5h OGD. A) Frequency of 5 shape modes of microglia for NC, 0.5h OGD, and 0.5h OGD+AZ groups as generated from the VAMPIRE package. B) Absolute difference in shape mode frequencies of 0.5h OGD and 0.5h OGD+AZ from NC shape mode frequencies. C) Microglial circularity of NC (n=2954 microglia from 4 slices), 0.5h OGD (n=1539 microglia from 5 slices), and 0.5h OGD+AZ (n=1612 microglia from 3 slices).

6.2.4 OGD enhances nanoparticle diffusion through the brain ECS

Nanotherapeutics must be able to reach target cells from the point of entry in the brain. To probe the effect of OGD-exposure on a nanoparticle's ability to move, we performed MPT with 40nm PS-PEG nanoparticles in *ex vivo* slices after OGD. Particle characteristics are in Table S6.2. Mean squared displacements (MSD) were calculated for each trajectory, and the geometrically ensemble-averaged MSD (<MSD>) for each experimental group was generated as a function of lag time (Figure 6.4A). Regardless of OGD duration, nanoparticles showed greater displacement, indicating an elevated ability to diffuse, compared to the NC group. Extraction of D_{eff} values using the Einstein-Smoluchowski Equation revealed a 16.7-, 16.5-, and 16.6-fold increase in nanoparticle diffusive ability in the 0.5h, 1.5h, and 3h OGD groups, respectively, compared to that of the NC group (Figure 6.4B). The <MSD> curves were then fit using the anomalous diffusion equation to obtain values of the anomalous diffusion exponent, α. Trajectories were classified as either superdiffusive ($\alpha > 1.25$), normal ($0.75 \leq \alpha \leq 1.25$), or subdiffusive ($\alpha < 0.75$) (Figure 6.4C). OGD increased superdiffusive and decreased subdiffusive transport for all exposure times. The proportion of superdiffusive trajectories increased by 6.1% while subdiffusion decreased by 10.8% between the NC and 3h OGD groups. Changes in diffusion were region-dependent (Figure 6.4D); the 0.5h, 1.5h, and 3h OGD exposure increased diffusion by 5.8-, 4.3-, and 4.5-fold, respectively, in the cortex compared to 27.8-, 38.0-, and 45.8-fold, respectively, in the striatum (Figure 6.4E). The regional and combined median D_{eff} and trajectory counts are presented in Table 6.1.

We also anticipated that OGD exposure would alter the ECS through which nanoparticles can move. To estimate the distribution of effective ECS pores, we fit the Amsden obstruction scaling model for entangled and cross-linked hydrogels [325] to the D_{eff} data in Figure 6.4B. As exposure to OGD increased, the distribution of pore sizes shifted to larger pores (Figure 6.4F). The percentage of pores larger than 40nm increased from 2.5% in the NC to 10.0%, 13.7%, and 24.5% in the 0.5h, 1.5h, and 3h OGD groups, respectively. Two final geometric features were calculated to better characterize nanoparticle behavior in the diseased brain microenvironment: trajectory boundedness (Figure S6.1A) and efficiency (Figure 6.1B). Boundedness reflects the proportion of a trajectory which is restricted within a circular area, while efficiency reflects the ability of a nanoparticle to maximize displacement while minimizing distance traveled. 0.5h OGD caused a 1.1-fold decrease in boundedness and 6.1-fold increase in efficiency compared to that of NC. 1.5h OGD and 3h OGD also increased efficiency (by 6.4- and 5.4-fold, respectively) but elicited no fold-change on boundedness compared to that of NC. McKenna obtained and analyzed the data for MPT studies.

Table 6.1. D_{eff} in rat brain tissue were extracted at $\tau = 0.303$ s from nanoparticle trajectories in the cortex (n=5 videos per slice) and striatum (n=5 videos per slice) in n=3 slices per group.

Treatment	**Trajectories in Cortex**	**D_{eff} in Cortex ($\mu m^2/s$)**	**Trajectories in Striatum**	**D_{eff} in Striatum ($\mu m^2/s$)**	**Median D_{eff} ($\mu m^2/s$)**

NC	24,382	0.0338	64,840	0.00707	0.0118
0.5h OGD	65,305	0.197	42,378	0.196	0.197
1.5h OGD	43,520	0.146	38,787	0.269	0.195
3h OGD	103,415	0.151	51,285	0.324	0.195

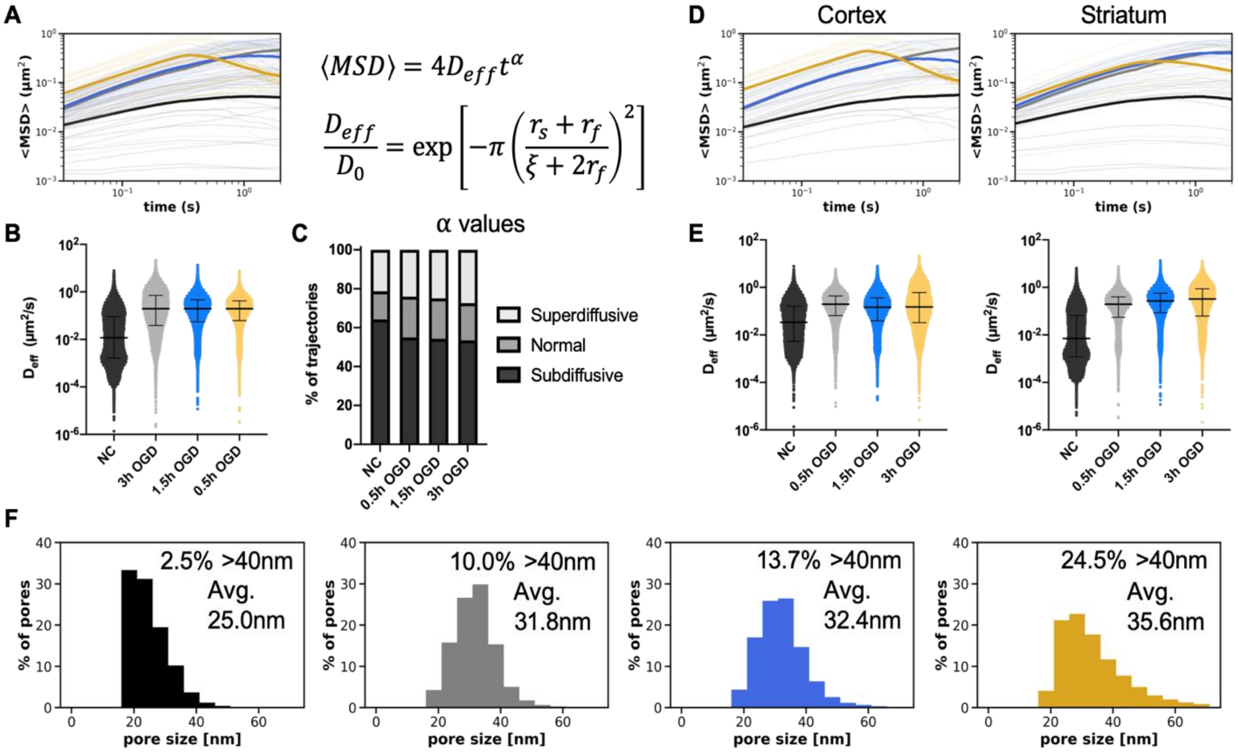

Figure 6.4: Characterization of nanoparticle diffusive behavior after OGD. A) Geometrically ensemble-averaged MSD vs lag time for NC (black), 0.5h (grey), 1.5h (blue), and 3h OGD (gold) conditions. Faint lines represent averages of each video (30 total per group) and the bolded line represents the mean of all videos. B) Deff values extracted from each trajectory from all videos (n=10) in all slices (n=3) per group (1 dot = 1 trajectory). C) The anomalous exponent α was calculated by fitting trajectory MSDs to the anomalous diffusion equation. α was used to classify trajectories as either superdiffusive, normal, or subdiffusive. D) <MSD> vs lag time split by brain region (left: cortex, right: striatum). E) Deff values split by brain region: (left = cortex, right = striatum). F) Effective ECS pore size distributions in NC and 0.5h, 1.5h, and 3h OGD slices from left to right. % of pores >40nm and average pore size are indicated by text. Data for B & E are reported as median ± interquartile range.

6.2.5 Microglial uptake of nanoparticles is influenced by disease state and nanoparticle properties

We have confirmed OGD slice health can be recovered following AZ treatment and that particles can readily move within the OGD brain environment. We next sought to understand how injury and treatment influence the interaction of PS-PEG, D-Cy5, and QD nanoparticles with microglial cells. Using flow cytometry, we determined the proportion of microglia which were nanoparticle-positive in each treatment condition. We showed a significant increase in microglial uptake of PS-PEG after OGD (PS-PEG: 0.47% NC vs 0.5h OGD 1.50%, p=0.016), and that AZ treatment reverted microglia to low-uptake behavior (PS-PEG: 0.59%) (Figure 6.5A). Application of 100x higher concentration PS-PEG showed similar trends, with 27.3%, 67.5%, and 40.4% uptake in microglial cells for NC, 0.5h OGD, and 0.5h OGD+AZ conditions (Figure S6.2). Microglial uptake of D-Cy5 (Figure 6.5B) and QDs (Figure 6.5C) however, did not exhibit significant differences across all three conditions. QDs were internalized at much higher proportions than the other nanoparticle types across all experimental groups: median values for the 0.5h OGD group were 1.42%, 0.68%, and 25.0% for PS-PEG, D-Cy5, and QDs, respectively. Confocal images confirm that microglial uptake of nanoparticles occurred for all nanoparticle types and experimental conditions.

One important result from flow cytometry was the change in microglial number after injury and treatment. While microglia made up 20.33% of live cells in a NC slice, their proportion was significantly reduced after 0.5h OGD (3.99%), measured 5 hours after the end of injury (p=0.016). However, treatment with AZ increased microglial proportion to 14.70% (p=0.016 versus 0.5h OGD) (Figure 6.6A). After 0.5h OGD, we saw a lower microglial percentage out of all live cells sustained for 25h (NC: 15.49%, 0.5h OGD: 4.00%, p=0.024) as determined by flow cytometry (Figure S6.3). This was further supported by quantitation of microglial area to total cell number at 24h after injury (Figure 6.6B). Interestingly, we observed a regional difference in microglial vulnerability. In the cortex, area covered by microglia did not change significantly across experimental condition (Figure 6.6C), but microglial area in the thalamus was significantly reduced after OGD (p<0.001). Treatment with AZ increased microglial coverage (p=0.031 compared to OGD), although still to a reduced level from NC (p<0.001) (Figure 6.6D). Representative confocal images from each region are shown in Figure 6.6E. Joseph and Zhang obtained and analyzed the nanoparticle-microglia co-localization images. Joseph obtained and analyzed the flow cytometry data. Joseph obtained and analyzed the flow cytometry data. Zhang obtained the microglia density images. Filteau analyzed the microglia density data.

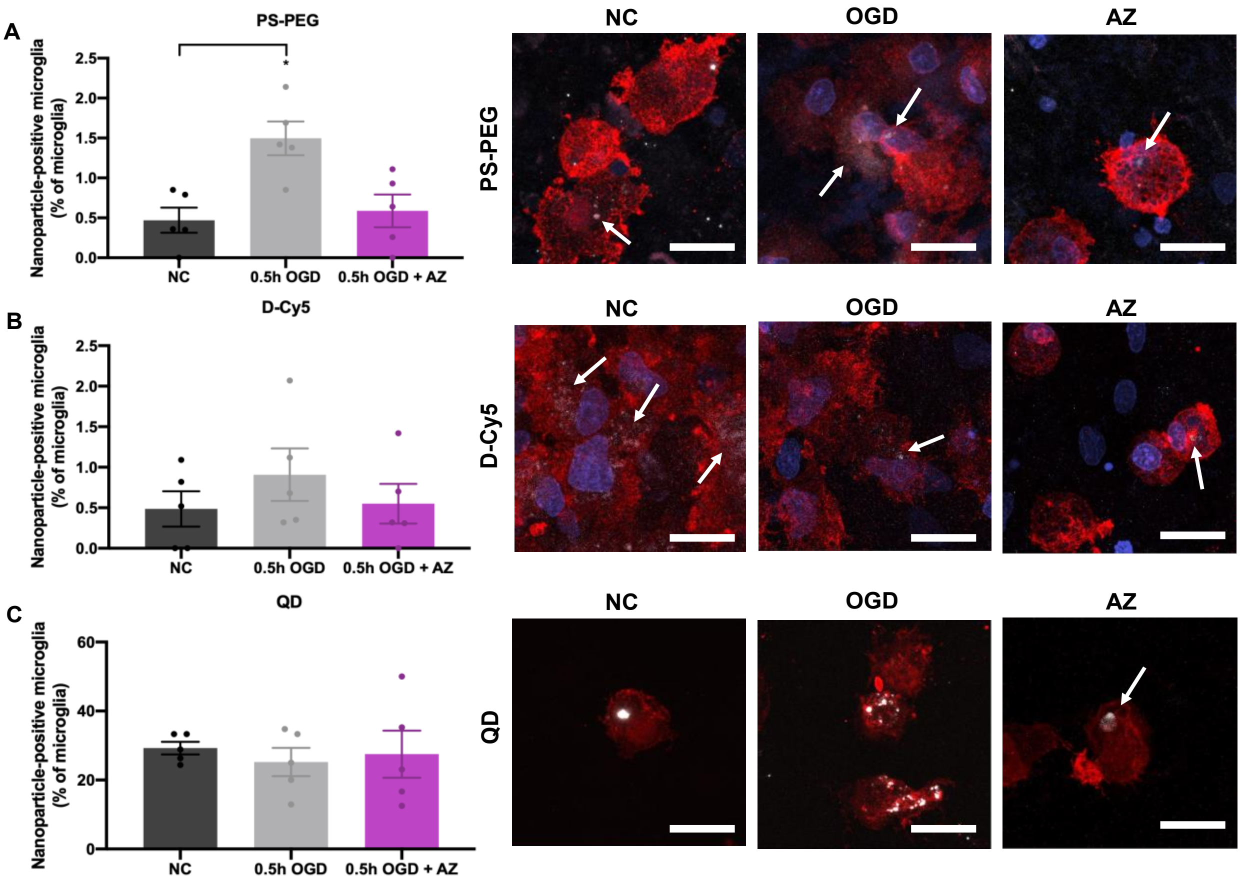

Figure 6.5: Microglial uptake of PS-PEG, D-Cy5, and QD nanoparticles at 5h for NC, 0.5h OGD, and 0.5h OGD+AZ treatment. Flow cytometry results of A) PS-PEG-positive, B) D-Cy5-positive, and C) QD-positive microglia as a proportion of all microglia in NC, 0.5h OGD, and 0.5h OGD+AZ groups. Co-localization of A) PS-PEG nanoparticles (white), B) D-Cy5 nanoparticles (white), and C) QD nanoparticles (white) with NC, 0.5h OGD, and 0.5h OGD+AZ microglia (red) and cell nuclei (blue). All scale bars represent 20 µm.

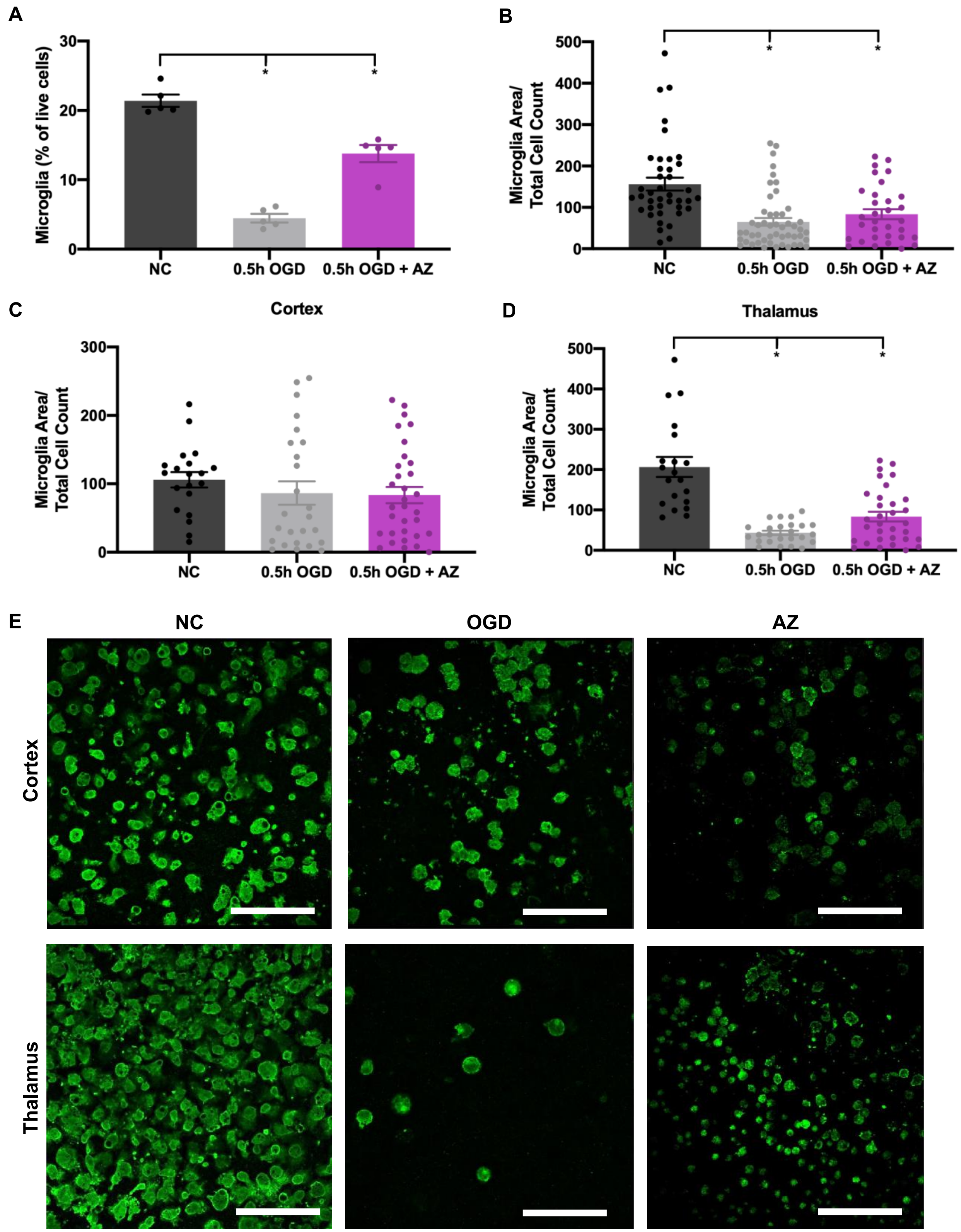

Figure 6.6: Microglial number decreases after OGD and is restored with AZ. A) Flow cytometry results of microglia as a proportion of all live cells in the NC, 0.5h OGD, and 0.5h OGD+AZ groups 5h after injury.

Microglial area of NC, 0.5h OGD, and 0.5h OGD+AZ slices normalized to DAPI-positive cell count from images at 24h after injury B) for all images, C) cortex alone, and D) thalamus alone. E) Representative images of microglia (green) in the cortex and thalamus of NC, 0.5h OGD, and 0.5h OGD+AZ slices. All scale bars represent 100µm.

6.3 Discussion

We investigated the nanoparticle- and disease-dependent nature of nanoparticle-microglia interactions using an OWH slice model of ischemic brain injury. Our first goal was to modulate ischemic brain injury severity by increasing OGD exposure times. There was an increase in cytotoxicity for all OGD exposure times compared to that of NC. Surprisingly, 1.5h and 3h OGD exposure times resulted in lower cytotoxicity than 0.5h OGD exposure. Previous studies have demonstrated an increase in cytotoxicity from 0.5h to 1h of OGD *ex vivo*, and 60 min is regarded as the timeframe of OGD-induced neuronal swelling followed by apoptotic and necrotic death [326-329]. In our study, exposure to 0.5h OGD was sufficient to induce significantly different outcomes than the NC condition, in agreement with other findings [312, 330, 331]. Considering OGD mediates damage via oxidative stress, we measured the concentration of the redox buffering molecule GSH as another measure of slice health [332]. All OGD exposure times reduced GSH concentrations, representing an oxidatively stressed environment [333].

Microglia are potent cellular targets for drug delivery, due to their role propagating pathological processes after ischemic injury. Previous studies have demonstrated microglia-specific drug delivery with PAMAM dendrimers, which was attributed to the increased phagocytic behavior of microglia in an activated state [310, 334, 335]. Increased microglial uptake of dendrimers is also present after HI in mice *in vivo*, retinal HI injury in mice *in vivo*, and maternal inflammation-induced cerebral palsy rabbits *in vivo* and *ex vivo* [58, 336-338]. In all three models, microglia exhibited robust activation and proliferation, which was associated with an amoeboid cell shape, pro-inflammatory phenotype, and increased phagocytic behavior. However, in our study, dendrimer uptake was not significantly changed, and no microglial proliferation occurred compared to that of the NC condition. In fact, microglial area from confocal images and microglial counts from FACS indicate a decrease in microglial number after OGD. One important note is the presence of a global inflammatory response *in vivo* that is absent from our slice preparation process *ex vivo*. Without systemic inflammatory contributions such as invasion by pro-inflammatory systemic immune cells, OGD alone may be insufficient to mediate microglial proliferation [339-

342]. Thus, one major limitation of inducing injury *ex vivo* is the inability to fully represent complex pathological processes such as neuroinflammation that involves the immune system. Future studies may overcome this limitation by incorporating a strong inflammatory stimulus *in vivo* before brain extraction.

Microglial phenotypes in slice culture are also different than those represented *in vivo* [343] and several studies have shown that nanoparticle uptake is correlated to microglial phenotype [323, 344]. Accumulating evidence shows the importance of shape in characterizing microglial phenotype [345, 346], supporting microglial characterization using shape modes independently or in tandem with other classification systems, such as surface marker presentation, transcriptomics, or cytokine expression. Improving microglial characterization is essential to understanding microglial-nanoparticle interactions, especially as the classical M1 and M2 microglial polarization phenotype schema progressively phases out [347]. To better characterize the range of microglial morphologies in our OGD slice model, we used computer-aided morphological analysis through application of the VAMPIRE software package. 0.5h OGD induced changes in microglial shape modes, which were reversed back to NC shape mode distributions upon AZ treatment. AZ has previously been shown to promote an anti-inflammatory phenotypical change of macrophages and microglia [315]. Although there remained some variation in frequency for the 5 shape modes for 0.5h OGD+AZ compared to that of NC, the ranking of shape mode frequencies from least (3) to greatest (2) followed the same ranking as the NC microglia shape mode frequencies. The VAMPIRE package enables in-depth morphological analysis and detection of nuances in microglial shapes that encompass the heterogeneity of microglia that the human eye cannot detect. However, extracting intuitive shape characteristics of microglia from VAMPIRE is non-trivial given the complexity in interpreting the large dataset "machine-vision" classifications of the VAMPIRE package [49]. Independent of shape mode, one readily interpretable morphological distinction between groups was that of microglial circularity, where high circularity corresponds to a non-branching amoeboid morphology characteristic of a pro-inflammatory activated state [346]. Although a value of 1 describes a perfect circle, some circularity values (1.2% of NC, 14.3% of 0.5h OGD, and 1.6% of 0.5h OGD+AZ) are slightly above 1 (1.12 max) due to errors in computer estimation of pixel perimeters [348]. We found that 0.5h OGD increased microglial circularity and AZ prevented amoeboid morphology, reducing circularity levels to closer to that of NC microglia. Further work may better determine the association between nanoparticle uptake and microglial phenotype by analyzing additional cell features, such as degree of branching, branching polarization, and soma size, in combination with transcriptomic analysis, especially for nanoparticle-containing cells.

In contrast to dendrimers, PS-PEG nanoparticles exhibited increased microglial accumulation after OGD, and QDs were internalized at roughly equal proportions regardless of disease state. QDs were able to achieve orders of magnitude higher microglial accumulation after administration at the same dose as PS-PEG and D-Cy5. Our results indicate that microglial phagocytosis is highly dependent on nanoparticle platform, and disease-induced changes in microglial behavior are not leveraged equally among all nanoparticle types. These platforms differ in size, rigidity, and chemical composition which can influence nanoparticle-cell interactions [34, 349] suggesting that nanoparticle physicochemical parameters must be well-tuned to achieve accumulation in target cells at sites of injury. For example, rigid lipid nanoparticles could more easily pass through cell membranes compared to less rigid nanoparticles [350]. Previous work also supports microglial uptake of high-rigidity nanoparticles, namely gold nanoparticles *in vitro* and silica and QD nanoparticles *ex vivo* and *in vivo* [59, 351, 352].

Nanoparticle diffusive ability also plays a role in reaching target microglial cells and in achieving maximal therapeutic impact [353, 354]. As evidenced by the MPT results after OGD, PS-PEG nanoparticles exhibited more than 16-fold higher diffusive ability compared to the NC condition. In this study, we directly confirmed diffusivity of PS-PEG, but PEGylated QDs and PAMAM dendrimers have also been shown to move effectively within the brain parenchyma [195, 310, 355]. After OGD, PS-PEG nanoparticle trajectories were more efficient and the population of particles behaving subdiffusively decreased. This shift in diffusive transport modes may be associated with other disease-mediated changes. For example, OGD-induced cytotoxicity might reduce cell density and therefore decrease the likelihood of subdiffusive transport, which is characteristic of nanoparticles closely interacting with cellular compartments. Macroscopic ECS changes after *ex vivo* ischemic injury have also been previously reported, including an increase in striatal tortuosity and decrease in ECS volume fraction of brain tissue in the hippocampus and cortex [356, 357]. The formation of dead-space domains may explain both an increase in estimated ECM pore size and tortuosity [358]. OGD also potentially increases the expression of ECM-degrading matrix metalloproteinases (MMPs), as demonstrated in models of cerebral ischemia [359]. The increase in ECM-degrading enzymes can alter pore sizes and subsequently effect nanoparticle diffusion in the ECS. In this study, the distribution of ECS pore sizes did in fact shift to larger pores following OGD, which could be leveraged by the PEGylated nanoparticles for effective diffusive transport through injured tissue.

The proportion of pores greater than 40nm increased with increasing exposure of OGD. Interestingly, an appreciable percentage of pores were predicted to be smaller than 40nm, the particle diameter. Neutrally charged 40nm PS-PEG nanoparticles can evade many of the mechanisms by which extracellular movement is hindered [355], making diffusion predominantly influenced by steric interactions. While it is likely that some populations of particles are truly immobilized within pores, the Amsden obstruction model may be underestimating pore size by assuming nanoparticles are completely inert. PEGylated nanoparticles may interact with microglia, other cell types, and various components of the ECM, which hinders transport and may skew pore size estimates. Although the average pore size was smaller than previously calculated, the range of pore sizes identified in this study is similar to previous findings using MPT analysis in brain slices [130]. The use of 40nm particles for prediction, compared to 40nm, 100nm, and 200nm particles used by Nance *et al*. [355], could underestimate the true size of pores >40nm and skewing the calculated average pore size to be smaller. Regardless, the model was applied equally across all experimental groups and therefore still provides insight into the differences existing between conditions in this study. Nanoparticle probe size, different culturing conditions, and DIV can each alter MPT analysis and the application of the Amsden obstruction model, requiring further investigation in the OGD model.

One benefit of the OWH slice platform for furthering this work is the ability to study regional variability in response to injury. After both 1.5h and 3h OGD, nanoparticles in the striatum had consistently faster D_{eff} compared to those in the cortex. Microglial area coverage also indicated a greater injury response in the midbrain. Only the thalamus, not the cortex, showed a decrease in microglial area coverage after 0.5h OGD. Although we did not probe for a mechanism to explain regional differences, such investigation can have important implications for therapeutic development. One recent study investigated the injury-resistant nature of the hypothalamus region and identified that slow neuronal depolarization in the region may be one native mechanism of neuroprotection [360]. Enhanced therapeutic penetration within diseased brain regions could reduce requisite dose amount and frequency and avoid inadvertent cytotoxicity on healthy tissue. Due to the intricate balance of pro- and anti-inflammatory activity in the brain microenvironment after disease, region specific control can also reduce over-scavenging of reactive oxygen species or excessive inhibition of inflammatory processes that could interrupt healthy cellular function or exacerbate damage [98, 361, 362]. Given that ischemic injury manifests in regional patterns in multiple phases [224, 363], the continued investigation of regional variations in the brain could inform therapeutic strategies that are highly advantageous in combating immediate and ongoing regionally-dependent disease sequelae.

Further cross-platform investigation will be important to elucidate advantageous nanoparticle characteristics, in addition to diffusive ability, size, rigidity, and surface functionalization, for microglial-targeted drug delivery after injury. Microglial uptake of additional nanoparticle platforms, such as nanocrystals or polymeric micelles, has been understudied yet may elucidate new therapeutic avenues. Importantly, immediate AZ treatment of OGD-injured slices returned microglial uptake behavior of all nanoparticle types closer to that of NC conditions, suggesting that modulated microglia of recovered brain tissue behave similarly to healthy microglia. While this work primarily studied AZ modulation of slice health and microglial behavior, we also demonstrated that application of SOD or AZ is neuroprotective after ischemic injury. Brain slices treated with either therapeutic had significantly reduced cell death over 24h, and AZ additionally prevented a decrease in GSH concentration, indicative of an inhibition of oxidative stress and cell damage. SOD efficacy is well defined by scavenging of superoxide anion which plays a damaging role in excitotoxicity, but the exact mechanism of AZ therapeutic efficacy remains to be elucidated in the brain [364, 365]. Regardless of therapeutic mechanism, therapeutic reversion of OGD-induced changes offers promising implications for drug delivery strategies. If SOD or AZ were delivered via rigid carriers similar to PS-PEG nanoparticles that exhibited increased diffusion and microglial uptake after OGD exposure, drug distribution would favorably accumulate in diseased regions. After therapeutic release and reduction of disease phenotype, subsequently administered nanoparticle doses would preferentially sequester in ongoing injury sites compared to recovering or healthy tissue environments. Further investigation of strategies to modulate nanoparticle diffusivity and microglial uptake may result in more effective methods of nanoparticle-mediated therapeutic delivery.

6.4 Conclusions

In this chapter, we probed the effect of OGD-induced brain injury and AZ treatment on nanoparticle interactions with microglia. First, we determined the effect of OGD exposure on markers of injury severity, including cell death and oxidative stress. We observed significant injury responses after 0.5h OGD exposure: a 54.3% increase in cytotoxicity, a 1.7-fold decrease in GSH concentration, and a larger pore distribution in the ECS. We observed an OGD-induced shift in microglial morphology towards more heterogeneity in shapes with overall increased circularity and a decrease in microglial density. Nanoparticle interactions with microglia were dependent on both the nanoparticle platform as well as treatment condition. After 0.5h OGD, microglial internalization of PS-PEG was increased, but uptake of QDs or dendrimers was not enhanced, indicating an important role of nanoparticle material identity in determining extent of phagocytosis after injury. OGD injury did not impede nanoparticle mobility; PS-PEG nanoparticles had a 16.7-fold increase in diffusion after 0.5h OGD compared to that of NC. Treatment with AZ not only effectively reduced OGD cytotoxicity and GSH depletion, but also reverted nanoparticle uptake behavior of PS-PEG and microglial morphology towards that of NC. This study shows OWH slices enabled region-dependent nanoscale probing of live tissue to identify cellular and microstructural changes in diseased and recovering brain microenvironments that can be leveraged for cell-specific uptake of nanoparticles. Additionally, we demonstrate that in ischemic conditions, nanoparticle fate is platform-dependent, providing insights into therapeutic strategy for targeting microglial cells to combat neurological disease.

In the next chapter, we summarize all research completed during the thesis project.

CHAPTER 7: Research Summary

7.1 Nanotherapeutic modulation of excitotoxicity and oxidative stress in acute brain injury

Liao R, Wood T, Nance E*. *Nanobiomedicine, accepted* (2020).

*Corresponding author

Excitotoxicity is a primary pathological disease process that occurs during stroke, traumatic brain injury (TBI), and global brain ischemia such as perinatal asphyxia. Excitotoxicity is triggered by an overabundance of excitatory neurotransmitters within the synapse, causing a detrimental cascade of excessive sodium and calcium influx, generation of reactive oxygen species, mitochondrial damage, and ultimately cell death. There are multiple potential points of intervention to combat excitotoxicity and downstream oxidative stress, yet there are currently no therapeutics clinically approved for this specific purpose. For a therapeutic to be effective against excitotoxicity, the therapeutic must accumulate at the disease site at the appropriate concentration at the right time. Nanotechnology can provide benefits for therapeutic delivery, including overcoming physiological obstacles such as the blood-brain barrier, protect cargo from degradation, and provide controlled release of a drug. This review evaluates the use of nano-based therapeutics to combat excitotoxicity in stroke, TBI, and hypoxia-ischemia encephalopathy (HIE) with an emphasis on mitigating oxidative stress, and consideration of the path forward towards clinical translation.

7.2 Nanoparticle-microglial interaction in the ischemic brain is modulated by injury duration and treatment

Liao R†, Joseph A†, Zhang M, Helmbrecht H, McKenna M, Filteau J, Nance E*. *Bioengineering & Translational Medicine* (2020). e10175.

*Corresponding author, †Authors contributed equally

Cerebral ischemia is a major cause of death in both neonates and adults, and currently has no cure. Nanotechnology represents one promising area of therapeutic development for cerebral ischemia due to the ability of nanoparticles to overcome biological barriers in the brain. Ex vivo injury models have emerged as a high-throughput alternative that can recapitulate disease processes and enable nanoscale probing of the brain microenvironment. In this study, we used oxygen-glucose deprivation (OGD) to model ischemic injury and studied nanoparticle interaction with microglia, resident immune cells in the brain that are of increasing interest for therapeutic delivery. By measuring cell death and glutathione production, we evaluated the effect of OGD exposure time and treatment with azithromycin (AZ) on slice health. We found a robust injury response with 0.5 hours of OGD exposure and effective treatment after immediate application of AZ. We observed an OGD-induced shift in microglial morphology towards increased heterogeneity and circularity, and a decrease in microglial number, which was reversed after treatment. OGD enhanced diffusion of polystyrene-poly(ethylene glycol) (PS-PEG) nanoparticles, improving transport and ability to reach target cells. While microglial uptake of dendrimers or quantum dots (QDs) was not enhanced after injury, internalization of PS-PEG was significantly increased. For PS-PEG, azithromycin (AZ) treatment restored microglial uptake to normal control levels. Our results suggest that different nanoparticle platforms should be carefully screened before application and upon doing so, disease-mediated changes in the brain microenvironment can be leveraged by nanoscale drug delivery devices for enhanced cell interaction.

7.3 Enzymatic protection and biocompatibility screening of enzyme-loaded polymeric nanoparticles for neurotherapeutic applications

Liao R, Pon J, Chungyoun M, Nance E*. *Biomaterials* (2020). 120238.

*Corresponding author

Polymeric nanoparticles provide a non-invasive strategy for enhancing the delivery of labile hydrophilic enzymatic cargo for neurological disease applications. One of the most common polymeric materials, poly(lactic-co-glycolic acid) (PLGA) copolymerized with poly(ethylene glycol) (PEG) is widely studied due to its biocompatible and biodegradable nature. Although PLGA-PEG nanoparticles are generally known to be non-toxic and protect enzymatic cargo from degradative proteases, different formulation parameters including surfactant, organic solvent, sonication times, and formulation method can all impact the final nanoparticle characteristics. We show that 30s sonication double emulsion (DE)-formulated nanoparticles achieved the highest enzymatic activity and provided the greatest enzymatic activity protection in degradative conditions, while nanoprecipitation (NPPT)-formulated nanoparticles exhibited no protection compared to free catalase. However, the same DE nanoparticles also caused significant toxicity on excitotoxicity-induced brain tissue slices, but not on healthy or neuroinflammation-induced tissue. We narrowed the culprit of toxicity to specifically sonication of PLGA-PEG polymer with dichloromethane (DCM) as the organic solvent, independent of surfactant type. We also discovered that toxicity was oxidative stress-dependent, but that increased toxicity was not enacted through increasing oxidative stress. Furthermore, no PEG degradation or aldehyde, alcohol, or carboxylic acid functional groups were detected after sonication. We identified that inclusion of free PEG along with PLGA-PEG polymer during the emulsification phases or replacing DCM with trichloromethane (TCM, chloroform) produced biocompatible polymeric nanoparticle formulations that still provided enzymatic protection. This work encourages thorough screening of nanoparticle toxicity and cargo-protective capabilities for the development of enzyme-loaded polymeric nanoparticles for the treatment of disease.

7.4 Superoxide dismutase reduces monosodium glutamate-induced injury in an organotypic whole hemisphere brain slice model of excitotoxicity

Liao R, Wood T, Nance E*. *Journal of Biological Engineering* (2020). 14.1: 1-12.

*Corresponding author

Background: Knowledge of glutamate excitotoxicity has increased substantially over the past few decades, with multiple proposed pathways involved in inflicting damage. We sought to develop a monosodium glutamate (MSG) exposed *ex vivo* organotypic whole hemisphere (OWH) brain slice model of excitotoxicity to study excitotoxic processes and screen the efficacy of superoxide dismutase (SOD).

Results: The OWH model is a reproducible platform with high cell viability and retained cellular morphology. OWH slices exposed to MSG induced significant cytotoxicity and downregulation of neuronal excitation-related gene expression. The OWH brain slice model has enabled us to isolate and study components of excitotoxicity, distinguishing the effects of glutamate excitation, hyperosmolar stress, and inflammation. We find that extracellularly administered SOD is significantly protective in inhibiting cell death and restoring healthy mitochondrial morphology. SOD efficacy suggests that superoxide scavenging is a promising therapeutic strategy in excitotoxic injury.

Conclusions: Using OWH brain slice models, we can obtain a better understanding of the pathological mechanisms of excitotoxic injury, and more rapidly screen potential therapeutics.

7.5 Determining dominant driving forces affecting controlled protein release from polymeric nanoparticles

Smith J†, Sprenger K†, Liao R, Joseph A, Nance E*, Pfaendtner J*. *Biointerphases* (2017). 12.2: 02D412.

*Corresponding author, †Authors contributed equally

Enzymes play a critical role in many applications in biology and medicine as potential therapeutics. One specific area of interest is enzyme encapsulation in polymer nanostructures, which have applications in drug delivery and catalysis. A detailed understanding of the mechanisms governing protein/polymer interactions is crucial for optimizing the performance of these complex systems for different applications. Using a combined computational and experimental approach, this study aims to quantify the relative importance of molecular and mesoscale driving forces to protein release from polymeric nanoparticles. Classical molecular dynamics (MD) simulations have been performed on bovine serum albumin (BSA) in aqueous solutions with oligomeric surrogates of poly(lactic-co-glycolic acid) copolymer, poly(styrene)-poly(lactic acid) copolymer, and poly(lactic acid). The simulated strength and location of polymer surrogate binding to the surface of BSA have been compared to experimental BSA release rates from nanoparticles formulated with these same polymers. Results indicate that the self-interaction tendencies of the polymer surrogates and other macroscale properties may play governing roles in protein release. Additional MD simulations of BSA in solution with poly(styrene)-acrylate copolymer reveal the possibility of enhanced control over the enzyme encapsulation process by tuning polymer self-interaction. Last, the authors find consistent protein surface binding preferences across simulations performed with polymer surrogates of varying lengths, demonstrating that protein/polymer interactions can be understood in part by studying the interactions and affinity of proteins with small polymer surrogates in solution.

7.6 Systems-level thinking for nanoparticle-mediated therapeutic delivery to neurological diseases.

Curtis C, Zhang M, Liao R, Wood T, Nance E*. *WIREs Nanomedicine and Nanobiotechnology* (2017) 9.2: e1422.

*Corresponding author

Neurological diseases account for 13% of the global burden of disease. As a result, treating these diseases costs $750 billion a year. Nanotechnology, which consists of small (~1–100 nm) but highly tailorable platforms, can provide significant opportunities for improving therapeutic delivery to the brain. Nanoparticles can increase drug solubility, overcome the blood–brain and brain penetration barriers, and provide timed release of a drug at a site of interest. Many researchers have successfully used nanotechnology to overcome individual barriers to therapeutic delivery to the brain, yet no platform has translated into a standard of care for any neurological disease. The challenge in translating nanotechnology platforms into clinical use for patients with neurological disease necessitates a new approach to: (1) collect information from the fields associated with understanding and treating brain diseases and (2) apply that information using scalable technologies in a clinically-relevant way. This approach requires systems level thinking to integrate an understanding of biological barriers to therapeutic intervention in the brain with the engineering of nanoparticle material properties to overcome those barriers. To demonstrate how a systems perspective can tackle the challenge of treating neurological diseases using nanotechnology, we will first present physiological barriers to drug delivery in the brain and common neurological disease hallmarks that influence these barriers. We will then analyze the design of nanotechnology platforms in preclinical *in vivo* efficacy studies for treatment of neurological disease, and map concepts for the interaction of nanoparticle physicochemical properties and pathophysiological hallmarks in the brain.

APPENDIX A: Supplementary Figures to Chapter 4

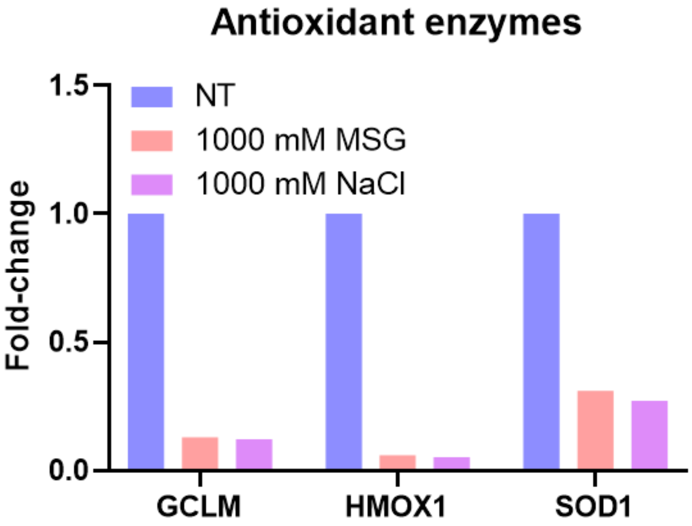

Figure S4.1: Fold-changes of antioxidant mRNAs for NT, 1000 mM MSG, and 1000 mM NaCl slices at 6h (n=1).

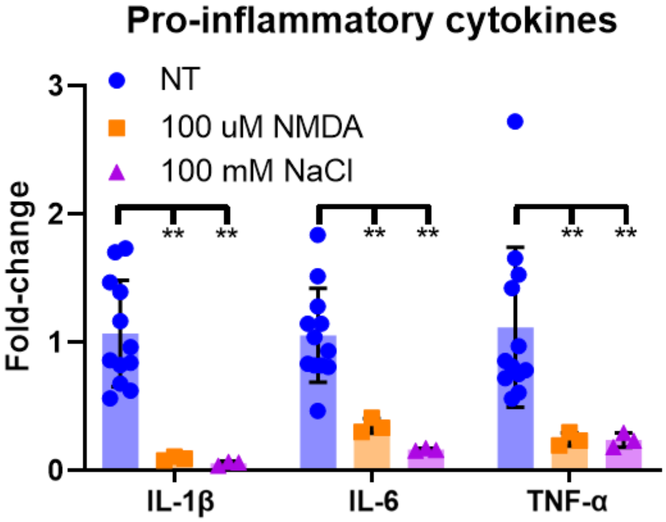

Figure S4.2: Fold-changes of pro-inflammatory mRNAs for NT, 100 µM NMDA, and 100 mM NaCl slices at 6h (n=3-12).

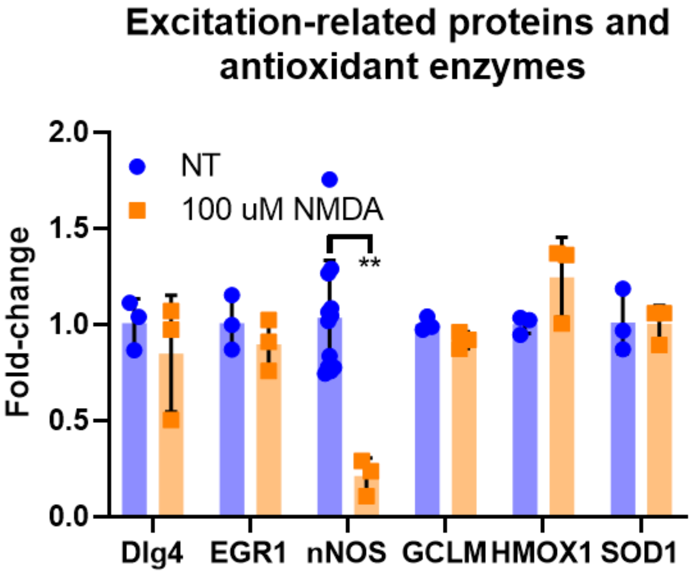

Figure S4.3: Fold-changes of excitation-related proteins and antioxidant enzyme mRNAs mRNAs for NT and 100 μM NMDA slices at 6h (n=3-12).

APPENDIX B: Supplementary Figures to Chapter 5

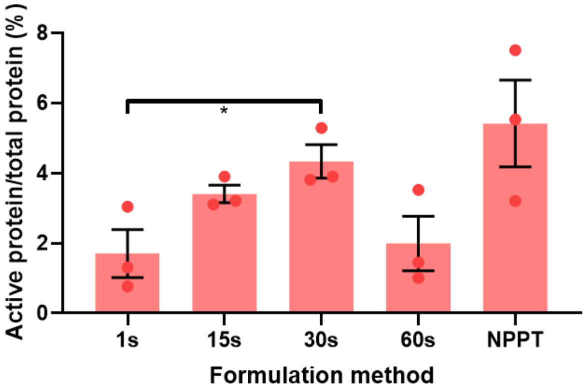

Figure S5.1: Active/total protein ratio for CHA nanoparticle formulations determined from catalase activity and protein concentration via BCA assay (n=3). Data are reported as mean ± SEM.

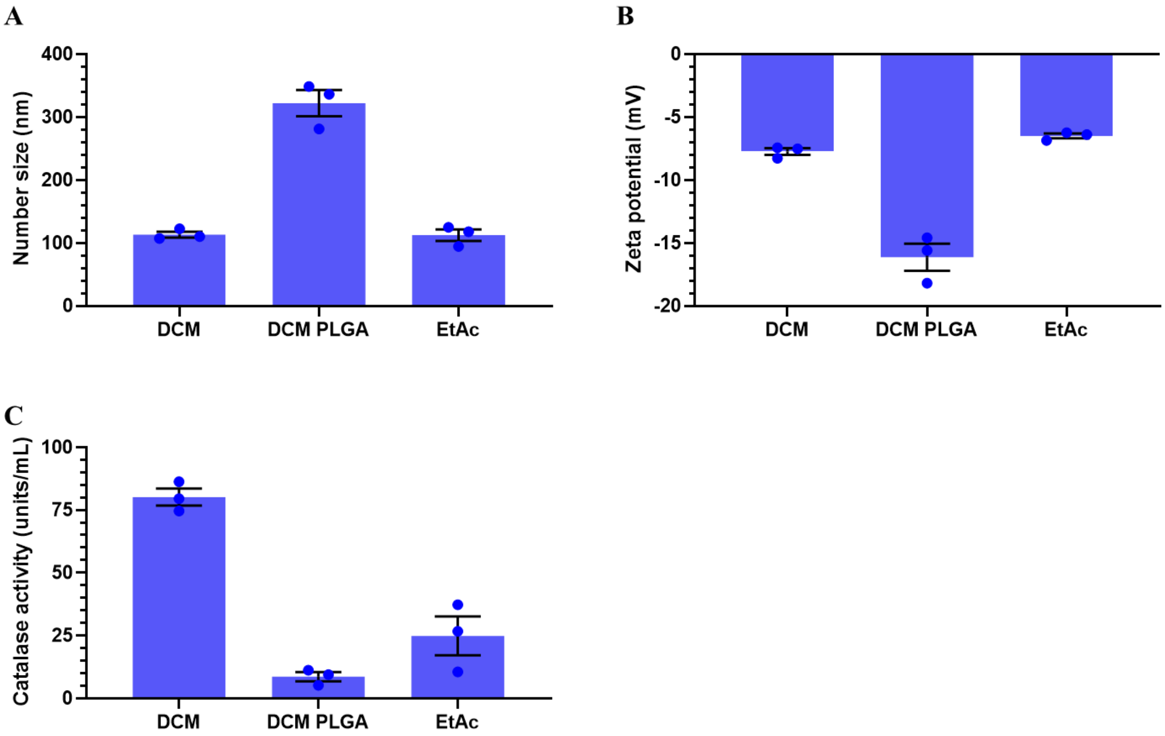

Figure S5.2: Characteristics of PVA nanoparticles formulated with the alternative DE conditions. A) nanoparticle number mean sizes, B) nanoparticle ζ-potentials, and C) nanoparticle catalase activities were determined for 30s DE nanoparticle formulations with PLGA instead of PLGA-PEG polymer (DCM PLGA) and EtAc instead of DCM organic solvent (EtAc) (n=3). DCM data is the same data as displayed in Figure 5.1. Data are reported as mean ± SEM.

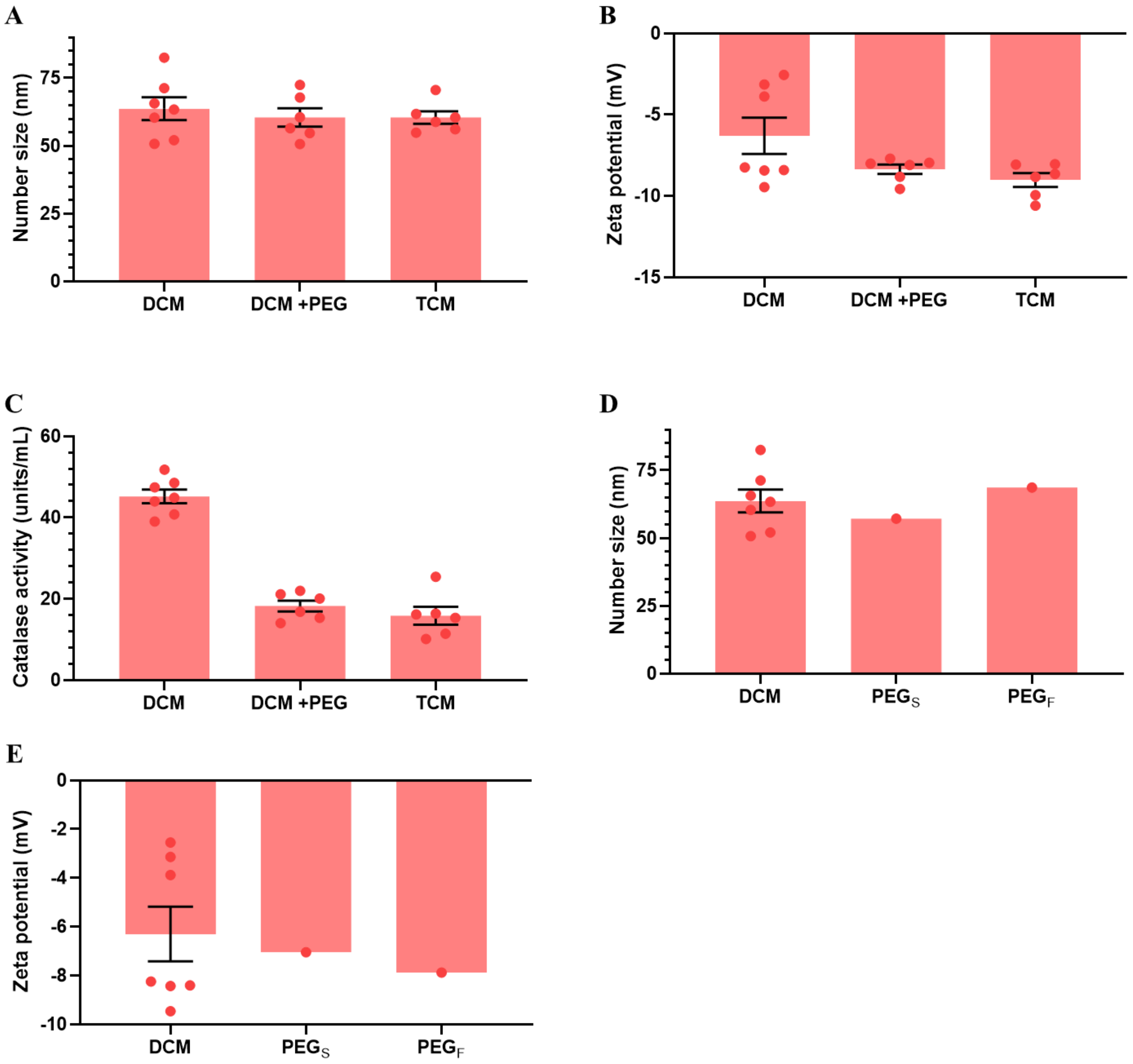

Figure S5.3: Characteristics of CHA nanoparticles formulated with the alternative non-toxic DE conditions. A) nanoparticle number mean sizes, B) nanoparticle ζ-potentials, and C) nanoparticle catalase activities for 30s DE nanoparticle formulations with PLGA-PEG+PEG polymer (DCM +PEG) and TCM instead of DCM organic solvent (TCM) (n=6). D) nanoparticle number mean sizes and E) nanoparticle ζ-potentials for PEG$_S$ and PEG$_F$ nanoparticles (n=1). DCM data is the same data as displayed in Figure 5.1. Data are reported as mean ± SEM.

APPENDIX C: Supplementary Figures and Tables to Chapter 6

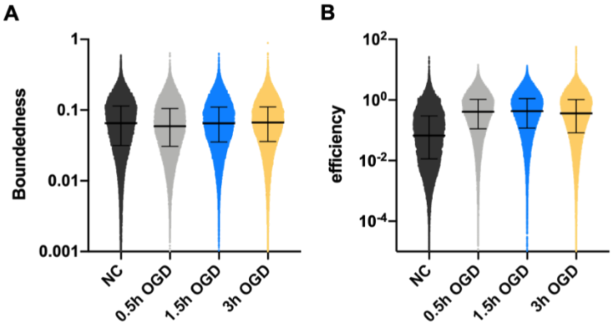

Figure S6.1: Nanoparticle boundedness (A) and efficiency (B) calculated for each trajectory from all videos (n=10) in all slices (n=3) per group (1 dot = 1 trajectory).

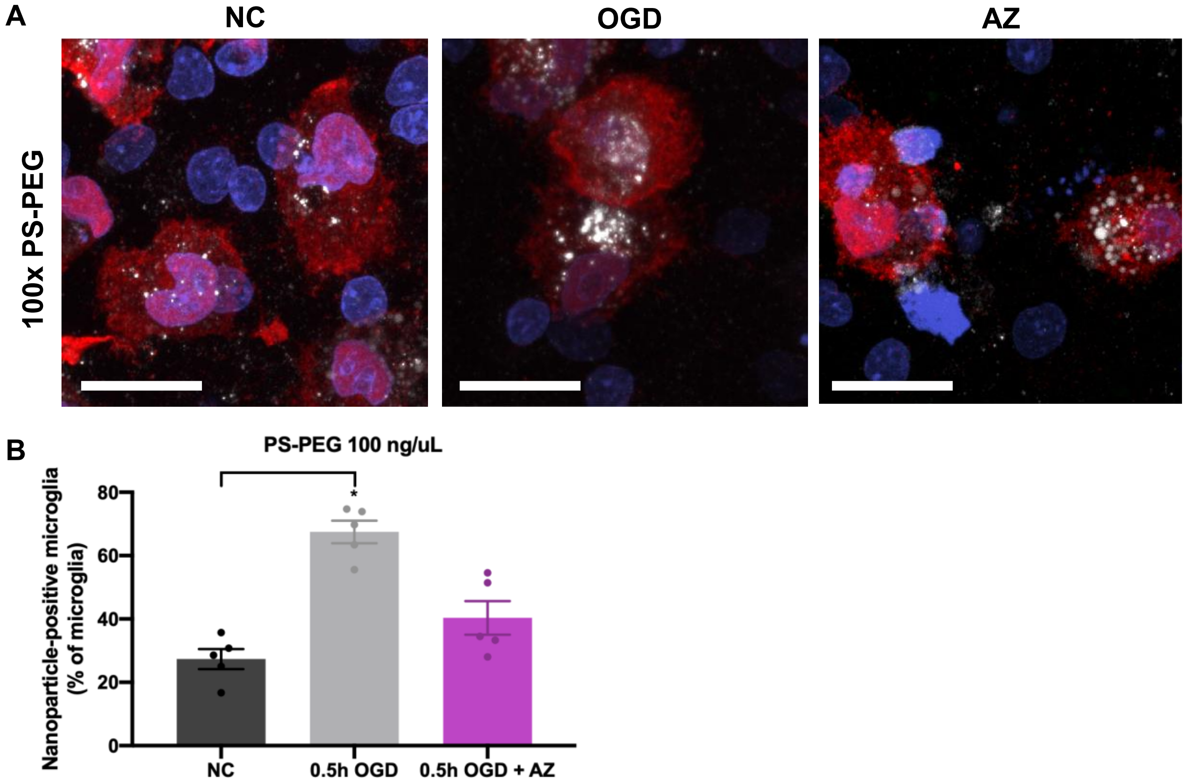

Figure S6.2: Microglial uptake of 100ng/µL PS-PEG nanoparticles. A) Representative confocal images of PS-PEG (white) and microglia (red) after administration of 100ng/µL(a 100-fold higher dose than the representative data in Figure 5). All scale bars represent 20 µm and cell nuclei (blue) are also shown. B) Flow cytometry results indicate nanoparticle-positive microglia as a proportion of all microglia in each treatment group.

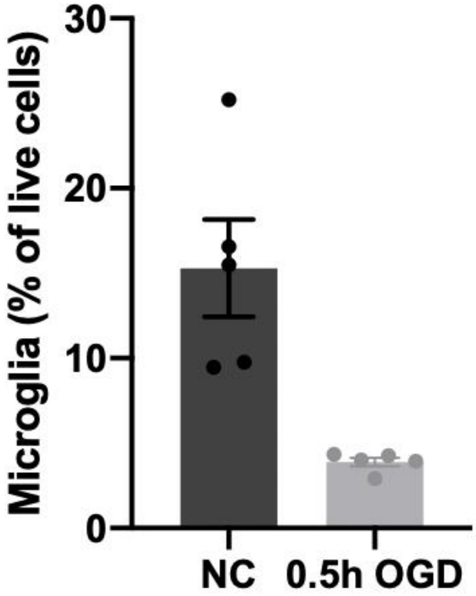

Figure S6.3: Flow cytometry results of microglia as a proportion of all live cells in the NC and 0.5h OGD groups at 25h after injury.

Table S6.1. Average circularity of microglia by shape mode for a given experimental condition.

Experimental Condition	Shape Mode					
	1	**2**	**3**	**4**	**5**	**Average**
NT	0.53	0.48	0.50	0.53	0.47	0.50
OGD	0.63	0.59	0.78	0.85	0.61	0.69
OGD+AZ	0.55	0.48	0.57	0.57	0.49	0.53

Table S6.2. Physicochemical properties of PS-PEG used in MPT and nanoparticle uptake studies. A non-PEG coated PS particle is included for comparison. Nanoparticles (n=3 batches per particle type) were characterized in terms of hydrodynamic diameter, mean surface charge (ζ-potential), and the polydispersity index (PDI) by dynamic light scattering at 25°C and pH 7.2 in 10 mM NaCl.

Nanoparticle Type	Number Mean ± SEM (nm)	Intensity Mean ± SEM (nm)	PDI	ζ-potential ± SEM (mV)
PS-COOH	39.1 ± 0.49	53.2 ± 0.58	0.044	-37.5 ± 0.74
PS-PEG	51.4 ± 0.96	66.9 ± 0.40	0.027	-0.59 ± 0.10

BIBLIOGRAPHY

1. Gooch, C.L., E. Pracht, and A.R. Borenstein, *The burden of neurological disease in the United States: A summary report and call to action.* Ann Neurol, 2017. **81**(4): p. 479-484.
2. Alavijeh, M.S., et al., *Drug metabolism and pharmacokinetics, the blood-brain barrier, and central nervous system drug discovery.* NeuroRx, 2005. **2**(4): p. 554-71.
3. Vos, T., et al., *Global, regional, and national incidence, prevalence, and years lived with disability for 328 diseases and injuries for 195 countries, 1990–2016: a systematic analysis for the Global Burden of Disease Study 2016.* The Lancet, 2017. **390**(10100): p. 1211-1259.
4. Taylor, C.A., et al., *Traumatic Brain Injury-Related Emergency Department Visits, Hospitalizations, and Deaths - United States, 2007 and 2013.* MMWR Surveill Summ, 2017. **66**(9): p. 1-16.
5. Cummings, J.L. and D.V. Jeste, *Alzheimer's disease and its management in the year 2010.* Psychiatr Serv, 1999. **50**(9): p. 1173-7.
6. Meldrum, B.S., *Glutamate as a neurotransmitter in the brain: review of physiology and pathology.* The Journal of nutrition, 2000. **130**(4): p. 1007S-1015S.
7. Wang, Y. and Z.-h. Qin, *Molecular and cellular mechanisms of excitotoxic neuronal death.* Apoptosis, 2010. **15**(11): p. 1382-1402.
8. Dong, X.-x., Y. Wang, and Z.-h. Qin, *Molecular mechanisms of excitotoxicity and their relevance to pathogenesis of neurodegenerative diseases.* Acta Pharmacologica Sinica, 2009. **30**(4): p. 379-387.
9. Beal, M.F., *Role of excitotoxicity in human neurological disease.* Curr Opin Neurobiol, 1992. **2**(5): p. 657-62.
10. O'Callaghan, J.P., K. Sriram, and D.B. Miller, *Defining "neuroinflammation".* Ann N Y Acad Sci, 2008. **1139**: p. 318-30.
11. Wellen, K.E. and G.S. Hotamisligil, *Inflammation, stress, and diabetes.* J Clin Invest, 2005. **115**(5): p. 1111-9.
12. Frank, M.G., et al., *Stress-induced neuroinflammatory priming: A liability factor in the etiology of psychiatric disorders.* Neurobiol Stress, 2016. **4**: p. 62-70.
13. Tohidpour, A., et al., *Neuroinflammation and Infection: Molecular Mechanisms Associated with Dysfunction of Neurovascular Unit.* Front Cell Infect Microbiol, 2017. **7**: p. 276.
14. Kumar, A. and D.J. Loane, *Neuroinflammation after traumatic brain injury: opportunities for therapeutic intervention.* Brain, behavior, and immunity, 2012. **26**(8): p. 1191-1201.
15. Romero, R., et al., *The role of inflammation and infection in preterm birth.* Semin Reprod Med, 2007. **25**(1): p. 21-39.
16. Hagberg, H., P. Gressens, and C. Mallard, *Inflammation during fetal and neonatal life: Implications for neurologic and neuropsychiatric disease in children and adults.* Annals of Neurology, 2012. **71**(4): p. 444-457.
17. Vargas, D.L., et al., *Neuroglial activation and neuroinflammation in the brain of patients with autism.* Ann Neurol, 2005. **57**(1): p. 67-81.
18. Zhang, S.C., et al., *Reactive microglia in dysmyelination and demyelination.* Glia, 2001. **34**(2): p. 101-109.
19. Kielian, T., *Neuroinflammation: good, bad, or indifferent?* J Neurochem, 2014. **130**(1): p. 1-3.
20. Neumann, H., M.R. Kotter, and R.J.M. Franklin, *Debris clearance by microglia: an essential link between degeneration and regeneration.* Brain, 2009. **132**: p. 288-295.
21. Block, M.L., L. Zecca, and J.S. Hong, *Microglia-mediated neurotoxicity: uncovering the molecular mechanisms.* Nature Reviews Neuroscience, 2007. **8**(1): p. 57-69.

22. Haynes, R.L., et al., *Nitrosative and oxidative injury to premyelinating oligodendrocytes in periventricular leukomalacia.* Journal of Neuropathology and Experimental Neurology, 2003. **62**(5): p. 441-450.
23. Perry, V.H., J.A.R. Nicoll, and C. Holmes, *Microglia in neurodegenerative disease.* Nature Reviews Neurology, 2010. **6**(4): p. 193-201.
24. Barger, S.W., et al., *Glutamate release from activated microglia requires the oxidative burst and lipid peroxidation.* Journal of Neurochemistry, 2007. **101**(5): p. 1205-1213.
25. Sofroniew, M.V., *Astrocyte barriers to neurotoxic inflammation.* Nat Rev Neurosci, 2015. **16**(5): p. 249-63.
26. Sofroniew, M.V., *Molecular dissection of reactive astrogliosis and glial scar formation.* Trends Neurosci, 2009. **32**(12): p. 638-47.
27. Maragakis, N.J. and J.D. Rothstein, *Mechanisms of Disease: astrocytes in neurodegenerative disease.* Nat Clin Pract Neurol, 2006. **2**(12): p. 679-89.
28. Chen, W.W., X. Zhang, and W.J. Huang, *Role of neuroinflammation in neurodegenerative diseases (Review).* Mol Med Rep, 2016. **13**(4): p. 3391-6.
29. Prentice, H., J.P. Modi, and J.Y. Wu, *Mechanisms of Neuronal Protection against Excitotoxicity, Endoplasmic Reticulum Stress, and Mitochondrial Dysfunction in Stroke and Neurodegenerative Diseases.* Oxidative Medicine and Cellular Longevity, 2015.
30. Singh, P., et al., *Prolonged glutamate excitotoxicity: Effects on mitochondrial antioxidants and antioxidant enzymes.* Molecular and Cellular Biochemistry, 2003. **243**(1-2): p. 139-145.
31. Matthews, C.C., et al., *Enzymatic degradation protects neurons from glutamate excitotoxicity.* Journal of Neurochemistry, 2000. **75**(3): p. 1045-1052.
32. Ames, B.N., M.K. Shigenaga, and T.M. Hagen, *Oxidants, Antioxidants, and the Degenerative Diseases of Aging.* Proceedings of the National Academy of Sciences of the United States of America, 1993. **90**(17): p. 7915-7922.
33. Goldberg, M.P. and D.W. Choi, *Combined oxygen and glucose deprivation in cortical cell culture: calcium-dependent and calcium-independent mechanisms of neuronal injury.* J Neurosci, 1993. **13**(8): p. 3510-24.
34. Kannan, R.M., et al., *Emerging concepts in dendrimer-based nanomedicine: from design principles to clinical applications.* J Intern Med, 2014. **276**(6): p. 579-617.
35. Abbott, N.J., et al., *Structure and function of the blood-brain barrier.* Neurobiol Dis, 2010. **37**(1): p. 13-25.
36. Mohs, R.C. and N.H. Greig, *Drug discovery and development: Role of basic biological research.* Alzheimers Dement (N Y), 2017. **3**(4): p. 651-657.
37. Kreuter, J., et al., *Apolipoprotein-mediated transport of nanoparticle-bound drugs across the blood-brain barrier.* J Drug Target, 2002. **10**(4): p. 317-25.
38. Danhier, F., et al., *PLGA-based nanoparticles: an overview of biomedical applications.* J Control Release, 2012. **161**(2): p. 505-22.
39. Wang, Y., et al., *Discovery of FDA-approved drugs as inhibitors of fatty acid binding protein 4 using molecular docking screening.* J Chem Inf Model, 2014. **54**(11): p. 3046-50.
40. Sah, E. and H. Sah, *Recent trends in preparation of poly (lactide-co-glycolide) nanoparticles by mixing polymeric organic solution with antisolvent.* Journal of Nanomaterials, 2015. **2015**.
41. Nance, E.A., et al., *A dense poly (ethylene glycol) coating improves penetration of large polymeric nanoparticles within brain tissue.* Science translational medicine, 2012. **4**(149): p. 149ra119-149ra119.
42. Noraberg, J., B.W. Kristensen, and J. Zimmer, *Markers for neuronal degeneration in organotypic slice cultures.* Brain Res Brain Res Protoc, 1999. **3**(3): p. 278-90.

43. Noraberg, J., *Organotypic brain slice cultures: an efficient and reliable method for neurotoxicological screening and mechanistic studies.* Altern Lab Anim, 2004. **32**(4): p. 329-37.
44. Saeidnia, S., A. Manayi, and M. Abdollahi, *From in vitro Experiments to in vivo and Clinical Studies; Pros and Cons.* Curr Drug Discov Technol, 2015. **12**(4): p. 218-24.
45. Stanimirovic, D.B., et al., *Blood-brain barrier models: in vitro to in vivo translation in preclinical development of CNS-targeting biotherapeutics.* Expert Opin Drug Discov, 2015. **10**(2): p. 141-55.
46. Rio, D.C., et al., *Purification of RNA using TRIzol (TRI reagent).* Cold Spring Harbor Protocols, 2010. **2010**(6): p. pdb. prot5439.
47. Beers, R.F. and I.W. Sizer, *A spectrophotometric method for measuring the breakdown of hydrogen peroxide by catalase.* J Biol chem, 1952. **195**(1): p. 133-140.
48. Dziubla, T.D., A. Karim, and V.R. Muzykantov, *Polymer nanocarriers protecting active enzyme cargo against proteolysis.* J Control Release, 2005. **102**(2): p. 427-39.
49. Wu, P.H., et al., *Evolution of cellular morpho-phenotypes in cancer metastasis.* Sci Rep, 2015. **5**: p. 18437.
50. Virtanen, P., et al., *SciPy 1.0: fundamental algorithms for scientific computing in Python.* Nat Methods, 2020. **17**(3): p. 261-272.
51. Pérez, F. and B.E. Granger, *IPython: a system for interactive scientific computing.* Computing in Science & Engineering, 2007. **9**(3): p. 21-29.
52. Oliphant, T.E., *A guide to NumPy*. Vol. 1. 2006: Trelgol Publishing USA.
53. Pedregosa, F., et al., *Scikit-learn: Machine learning in Python.* the Journal of machine Learning research, 2011. **12**: p. 2825-2830.
54. McQuin, C., et al., *CellProfiler 3.0: Next-generation image processing for biology.* PLoS Biol, 2018. **16**(7): p. e2005970.
55. Nance, E., *Brain-Penetrating Nanoparticles for Analysis of the Brain Microenvironment.* Methods Mol Biol, 2017. **1570**: p. 91-104.
56. Mishra, M.K., et al., *Dendrimer brain uptake and targeted therapy for brain injury in a large animal model of hypothermic circulatory arrest.* ACS Nano, 2014. **8**(3): p. 2134-47.
57. Lesniak, W.G., et al., *Biodistribution of fluorescently labeled PAMAM dendrimers in neonatal rabbits: effect of neuroinflammation.* Mol Pharm, 2013. **10**(12): p. 4560-71.
58. Zhang, F., et al., *Microglial migration and interactions with dendrimer nanoparticles are altered in the presence of neuroinflammation.* J Neuroinflammation, 2016. **13**(1): p. 65.
59. Zhang, M., et al., *Quantum Dot Cellular Uptake and Toxicity in the Developing Brain: Implications for Use as Imaging Probes.* Nanoscale Adv, 2019. **1**(9): p. 3424-3442.
60. Curtis, C., A. Rokem, and E. Nance, *diff_classifier: Parallelization of multi-particle tracking video analyses.* J Open Source Softw, 2019. **4**(36).
61. Amsden, B., *An obstruction-scaling model for diffusion in homogeneous hydrogels.* Macromolecules, 1999. **32**(3): p. 874-879.
62. Benjamin, E.J., et al., *Heart Disease and Stroke Statistics-2017 Update: A Report From the American Heart Association.* Circulation, 2017. **135**(10): p. e146-e603.
63. Kurinczuk, J.J., M. White-Koning, and N. Badawi, *Epidemiology of neonatal encephalopathy and hypoxic-ischaemic encephalopathy.* Early Hum Dev, 2010. **86**(6): p. 329-38.
64. Peterson, A.B., et al., *Surveillance report of traumatic brain injury-related emergency department visits, hospitalizations, and deaths, United States, 2014.* 2019.
65. Eunson, P., *The long-term health, social, and financial burden of hypoxic-ischaemic encephalopathy.* Dev Med Child Neurol, 2015. **57 Suppl 3**: p. 48-50.
66. Coronado, V., et al., *The epidemiology and prevention of TBI.* Brain Injury Medicine. New York, NY: Demos, 2012: p. 45-56.

67. Fujikawa, D.G., *The role of excitotoxic programmed necrosis in acute brain injury.* Computational and structural biotechnology journal, 2015. **13**: p. 212-221.
68. Dantzer, R. and A.K. Walker, *Is there a role for glutamate-mediated excitotoxicity in inflammation-induced depression?* Journal of neural transmission, 2014. **121**(8): p. 925-932.
69. Curtis, C., et al., *Systems-level thinking for nanoparticle-mediated therapeutic delivery to neurological diseases.* Wiley Interdiscip Rev Nanomed Nanobiotechnol, 2017. **9**(2).
70. Südhof, T.C., *Calcium control of neurotransmitter release.* Cold Spring Harbor perspectives in biology, 2012. **4**(1): p. a011353.
71. Mahmoud, S., et al., *Astrocytes maintain glutamate homeostasis in the CNS by controlling the balance between glutamate uptake and release.* Cells, 2019. **8**(2): p. 184.
72. Girouard, H., et al., *NMDA receptor activation increases free radical production through nitric oxide and NOX2.* Journal of Neuroscience, 2009. **29**(8): p. 2545-2552.
73. Lewerenz, J. and P. Maher, *Chronic glutamate toxicity in neurodegenerative diseases—what is the evidence?* Frontiers in neuroscience, 2015. **9**: p. 469.
74. Swanson, R.A., K. Farrell, and R.P. Simon, *Acidosis causes failure of astrocyte glutamate uptake during hypoxia.* Journal of Cerebral Blood Flow & Metabolism, 1995. **15**(3): p. 417-424.
75. Veenith, T., S.S. Goon, and R.M. Burnstein, *Molecular mechanisms of traumatic brain injury: the missing link in management.* World Journal of Emergency Surgery, 2009. **4**(1): p. 7.
76. Kaur, P. and S. Sharma, *Recent advances in pathophysiology of traumatic brain injury.* Current neuropharmacology, 2018. **16**(8): p. 1224-1238.
77. Fellman, V. and K.O. Raivio, *Reperfusion injury as the mechanism of brain damage after perinatal asphyxia.* Pediatric research, 1997. **41**(5): p. 599-606.
78. Hackett, J.T. and T. Ueda, *Glutamate release.* Neurochemical research, 2015. **40**(12): p. 2443-2460.
79. Leaw, B., et al., *Mitochondria, Bioenergetics and Excitotoxicity: New Therapeutic Targets in Perinatal Brain Injury.* Front Cell Neurosci, 2017. **11**: p. 199.
80. Brookes, P.S., et al., *Calcium, ATP, and ROS: a mitochondrial love-hate triangle.* Am J Physiol Cell Physiol, 2004. **287**(4): p. C817-33.
81. Dikalov, S., et al., *Crosstalk between mitochondrial ROS and NADPH oxidases in cardiovascular and degenerative diseases: application of mitochondria-targeted antioxidants.* Free Radical Biology and Medicine, 2011(51): p. S85-S86.
82. Nazarewicz, R.R., et al., *Nox2 as a potential target of mitochondrial superoxide and its role in endothelial oxidative stress.* American Journal of Physiology-Heart and Circulatory Physiology, 2013. **305**(8): p. H1131-H1140.
83. Joseph, L.C., et al., *Inhibition of NAPDH oxidase 2 (NOX2) prevents oxidative stress and mitochondrial abnormalities caused by saturated fat in cardiomyocytes.* PloS one, 2016. **11**(1).
84. Silva, G.B. and J.L. Garvin, *Rac1 mediates NaCl-induced superoxide generation in the thick ascending limb.* American Journal of Physiology-Renal Physiology, 2010. **298**(2): p. F421-F425.
85. Landmesser, U., et al., *Oxidation of tetrahydrobiopterin leads to uncoupling of endothelial cell nitric oxide synthase in hypertension.* The Journal of clinical investigation, 2003. **111**(8): p. 1201-1209.
86. Alper, G., et al., *MAO inhibitors and oxidant stress in aging brain tissue.* European neuropsychopharmacology, 1999. **9**(3): p. 247-252.
87. Atlante, A., et al., *Glutamate neurotoxicity in rat cerebellar granule cells: a major role for xanthine oxidase in oxygen radical formation.* Journal of neurochemistry, 1997. **68**(5): p. 2038-2045.
88. Wu, M.-y., et al., *Current mechanistic concepts in ischemia and reperfusion injury.* Cellular Physiology and Biochemistry, 2018. **46**(4): p. 1650-1667.

89. Beckman, J.S. and W.H. Koppenol, *Nitric oxide, superoxide, and peroxynitrite: the good, the bad, and ugly.* Am J Physiol, 1996. **271**(5 Pt 1): p. C1424-37.
90. Kahraman, S., et al., *Permeability transition pore-dependent and PARP-mediated depletion of neuronal pyridine nucleotides during anoxia and glucose deprivation.* J Bioenerg Biomembr, 2015. **47**(1-2): p. 53-61.
91. Adam-Vizi, V. and A.A. Starkov, *Calcium and mitochondrial reactive oxygen species generation: how to read the facts.* J Alzheimers Dis, 2010. **20 Suppl 2**: p. S413-26.
92. Kowaltowski, A.J., R.F. Castilho, and A.E. Vercesi, *Mitochondrial permeability transition and oxidative stress.* FEBS Lett, 2001. **495**(1-2): p. 12-5.
93. Morciano, G., et al., *Molecular identity of the mitochondrial permeability transition pore and its role in ischemia-reperfusion injury.* J Mol Cell Cardiol, 2015. **78**: p. 142-53.
94. Qin, Y.Y., et al., *Combined NADPH and the NOX inhibitor apocynin provides greater anti-inflammatory and neuroprotective effects in a mouse model of stroke.* Free Radic Biol Med, 2017. **104**: p. 333-345.
95. Duchen, M.R., *Mitochondria and calcium: from cell signalling to cell death.* J Physiol, 2000. **529 Pt 1**: p. 57-68.
96. Zorov, D.B., M. Juhaszova, and S.J. Sollott, *Mitochondrial reactive oxygen species (ROS) and ROS-induced ROS release.* Physiological reviews, 2014. **94**(3): p. 909-950.
97. Mander, P.K., A. Jekabsone, and G.C. Brown, *Microglia proliferation is regulated by hydrogen peroxide from NADPH oxidase.* The Journal of Immunology, 2006. **176**(2): p. 1046-1052.
98. Veal, E. and A. Day, *Hydrogen peroxide as a signaling molecule*. 2011, Mary Ann Liebert, Inc. 140 Huguenot Street, 3rd Floor New Rochelle, NY 10801 USA.
99. Joseph, A., et al., *Curcumin-loaded polymeric nanoparticles for neuroprotection in neonatal rats with hypoxic-ischemic encephalopathy.* Nano Research, 2018. **11**(10): p. 5670-5688.
100. Haroon, E., et al., *Increased inflammation and brain glutamate define a subtype of depression with decreased regional homogeneity, impaired network integrity, and anhedonia.* Translational psychiatry, 2018. **8**(1): p. 1-11.
101. McGeer, P.L. and E.G. McGeer, *Inflammation and neurodegeneration in Parkinson's disease.* Parkinsonism & related disorders, 2004. **10**: p. S3-S7.
102. Ceulemans, A.-G., et al., *The dual role of the neuroinflammatory response after ischemic stroke: modulatory effects of hypothermia.* Journal of neuroinflammation, 2010. **7**(1): p. 74.
103. Liu, F. and L.D. Mccullough, *Inflammatory responses in hypoxic ischemic encephalopathy.* Acta Pharmacologica Sinica, 2013. **34**(9): p. 1121-1130.
104. Zou, H., et al., *Neuroprotective, neuroplastic, and neurobehavioral effects of daily treatment with levetiracetam in experimental traumatic brain injury.* Neurorehabilitation and neural repair, 2013. **27**(9): p. 878-888.
105. Shetty, A.K., *Prospects of levetiracetam as a neuroprotective drug against status epilepticus, traumatic brain injury, and stroke.* Front Neurol, 2013. **4**: p. 172.
106. Ikonomidou, C. and L. Turski, *Why did NMDA receptor antagonists fail clinical trials for stroke and traumatic brain injury?* Lancet Neurol, 2002. **1**(6): p. 383-6.
107. Lee, S.G., et al., *Mechanism of ceftriaxone induction of excitatory amino acid transporter-2 expression and glutamate uptake in primary human astrocytes.* J Biol Chem, 2008. **283**(19): p. 13116-23.
108. Lin, C.L., et al., *Glutamate transporter EAAT2: a new target for the treatment of neurodegenerative diseases.* Future Med Chem, 2012. **4**(13): p. 1689-700.
109. Vermeij, J.D., et al., *Preventive Ceftriaxone in Patients with Stroke Treated with Intravenous Thrombolysis: Post Hoc Analysis of the Preventive Antibiotics in Stroke Study.* Cerebrovasc Dis, 2016. **42**(5-6): p. 361-369.

110. Cook, D.J., L. Teves, and M. Tymianski, *Treatment of stroke with a PSD-95 inhibitor in the gyrencephalic primate brain.* Nature, 2012. **483**(7388): p. 213-7.
111. Sun, H.S., et al., *Effectiveness of PSD95 inhibitors in permanent and transient focal ischemia in the rat.* Stroke, 2008. **39**(9): p. 2544-53.
112. Xu, B., et al., *Neuroprotective Effects of a PSD-95 Inhibitor in Neonatal Hypoxic-Ischemic Brain Injury.* Mol Neurobiol, 2016. **53**(9): p. 5962-5970.
113. Sup, S.J., B.G. Green, and S.K. Grant, *2-Iminobiotin is an inhibitor of nitric oxide synthases.* Biochem Biophys Res Commun, 1994. **204**(2): p. 962-8.
114. Bjorkman, S.T., et al., *Short-term dose-response characteristics of 2-iminobiotin immediately postinsult in the neonatal piglet after hypoxia-ischemia.* Stroke, 2013. **44**(3): p. 809-11.
115. Leufkens, P.W., *2-iminobiotin formulations and uses thereof*. 2015, Google Patents.
116. Vitecek, J., et al., *Arginine-based inhibitors of nitric oxide synthase: therapeutic potential and challenges.* Mediators Inflamm, 2012. **2012**: p. 318087.
117. Taheraghdam, A.A., et al., *Allopurinol as a preventive contrivance after acute ischemic stroke in patients with a high level of serum uric acid: a randomized, controlled trial.* Med Princ Pract, 2014. **23**(2): p. 134-9.
118. Rodriguez-Fanjul, J., et al., *Neuroprotection with hypothermia and allopurinol in an animal model of hypoxic-ischemic injury: Is it a gender question?* PLoS One, 2017. **12**(9): p. e0184643.
119. Choi, B.Y., et al., *Prevention of traumatic brain injury-induced neuronal death by inhibition of NADPH oxidase activation.* Brain Res, 2012. **1481**: p. 49-58.
120. Tang, X.N., et al., *Apocynin improves outcome in experimental stroke with a narrow dose range.* Neuroscience, 2008. **154**(2): p. 556-62.
121. Ainsley Dean, P.J., et al., *Potential for use of creatine supplementation following mild traumatic brain injury.* Concussion, 2017. **2**(2): p. CNC34.
122. Lopez-Viota, J., et al., *Electrophoretic characterization of gold nanoparticles functionalized with human serum albumin (HSA) and creatine.* J Colloid Interface Sci, 2009. **332**(1): p. 215-23.
123. Dolan, E., B. Gualano, and E.S. Rawson, *Beyond muscle: the effects of creatine supplementation on brain creatine, cognitive processing, and traumatic brain injury.* Eur J Sport Sci, 2019. **19**(1): p. 1-14.
124. Won, S.J., et al., *Prevention of traumatic brain injury-induced neuron death by intranasal delivery of nicotinamide adenine dinucleotide.* J Neurotrauma, 2012. **29**(7): p. 1401-9.
125. Elizabeth Nance, M.M., *Nanoparticles for Biomedical Applications*, in *Chapter 7 - Challenges and barriers*, L.L. Eun Ji Chung, Carlos Rinaldi, Editor. 2019, Elsevier. p. 89-107.
126. Frohlich, E., *The role of surface charge in cellular uptake and cytotoxicity of medical nanoparticles.* Int J Nanomedicine, 2012. **7**: p. 5577-91.
127. Li, S.D. and L. Huang, *Nanoparticles evading the reticuloendothelial system: role of the supported bilayer.* Biochim Biophys Acta, 2009. **1788**(10): p. 2259-66.
128. Eijsink, V.G., et al., *Directed evolution of enzyme stability.* Biomol Eng, 2005. **22**(1-3): p. 21-30.
129. Lahari, C., et al., *Adsorption induced enzyme denaturation: the role of polymer hydrophobicity in adsorption and denaturation of alpha-chymotrypsin on allyl glycidyl ether (AGE)-ethylene glycol dimethacrylate (EGDM) copolymers.* Langmuir, 2010. **26**(2): p. 1096-106.
130. Nance, E., et al., *Non-invasive delivery of stealth, brain-penetrating nanoparticles across the blood-brain barrier using MRI-guided focused ultrasound.* J Control Release, 2014. **189**: p. 123-132.
131. Pardridge, W.M., *The blood-brain barrier: bottleneck in brain drug development.* NeuroRx, 2005. **2**(1): p. 3-14.
132. Chodobski, A., B.J. Zink, and J. Szmydynger-Chodobska, *Blood-brain barrier pathophysiology in traumatic brain injury.* Transl Stroke Res, 2011. **2**(4): p. 492-516.

133. Jiang, X., et al., *Blood-brain barrier dysfunction and recovery after ischemic stroke.* Prog Neurobiol, 2018. **163-164**: p. 144-171.
134. Moretti, R., et al., *Blood-brain barrier dysfunction in disorders of the developing brain.* Front Neurosci, 2015. **9**: p. 40.
135. Schinkel, A.H., *P-Glycoprotein, a gatekeeper in the blood-brain barrier.* Adv Drug Deliv Rev, 1999. **36**(2-3): p. 179-194.
136. Strazielle, N. and J.F. Ghersi-Egea, *Efflux transporters in blood-brain interfaces of the developing brain.* Front Neurosci, 2015. **9**: p. 21.
137. Blanco, E., H. Shen, and M. Ferrari, *Principles of nanoparticle design for overcoming biological barriers to drug delivery.* Nat Biotechnol, 2015. **33**(9): p. 941-51.
138. Nowak, M., et al., *Size, Shape, and Flexibility Influence Nanoparticle Transport Across Brain Endothelium Under Flow.* Bioengineering & Translational Medicine, 2019: p. e10153.
139. Yellepeddi, V.K., A. Joseph, and E. Nance, *Pharmacokinetics of nanotechnology-based formulations in pediatric populations.* Adv Drug Deliv Rev, 2019. **151-152**: p. 44-55.
140. Zhang, C., et al., *Convection enhanced delivery of cisplatin-loaded brain penetrating nanoparticles cures malignant glioma in rats.* Journal of Controlled Release, 2017. **263**: p. 112-119.
141. Patel, P.J., N.S. Acharya, and S.R. Acharya, *Development and characterization of glutathione-conjugated albumin nanoparticles for improved brain delivery of hydrophilic fluorescent marker.* Drug delivery, 2013. **20**(3-4): p. 143-155.
142. Mei, T., et al., *Encapsulation of tissue plasminogen activator in pH-sensitive self-assembled antioxidant nanoparticles for ischemic stroke treatment - Synergistic effect of thrombolysis and antioxidant.* Biomaterials, 2019. **215**: p. 119209.
143. Wu, W., et al., *Endogenous pH-responsive nanoparticles with programmable size changes for targeted tumor therapy and imaging applications.* Theranostics, 2018. **8**(11): p. 3038-3058.
144. Kulkarni, P.S., et al., *Mmp-9 responsive PEG cleavable nanovesicles for efficient delivery of chemotherapeutics to pancreatic cancer.* Mol Pharm, 2014. **11**(7): p. 2390-9.
145. Cho, H., et al., *Redox-sensitive polymeric nanoparticles for drug delivery.* Chem Commun (Camb), 2012. **48**(48): p. 6043-5.
146. Fisher, D.G. and R.J. Price, *Recent Advances in the Use of Focused Ultrasound for Magnetic Resonance Image-Guided Therapeutic Nanoparticle Delivery to the Central Nervous System.* Front Pharmacol, 2019. **10**: p. 1348.
147. Geho, D.H., et al., *Nanoparticles: potential biomarker harvesters.* Curr Opin Chem Biol, 2006. **10**(1): p. 56-61.
148. Chinen, A.B., et al., *Nanoparticle Probes for the Detection of Cancer Biomarkers, Cells, and Tissues by Fluorescence.* Chem Rev, 2015. **115**(19): p. 10530-74.
149. Reddy, M.K. and V. Labhasetwar, *Nanoparticle-mediated delivery of superoxide dismutase to the brain: an effective strategy to reduce ischemia-reperfusion injury.* FASEB J, 2009. **23**(5): p. 1384-95.
150. Yun, X., et al., *Nanoparticles for targeted delivery of antioxidant enzymes to the brain after cerebral ischemia and reperfusion injury.* J Cereb Blood Flow Metab, 2013. **33**(4): p. 583-92.
151. Stanimirovic, D.B., et al., *Liposome-entrapped superoxide dismutase reduces ischemia/reperfusion 'oxidative stress' in gerbil brain.* Neurochem Res, 1994. **19**(12): p. 1473-8.
152. Imaizumi, S., et al., *Liposome-entrapped superoxide dismutase reduces cerebral infarction in cerebral ischemia in rats.* Stroke, 1990. **21**(9): p. 1312-7.
153. Chan, P.H., S. Longar, and R.A. Fishman, *Protective effects of liposome-entrapped superoxide dismutase on posttraumatic brain edema.* Ann Neurol, 1987. **21**(6): p. 540-7.

154. Jiang, Y., et al., *SOD1 nanozyme with reduced toxicity and MPS accumulation.* J Control Release, 2016. **231**: p. 38-49.
155. Manickam, D.S., et al., *Well-defined cross-linked antioxidant nanozymes for treatment of ischemic brain injury.* J Control Release, 2012. **162**(3): p. 636-45.
156. Liao, R., T.R. Wood, and E. Nance, *Superoxide dismutase reduces monosodium glutamate-induced injury in an organotypic whole hemisphere brain slice model of excitotoxicity.* J Biol Eng, 2020. **14**: p. 3.
157. Haney, M.J., et al., *Cell-mediated transfer of catalase nanoparticles from macrophages to brain endothelial, glial and neuronal cells.* Nanomedicine (Lond), 2011. **6**(7): p. 1215-30.
158. Singhal, A., et al., *Nanoparticle-mediated catalase delivery protects human neurons from oxidative stress.* Cell Death Dis, 2013. **4**: p. e903.
159. Zhang, C., et al., *Direct Macromolecular Drug Delivery to Cerebral Ischemia Area using Neutrophil-Mediated Nanoparticles.* Theranostics, 2017. **7**(13): p. 3260-3275.
160. Petro, M., et al., *Tissue plasminogen activator followed by antioxidant-loaded nanoparticle delivery promotes activation/mobilization of progenitor cells in infarcted rat brain.* Biomaterials, 2016. **81**: p. 169-180.
161. Lutton, E.M., et al., *Acute administration of catalase targeted to ICAM-1 attenuates neuropathology in experimental traumatic brain injury.* Sci Rep, 2017. **7**(1): p. 3846.
162. Islam, M.N., M. Zhang, and B. Adhikari, *The inactivation of enzymes by ultrasound—a review of potential mechanisms.* Food Reviews International, 2014. **30**(1): p. 1-21.
163. van de Weert, M., W.E. Hennink, and W. Jiskoot, *Protein instability in poly(lactic-co-glycolic acid) microparticles.* Pharm Res, 2000. **17**(10): p. 1159-67.
164. Yu, M., et al., *Nanotechnology for protein delivery: Overview and perspectives.* J Control Release, 2016. **240**: p. 24-37.
165. Valgimigli, L., A. Baschieri, and R. Amorati, *Antioxidant activity of nanomaterials.* Journal of Materials Chemistry B, 2018. **6**(14): p. 2036-2051.
166. Takamiya, M., et al., *Strong neuroprotection with a novel platinum nanoparticle against ischemic stroke- and tissue plasminogen activator-related brain damages in mice.* Neuroscience, 2012. **221**: p. 47-55.
167. Rzigalinski, B.A., C.S. Carfagna, and M. Ehrich, *Cerium oxide nanoparticles in neuroprotection and considerations for efficacy and safety.* Wiley Interdiscip Rev Nanomed Nanobiotechnol, 2017. **9**(4).
168. Kim, C.K., et al., *Ceria nanoparticles that can protect against ischemic stroke.* Angew Chem Int Ed Engl, 2012. **51**(44): p. 11039-43.
169. Estevez, A. and J. Erlichman, *Cerium oxide nanoparticles for the treatment of neurological oxidative stress diseases*, in *Oxidative Stress: Diagnostics, Prevention, and Therapy*. 2011, ACS Publications. p. 255-288.
170. Singh, N., C.A. Cohen, and B.A. Rzigalinski, *Treatment of neurodegenerative disorders with radical nanomedicine.* Ann N Y Acad Sci, 2007. **1122**: p. 219-30.
171. Schubert, D., et al., *Cerium and yttrium oxide nanoparticles are neuroprotective.* Biochem Biophys Res Commun, 2006. **342**(1): p. 86-91.
172. Zha, Y.Y., et al., *Concentration-dependent effects of fullerenol on cultured hippocampal neuron viability.* Int J Nanomedicine, 2012. **7**: p. 3099-109.
173. Lin, A.M., et al., *Local carboxyfullerene protects cortical infarction in rat brain.* Neurosci Res, 2002. **43**(4): p. 317-21.
174. Djordjevic, A., et al., *Review of synthesis and antioxidant potential of fullerenol nanoparticles.* Journal of Nanomaterials, 2015. **2015**.

175. Kim, Y.O., et al., *Neuroprotective effects of hydroxyfullerene in rats subjected to global cerebral ischemia.* Cell, 2008. **40**(20): p. 0.
176. Vani, J.R., et al., *Polyhydroxylated fullerene nanoparticles attenuate brain infarction and oxidative stress in rat model of ischemic stroke.* EXCLI J, 2016. **15**: p. 378-90.
177. Samuel, E.L., et al., *Highly efficient conversion of superoxide to oxygen using hydrophilic carbon clusters.* Proceedings of the National Academy of Sciences, 2015. **112**(8): p. 2343-2348.
178. Huq, R., et al., *Preferential uptake of antioxidant carbon nanoparticles by T lymphocytes for immunomodulation.* Sci Rep, 2016. **6**: p. 33808.
179. Nilewski, L.G., et al., *Carbon nanoparticles and oxidative stress: could an injection stop brain damage in minutes?* Nanomedicine (Lond), 2015. **10**(11): p. 1677-9.
180. Fabian, R.H., et al., *Efficacy of Novel Carbon Nanoparticle Antioxidant Therapy in a Severe Model of Reversible Middle Cerebral Artery Stroke in Acutely Hyperglycemic Rats.* Front Neurol, 2018. **9**: p. 199.
181. Bitner, B.R., et al., *Antioxidant carbon particles improve cerebrovascular dysfunction following traumatic brain injury.* ACS Nano, 2012. **6**(9): p. 8007-14.
182. Carlander, U., et al., *Physiologically based pharmacokinetic modeling of nanoceria systemic distribution in rats suggests dose- and route-dependent biokinetics.* Int J Nanomedicine, 2018. **13**: p. 2631-2646.
183. Hendrickson, O., et al., *Fullerenes: in vivo studies of biodistribution, toxicity, and biological action.* Nanotechnologies in Russia, 2014. **9**(11-12): p. 601-617.
184. Bond, W.S. and T.S. Rex, *Evidence that erythropoietin modulates neuroinflammation through differential action on neurons, astrocytes, and microglia.* Frontiers in immunology, 2014. **5**: p. 523.
185. Katavetin, P., et al., *Antioxidative effects of erythropoietin.* Kidney Int Suppl, 2007(107): p. S10-5.
186. Bailey, D.M., et al., *On the antioxidant properties of erythropoietin and its association with the oxidative-nitrosative stress response to hypoxia in humans.* Acta Physiol (Oxf), 2014. **212**(2): p. 175-87.
187. Chen, H., et al., *Nanoerythropoietin is 10-times more effective than regular erythropoietin in neuroprotection in a neonatal rat model of hypoxia and ischemia.* Stroke, 2012. **43**(3): p. 884-7.
188. Dai, W., et al., *Curcumin provides neuroprotection in model of traumatic brain injury via the Nrf2-ARE signaling pathway.* Brain Res Bull, 2018. **140**: p. 65-71.
189. Miao, Y., et al., *Curcumin pretreatment attenuates inflammation and mitochondrial dysfunction in experimental stroke: The possible role of Sirt1 signaling.* Brain Res Bull, 2016. **121**: p. 9-15.
190. Liu, Z., et al., *Curcumin Protects against Ischemic Stroke by Titrating Microglia/Macrophage Polarization.* Front Aging Neurosci, 2017. **9**: p. 233.
191. Kakkar, V., et al., *Curcumin loaded solid lipid nanoparticles: an efficient formulation approach for cerebral ischemic reperfusion injury in rats.* Eur J Pharm Biopharm, 2013. **85**(3 Pt A): p. 339-45.
192. Ahmad, N., et al., *A comparative study of PNIPAM nanoparticles of curcumin, demethoxycurcumin, and bisdemethoxycurcumin and their effects on oxidative stress markers in experimental stroke.* Protoplasma, 2013. **250**(6): p. 1327-38.
193. Liu, Y., et al., *Comprehensive Insights into the Multi-Antioxidative Mechanisms of Melanin Nanoparticles and Their Application To Protect Brain from Injury in Ischemic Stroke.* J Am Chem Soc, 2017. **139**(2): p. 856-862.
194. Bavarsad Shahripour, R., M.R. Harrigan, and A.V. Alexandrov, *N-acetylcysteine (NAC) in neurological disorders: mechanisms of action and therapeutic opportunities.* Brain Behav, 2014. **4**(2): p. 108-22.
195. Nance, E., et al., *Systemic dendrimer-drug treatment of ischemia-induced neonatal white matter injury.* J Control Release, 2015. **214**: p. 112-20.

196. Cunha, R.A., *Neuroprotection by adenosine in the brain: From A(1) receptor activation to A (2A) receptor blockade.* Purinergic Signal, 2005. **1**(2): p. 111-34.
197. Rouquette, M., et al., *Squalene-Adenosine Nanoparticles: Ligands of Adenosine Receptors or Adenosine Prodrug?* J Pharmacol Exp Ther, 2019. **369**(1): p. 144-151.
198. Gaudin, A., et al., *Squalenoyl adenosine nanoparticles provide neuroprotection after stroke and spinal cord injury.* Nat Nanotechnol, 2014. **9**(12): p. 1054-1062.
199. Kusaka, T., et al., *Relationship between cerebral interstitial levels of amino acids and phosphorylation potential during secondary energy failure in hypoxic-ischemic newborn piglets.* Pediatric research, 2004. **55**(2): p. 273-279.
200. Dietrich, W.D. and H.M. Bramlett, *Therapeutic hypothermia and targeted temperature management for traumatic brain injury: Experimental and clinical experience.* Brain circulation, 2017. **3**(4): p. 186.
201. Wassink, G., et al., *Therapeutic hypothermia in neonatal hypoxic-ischemic encephalopathy.* Current neurology and neuroscience reports, 2019. **19**(1): p. 2.
202. Kurisu, K. and M.A. Yenari, *Therapeutic hypothermia for ischemic stroke; pathophysiology and future promise.* Neuropharmacology, 2018. **134**(Pt B): p. 302-309.
203. Wassink, G., et al., *A working model for hypothermic neuroprotection.* J Physiol, 2018. **596**(23): p. 5641-5654.
204. Chakkarapani, E., et al., *Xenon enhances hypothermic neuroprotection in asphyxiated newborn pigs.* Ann Neurol, 2010. **68**(3): p. 330-41.
205. Hobbs, C., et al., *Xenon and hypothermia combine additively, offering long-term functional and histopathologic neuroprotection after neonatal hypoxia/ischemia.* Stroke, 2008. **39**(4): p. 1307-13.
206. Thoresen, M., et al., *Cooling combined with immediate or delayed xenon inhalation provides equivalent long-term neuroprotection after neonatal hypoxia-ischemia.* J Cereb Blood Flow Metab, 2009. **29**(4): p. 707-14.
207. Azzopardi, D., et al., *Moderate hypothermia within 6 h of birth plus inhaled xenon versus moderate hypothermia alone after birth asphyxia (TOBY-Xe): a proof-of-concept, open-label, randomised controlled trial.* Lancet Neurol, 2016. **15**(2): p. 145-153.
208. Thoresen, M., et al., *Post-hypoxic hypothermia reduces cerebrocortical release of NO and excitotoxins.* Neuroreport, 1997. **8**(15): p. 3359-62.
209. Hassell, K.J., et al., *New horizons for newborn brain protection: enhancing endogenous neuroprotection.* Arch Dis Child Fetal Neonatal Ed, 2015. **100**(6): p. F541-52.
210. Wood, T., et al., *Rectal temperature in the first five hours after hypoxia-ischemia critically affects neuropathological outcomes in neonatal rats.* Pediatr Res, 2018. **83**(2): p. 536-544.
211. DeBow, S.B., et al., *Incomplete assessment of experimental cytoprotectants in rodent ischemia studies.* Can J Neurol Sci, 2003. **30**(4): p. 368-74.
212. Galinsky, R., et al., *In the Era of Therapeutic Hypothermia, How Well Do Studies of Perinatal Neuroprotection Control Temperature?* Dev Neurosci, 2017. **39**(1-4): p. 7-22.
213. Liedtke, W.B., *Deconstructing mammalian thermoregulation.* Proc Natl Acad Sci U S A, 2017. **114**(8): p. 1765-1767.
214. Morrison, S.F. and K. Nakamura, *Central neural pathways for thermoregulation.* Front Biosci (Landmark Ed), 2011. **16**: p. 74-104.
215. Nurse, S. and D. Corbett, *Neuroprotection after several days of mild, drug-induced hypothermia.* Journal of Cerebral Blood Flow & Metabolism, 1996. **16**(3): p. 474-480.
216. Rubiano, A.M., et al., *The effect of admission spontaneous hypothermia on patients with severe traumatic brain injury.* Injury, 2013. **44**(9): p. 1219-1225.

217. Konstantinidis, A., et al., *The impact of nontherapeutic hypothermia on outcomes after severe traumatic brain injury.* Journal of Trauma and Acute Care Surgery, 2011. **71**(6): p. 1627-1631.
218. Lascarrou, J.-B., et al., *Targeted temperature management for cardiac arrest with nonshockable rhythm.* New England Journal of Medicine, 2019. **381**(24): p. 2327-2337.
219. Nielsen, N., et al., *Targeted temperature management at 33 C versus 36 C after cardiac arrest.* New England journal of medicine, 2013. **369**(23): p. 2197-2206.
220. Wood, T., et al., *Treatment temperature and insult severity influence the neuroprotective effects of therapeutic hypothermia.* Scientific reports, 2016. **6**(1): p. 1-12.
221. O'Collins, V.E., et al., *1,026 experimental treatments in acute stroke.* Annals of neurology, 2006. **59**(3): p. 467-477.
222. Gebhardt, K., et al., *Prevalence and effect of fever on outcome following resuscitation from cardiac arrest.* Resuscitation, 2013. **84**(8): p. 1062-1067.
223. Laptook, A.R., et al., *Elevated temperature and 6-to 7-year outcome of neonatal encephalopathy.* Annals of neurology, 2013. **73**(4): p. 520-528.
224. Wood, T. and E. Nance, *Disease-directed engineering for physiology-driven treatment interventions in neurological disorders.* APL Bioeng, 2019. **3**(4): p. 040901.
225. Jayaraj, R.L., et al., *Neuroinflammation: friend and foe for ischemic stroke.* J Neuroinflammation, 2019. **16**(1): p. 142.
226. Faden, A.I. and D.J. Loane, *Chronic neurodegeneration after traumatic brain injury: Alzheimer disease, chronic traumatic encephalopathy, or persistent neuroinflammation?* Neurotherapeutics, 2015. **12**(1): p. 143-50.
227. Buetler, T.M., A. Krauskopf, and U.T. Ruegg, *Role of superoxide as a signaling molecule.* News Physiol Sci, 2004. **19**: p. 120-3.
228. Wu, Q.J. and M. Tymianski, *Targeting NMDA receptors in stroke: new hope in neuroprotection.* Mol Brain, 2018. **11**(1): p. 15.
229. Hasbani, M.J., et al., *Distinct roles for sodium, chloride, and calcium in excitotoxic dendritic injury and recovery.* Exp Neurol, 1998. **154**(1): p. 241-58.
230. Arundine, M. and M. Tymianski, *Molecular mechanisms of calcium-dependent neurodegeneration in excitotoxicity.* Cell Calcium, 2003. **34**(4-5): p. 325-37.
231. Kuo, J.R., et al., *Attenuation of brain nitrostative and oxidative damage by brain cooling during experimental traumatic brain injury.* J Biomed Biotechnol, 2011. **2011**: p. 145214.
232. Reyes, R.C., et al., *Activation of neuronal NMDA receptors induces superoxide-mediated oxidative stress in neighboring neurons and astrocytes.* J Neurosci, 2012. **32**(37): p. 12973-8.
233. Reddy, M.K., et al., *Superoxide dismutase-loaded PLGA nanoparticles protect cultured human neurons under oxidative stress.* Appl Biochem Biotechnol, 2008. **151**(2-3): p. 565-77.
234. Humpel, C., *Organotypic brain slice cultures: A review.* Neuroscience, 2015. **305**: p. 86-98.
235. Kalivas, P., *Extracellular glutamate: functional compartments operate in different concentration ranges.* Frontiers in systems neuroscience, 2011. **5**: p. 94.
236. Infanger, D.W., R.V. Sharma, and R.L. Davisson, *NADPH oxidases of the brain: distribution, regulation, and function.* Antioxidants & redox signaling, 2006. **8**(9-10): p. 1583-1596.
237. Jones, E.V., D. Cook, and K.K. Murai, *A neuron-astrocyte co-culture system to investigate astrocyte-secreted factors in mouse neuronal development*, in *Astrocytes*. 2012, Springer. p. 341-352.
238. Roque, P.J. and L.G. Costa, *Co-Culture of Neurons and Microglia.* Curr Protoc Toxicol, 2017. **74**: p. 11 24 1-11 24 17.
239. Schermer, C. and C. Humpel, *Granulocyte macrophage-colony stimulating factor activates microglia in rat cortex organotypic brain slices.* Neuroscience letters, 2002. **328**(2): p. 180-184.

240. Scimemi, A. and M. Beato, *Determining the neurotransmitter concentration profile at active synapses.* Mol Neurobiol, 2009. **40**(3): p. 289-306.
241. Huuskonen, J., et al., *A refined in vitro model to study inflammatory responses in organotypic membrane culture of postnatal rat hippocampal slices.* J Neuroinflammation, 2005. **2**: p. 25.
242. Sheppard, O., M.P. Coleman, and C.S. Durrant, *Lipopolysaccharide-induced neuroinflammation induces presynaptic disruption through a direct action on brain tissue involving microglia-derived interleukin 1 beta.* J Neuroinflammation, 2019. **16**(1): p. 106.
243. Tanaka, M., P.B. Chock, and E.R. Stadtman, *Oxidized messenger RNA induces translation errors.* Proceedings of the National Academy of Sciences of the United States of America, 2007. **104**(1): p. 66-71.
244. Romero-Santacreu, L., et al., *Specific and global regulation of mRNA stability during osmotic stress in Saccharomyces cerevisiae.* Rna, 2009. **15**(6): p. 1110-1120.
245. Zhang, X.M., et al., *Gender differences in susceptibility to kainic acid-induced neurodegeneration in aged C57BL/6 mice.* Neurotoxicology, 2008. **29**(3): p. 406-412.
246. Gaignard, P., et al., *Sex differences in brain mitochondrial metabolism: influence of endogenous steroids and stroke.* Journal of Neuroendocrinology, 2018. **30**(2).
247. Silaidos, C., et al., *Sex-associated differences in mitochondrial function in human peripheral blood mononuclear cells (PBMCs) and brain.* Biology of Sex Differences, 2018. **9**.
248. Wagner, A.K., et al., *Relationships between cerebrospinal fluid markers of excitotoxicity, ischemia, and oxidative damage after severe TBI: The impact of gender, age, and hypothermia.* Journal of Neurotrauma, 2004. **21**(2): p. 125-136.
249. Viviani, B., et al., *Perspectives on neuroinflammation and excitotoxicity: a neurotoxic conspiracy?* Neurotoxicology, 2014. **43**: p. 10-20.
250. Gauberti, M., S.M. De Lizarrondo, and D. Vivien, *The "inflammatory penumbra" in ischemic stroke: From clinical data to experimental evidence.* European Stroke Journal, 2016. **1**(1): p. 20-27.
251. Hou, T.T., et al., *Synergistic Triggering of Superoxide Flashes by Mitochondrial Ca2+ Uniport and Basal Reactive Oxygen Species Elevation.* Journal of Biological Chemistry, 2013. **288**(7): p. 4602-4612.
252. Morland, C., M.N. Pettersen, and B. Hassel, *Hyperosmolar sodium chloride is toxic to cultured neurons and causes reduction of glucose metabolism and ATP levels, an increase in glutamate uptake, and a reduction in cytosolic calcium.* Neurotoxicology, 2016. **54**: p. 34-43.
253. Nguyen, T., P. Nioi, and C.B. Pickett, *The Nrf2-Antioxidant Response Element Signaling Pathway and Its Activation by Oxidative Stress.* Journal of Biological Chemistry, 2009. **284**(20): p. 13291-13295.
254. Wright, F.L., et al., *Hyperosmolarity Invokes Distinct Anti-Inflammatory Mechanisms in Pulmonary Epithelial Cells: Evidence from Signaling and Transcription Layers.* Plos One, 2014. **9**(12).
255. Milani, P., et al., *SOD1 Transcriptional and Posttranscriptional Regulation and Its Potential Implications in ALS.* Neurol Res Int, 2011. **2011**: p. 458427.
256. Zhu, C.H., et al., *A family of AP-2 proteins down-regulate manganese superoxide dismutase expression.* J Biol Chem, 2001. **276**(17): p. 14407-13.
257. Minatohara, K., M. Akiyoshi, and H. Okuno, *Role of Immediate-Early Genes in Synaptic Plasticity and Neuronal Ensembles Underlying the Memory Trace.* Front Mol Neurosci, 2015. **8**: p. 78.
258. López-Pérez, S.J., M.E. Ureña-Guerrero, and A. Morales-Villagrán, *Monosodium glutamate neonatal treatment as a seizure and excitotoxic model.* Brain research, 2010. **1317**: p. 246-256.
259. Molin, C., et al., *mRNA stability changes precede changes in steady-state mRNA amounts during hyperosmotic stress.* RNA, 2009. **15**(4): p. 600-14.

260. Fimognari, C., *Role of Oxidative RNA Damage in Chronic-Degenerative Diseases.* Oxid Med Cell Longev, 2015. **2015**: p. 358713.
261. Kong, Q. and C.L. Lin, *Oxidative damage to RNA: mechanisms, consequences, and diseases.* Cell Mol Life Sci, 2010. **67**(11): p. 1817-29.
262. Shan, Y., L.R. Carlock, and P.D. Walker, *NMDA receptor overstimulation triggers a prolonged wave of immediate early gene expression: Relationship to excitotoxicity.* Experimental Neurology, 1997. **144**(2): p. 406-415.
263. Rao, V.L.R., et al., *Traumatic injury to rat brain upregulates neuronal nitric oxide synthase expression and L-[H-3]nitroarginine binding.* Journal of Neurotrauma, 1999. **16**(10): p. 865-877.
264. van den Tweel, E.R.W., et al., *Expression of nitric oxide synthase isoforms and nitrotyrosine formation after hypoxia-ischemia in the neonatal rat brain.* Journal of Neuroimmunology, 2005. **167**(1-2): p. 64-71.
265. Sasaki, M., et al., *Dynamic regulation of neuronal NO synthase transcription by calcium influx through a CREB family transcription factor-dependent mechanism.* Proceedings of the National Academy of Sciences of the United States of America, 2000. **97**(15): p. 8617-8622.
266. Bonfoco, E., et al., *Apoptosis and necrosis: two distinct events induced, respectively, by mild and intense insults with N-methyl-D-aspartate or nitric oxide/superoxide in cortical cell cultures.* Proceedings of the National Academy of Sciences, 1995. **92**(16): p. 7162-7166.
267. Youle, R.J. and A.M. van der Bliek, *Mitochondrial fission, fusion, and stress.* Science, 2012. **337**(6098): p. 1062-5.
268. Choi, S.R., et al., *Neuronal NOS Activates Spinal NADPH Oxidase 2 Contributing to Central Sigma-1 Receptor-Induced Pain Hypersensitivity in Mice.* Biol Pharm Bull, 2016. **39**(12): p. 1922-1931.
269. Patel, A., et al., *Recent advances in protein and Peptide drug delivery: a special emphasis on polymeric nanoparticles.* Protein Pept Lett, 2014. **21**(11): p. 1102-20.
270. Langguth, P., et al., *The challenge of proteolytic enzymes in intestinal peptide delivery.* Journal of controlled release, 1997. **46**(1-2): p. 39-57.
271. Muzykantov, V.R., *Targeting of superoxide dismutase and catalase to vascular endothelium.* J Control Release, 2001. **71**(1): p. 1-21.
272. Kreuter, J., *Drug delivery to the central nervous system by polymeric nanoparticles: what do we know?* Adv Drug Deliv Rev, 2014. **71**: p. 2-14.
273. Vauthier, C. and K. Bouchemal, *Methods for the preparation and manufacture of polymeric nanoparticles.* Pharm Res, 2009. **26**(5): p. 1025-58.
274. Patel, T., et al., *Polymeric nanoparticles for drug delivery to the central nervous system.* Adv Drug Deliv Rev, 2012. **64**(7): p. 701-5.
275. Petri, B., et al., *Chemotherapy of brain tumour using doxorubicin bound to surfactant-coated poly(butyl cyanoacrylate) nanoparticles: revisiting the role of surfactants.* J Control Release, 2007. **117**(1): p. 51-8.
276. Avgoustakis, K., *Pegylated poly(lactide) and poly(lactide-co-glycolide) nanoparticles: preparation, properties and possible applications in drug delivery.* Curr Drug Deliv, 2004. **1**(4): p. 321-33.
277. Bilati, U., E. Allemann, and E. Doelker, *Nanoprecipitation versus emulsion-based techniques for the encapsulation of proteins into biodegradable nanoparticles and process-related stability issues.* AAPS PharmSciTech, 2005. **6**(4): p. E594-604.
278. Wang, Y., W. Luo, and G. Reiser, *Trypsin and trypsin-like proteases in the brain: proteolysis and cellular functions.* Cell Mol Life Sci, 2008. **65**(2): p. 237-52.
279. Pope, A. and R.A. Nixon, *Proteases of human brain.* Neurochem Res, 1984. **9**(3): p. 291-323.
280. Cao, C., et al., *Catalase is regulated by ubiquitination and proteosomal degradation. Role of the c-Abl and Arg tyrosine kinases.* Biochemistry, 2003. **42**(35): p. 10348-53.

281. Mokni, M., et al., *Effect of resveratrol on antioxidant enzyme activities in the brain of healthy rat.* Neurochem Res, 2007. **32**(6): p. 981-7.
282. Quillinan, N., P.S. Herson, and R.J. Traystman, *Neuropathophysiology of Brain Injury.* Anesthesiol Clin, 2016. **34**(3): p. 453-64.
283. Locatelli, E. and M.C. Franchini, *Biodegradable PLGA-b-PEG polymeric nanoparticles: synthesis, properties, and nanomedical applications as drug delivery system.* Journal of Nanoparticle Research, 2012. **14**(12): p. 1316.
284. Li, Y., et al., *PEGylated PLGA nanoparticles as protein carriers: synthesis, preparation and biodistribution in rats.* J Control Release, 2001. **71**(2): p. 203-11.
285. Wang, R., et al., *Generation of toxic degradation products by sonication of Pluronic(R) dispersants: implications for nanotoxicity testing.* Nanotoxicology, 2013. **7**(7): p. 1272-81.
286. Cimarosti, H. and J.M. Henley, *Investigating the mechanisms underlying neuronal death in ischemia using in vitro oxygen-glucose deprivation: potential involvement of protein SUMOylation.* Neuroscientist, 2008. **14**(6): p. 626-36.
287. Winterbourn, C.C., *Revisiting the reactions of superoxide with glutathione and other thiols.* Arch Biochem Biophys, 2016. **595**: p. 68-71.
288. Ziembowicz, S., M. Kida, and P. Koszelnik. *Sonochemical formation of hydrogen peroxide*. in *Multidisciplinary Digital Publishing Institute Proceedings*. 2017.
289. Miljevic, B., et al., *To sonicate or not to sonicate PM filters: reactive oxygen species generation upon ultrasonic irradiation.* Aerosol science and technology, 2014. **48**(12): p. 1276-1284.
290. Kaczmarek, H., L. Lindén, and J. Rabek, *Reactions of hydroxyl (HO•) and hydroperoxyl (HO) radicals generated chemically and photochemically with poly (ethylene oxide).* Journal of Polymer Science Part A: Polymer Chemistry, 1995. **33**(6): p. 879-890.
291. Kawasaki, H., Y. Takeda, and R. Arakawa, *Mass spectrometric analysis for high molecular weight synthetic polymers using ultrasonic degradation and the mechanism of degradation.* Anal Chem, 2007. **79**(11): p. 4182-7.
292. Vijayalakshmi, S. and G. Madras, *Effect of initial molecular weight and solvents on the ultrasonic degradation of poly (ethylene oxide).* Polymer Degradation and stability, 2005. **90**(1): p. 116-122.
293. Pielichowski, K. and K. Flejtuch, *Differential scanning calorimetry studies on poly (ethylene glycol) with different molecular weights for thermal energy storage materials.* Polymers for Advanced Technologies, 2002. **13**(10-12): p. 690-696.
294. Majumdar, R., K. Alexander, and A. Riga, *Physical characterization of polyethylene glycols by thermal analytical technique and the effect of humidity and molecular weight.* Die Pharmazie-An International Journal of Pharmaceutical Sciences, 2010. **65**(5): p. 343-347.
295. Giroto, J.A., et al., *Degradation of poly (ethylene glycol) in aqueous solution by photo-Fenton and H2O2/UV processes.* Industrial & engineering chemistry research, 2010. **49**(7): p. 3200-3206.
296. CHIBA, A., T. FURUGORI, and W.-C. WU, *Ultrasonic decomposition of dichloromethane.* Journal of The Surface Finishing Society of Japan, 1994. **45**(7): p. 735-738.
297. Cheng, Q., et al., *Ultrasound-assisted SWNTs dispersion: effects of sonication parameters and solvent properties.* The Journal of Physical Chemistry C, 2010. **114**(19): p. 8821-8827.
298. Camerotto, E., et al., *Influence of surface tension on cavitation noise spectra and particle removal efficiency in high frequency ultrasound fields.* Journal of Applied Physics, 2012. **112**(11): p. 114322.
299. Thomson, G.W., *The Antoine Equation for Vapor-pressure Data.* Chemical reviews, 1946. **38**(1): p. 1-39.
300. Riesz, P., D. Berdahl, and C. Christman, *Free radical generation by ultrasound in aqueous and nonaqueous solutions.* Environmental Health Perspectives, 1985. **64**: p. 233-252.

301. Malzert-Fréon, A., J.-P. Benoît, and F. Boury, *Interactions between poly (ethylene glycol) and protein in dichloromethane/water emulsions: A study of interfacial properties.* European journal of pharmaceutics and biopharmaceutics, 2008. **69**(3): p. 835-843.
302. Luo, J., R. Borgens, and R. Shi, *Polyethylene glycol improves function and reduces oxidative stress in synaptosomal preparations following spinal cord injury.* Journal of neurotrauma, 2004. **21**(8): p. 994-1007.
303. Koob, A.O., et al., *Intravenous polyethylene glycol inhibits the loss of cerebral cells after brain injury.* Journal of neurotrauma, 2005. **22**(10): p. 1092-1111.
304. Douglas-Escobar, M. and M.D. Weiss, *Hypoxic-ischemic encephalopathy: a review for the clinician.* JAMA pediatrics, 2015. **169**(4): p. 397-403.
305. Johnson, W., et al., *Stroke: a global response is needed.* Bulletin of the World Health Organization, 2016. **94**(9): p. 634.
306. Edwards, A.D., et al., *Neurological outcomes at 18 months of age after moderate hypothermia for perinatal hypoxic ischaemic encephalopathy: synthesis and meta-analysis of trial data.* Bmj, 2010. **340**: p. c363.
307. Albers, G.W., et al., *Antithrombotic and thrombolytic therapy for ischemic stroke: the Seventh ACCP Conference on Antithrombotic and Thrombolytic Therapy.* Chest, 2004. **126**(3): p. 483S-512S.
308. Priller, J. and M. Prinz, *Targeting microglia in brain disorders.* Science, 2019. **365**(6448): p. 32-33.
309. Nance, E., et al., *Dendrimer-mediated delivery of N-acetyl cysteine to microglia in a mouse model of Rett syndrome.* J Neuroinflammation, 2017. **14**(1): p. 252.
310. Nance, E., et al., *Nanoscale effects in dendrimer-mediated targeting of neuroinflammation.* Biomaterials, 2016. **101**: p. 96-107.
311. Tasca, C.I., T. Dal-Cim, and H. Cimarosti, *In vitro oxygen-glucose deprivation to study ischemic cell death.* Methods Mol Biol, 2015. **1254**: p. 197-210.
312. Fujimoto, S., et al., *Mechanisms of oxygen glucose deprivation-induced glutamate release from cerebrocortical slice cultures.* Neurosci Res, 2004. **50**(2): p. 179-87.
313. Hall, A.A., et al., *Delayed treatments for stroke influence neuronal death in rat organotypic slice cultures subjected to oxygen glucose deprivation.* Neuroscience, 2009. **164**(2): p. 470-7.
314. De Alba, J., et al., *Down-regulation of neuronal nitric oxide synthase by nitric oxide after oxygen-glucose deprivation in rat forebrain slices.* J Neurochem, 1999. **72**(1): p. 248-54.
315. Amantea, D., et al., *Azithromycin protects mice against ischemic stroke injury by promoting macrophage transition towards M2 phenotype.* Exp Neurol, 2016. **275 Pt 1**: p. 116-25.
316. Parnham, M.J., et al., *Azithromycin: mechanisms of action and their relevance for clinical applications.* Pharmacol Ther, 2014. **143**(2): p. 225-45.
317. Bosco, A., et al., *Neurodegeneration severity can be predicted from early microglia alterations monitored in vivo in a mouse model of chronic glaucoma.* Dis Model Mech, 2015. **8**(5): p. 443-55.
318. Pavese, N., et al., *Microglial activation correlates with severity in Huntington disease: a clinical and PET study.* Neurology, 2006. **66**(11): p. 1638-43.
319. Barks, J.D.E., et al., *Repurposing azithromycin for neonatal neuroprotection.* Pediatr Res, 2019. **86**(4): p. 444-451.
320. Saver, J.L., *Time is brain—quantified.* Stroke, 2006. **37**(1): p. 263-266.
321. Lawson, L.J., et al., *Heterogeneity in the distribution and morphology of microglia in the normal adult mouse brain.* Neuroscience, 1990. **39**(1): p. 151-70.
322. Gomez-Nicola, D. and V.H. Perry, *Microglial dynamics and role in the healthy and diseased brain: a paradigm of functional plasticity.* Neuroscientist, 2015. **21**(2): p. 169-84.
323. Choi, B., et al., *Highly selective microglial uptake of ceria-zirconia nanoparticles for enhanced analgesic treatment of neuropathic pain.* Nanoscale, 2019. **11**(41): p. 19437-19447.

324. MacParland, S.A., et al., *Phenotype Determines Nanoparticle Uptake by Human Macrophages from Liver and Blood.* ACS Nano, 2017. **11**(3): p. 2428-2443.
325. Amsden, B., *Solute diffusion within hydrogels. Mechanisms and models.* Macromolecules, 1998. **31**(23): p. 8382-8395.
326. Strasser, U. and G. Fischer, *Quantitative measurement of neuronal degeneration in organotypic hippocampal cultures after combined oxygen/glucose deprivation.* J Neurosci Methods, 1995. **57**(2): p. 177-86.
327. Holloway, P.M. and F.N. Gavins, *Modeling Ischemic Stroke In Vitro: Status Quo and Future Perspectives.* Stroke, 2016. **47**(2): p. 561-9.
328. Kalda, A., et al., *Medium transitory oxygen-glucose deprivation induced both apoptosis and necrosis in cerebellar granule cells.* Neurosci Lett, 1998. **240**(1): p. 21-4.
329. Gwag, B.J., et al., *Blockade of glutamate receptors unmasks neuronal apoptosis after oxygen-glucose deprivation in vitro.* Neuroscience, 1995. **68**(3): p. 615-9.
330. Fernandez-Lopez, D., et al., *Immature rat brain slices exposed to oxygen-glucose deprivation as an in vitro model of neonatal hypoxic-ischemic encephalopathy.* J Neurosci Methods, 2005. **145**(1-2): p. 205-12.
331. Berger, R., et al., *Effect of mild hypothermia during and after transient in vitro ischemia on metabolic disturbances in hippocampal slices at different stages of development.* Brain Res Dev Brain Res, 1998. **105**(1): p. 67-77.
332. Brongholi, K., et al., *Oxygen–glucose deprivation decreases glutathione levels and glutamate uptake in rat hippocampal slices.* Brain research, 2006. **1083**(1): p. 211-218.
333. Ravindranath, V. and D.J. Reed, *Glutathione depletion and formation of glutathione-protein mixed disulfide following exposure of brain mitochondria to oxidative stress.* Biochem Biophys Res Commun, 1990. **169**(3): p. 1075-9.
334. Burd, I., et al., *Fetal uptake of intra-amniotically delivered dendrimers in a mouse model of intrauterine inflammation and preterm birth.* Nanomedicine, 2014. **10**(6): p. 1343-51.
335. Block, M.L., L. Zecca, and J.S. Hong, *Microglia-mediated neurotoxicity: uncovering the molecular mechanisms.* Nat Rev Neurosci, 2007. **8**(1): p. 57-69.
336. Nemeth, C.L., et al., *Uptake of dendrimer-drug by different cell types in the hippocampus after hypoxic-ischemic insult in neonatal mice: Effects of injury, microglial activation and hypothermia.* Nanomedicine, 2017. **13**(7): p. 2359-2369.
337. Kambhampati, S.P., et al., *Systemic and Intravitreal Delivery of Dendrimers to Activated Microglia/Macrophage in Ischemia/Reperfusion Mouse Retina.* Invest Ophthalmol Vis Sci, 2015. **56**(8): p. 4413-24.
338. Kannan, S., et al., *Dendrimer-based postnatal therapy for neuroinflammation and cerebral palsy in a rabbit model.* Sci Transl Med, 2012. **4**(130): p. 130ra46.
339. Girard, S., et al., *Microglia and macrophages differentially modulate cell death after brain injury caused by oxygen-glucose deprivation in organotypic brain slices.* Glia, 2013. **61**(5): p. 813-24.
340. Suh, H.S., M.O. Kim, and S.C. Lee, *Inhibition of granulocyte-macrophage colony-stimulating factor signaling and microglial proliferation by anti-CD45RO: role of Hck tyrosine kinase and phosphatidylinositol 3-kinase/Akt.* J Immunol, 2005. **174**(5): p. 2712-9.
341. Mitrasinovic, O.M., et al., *Microglia overexpressing the macrophage colony-stimulating factor receptor are neuroprotective in a microglial-hippocampal organotypic coculture system.* J Neurosci, 2005. **25**(17): p. 4442-51.
342. Mausberg, A.K., S. Jander, and G. Reichmann, *Intracerebral granulocyte-macrophage colony-stimulating factor induces functionally competent dendritic cells in the mouse brain.* Glia, 2009. **57**(12): p. 1341-50.

343. Dubbelaar, M.L., et al., *The Kaleidoscope of Microglial Phenotypes.* Front Immunol, 2018. **9**: p. 1753.
344. Zhang, F., et al., *Targeting specific cells in the brain with nanomedicines for CNS therapies.* J Control Release, 2016. **240**: p. 212-226.
345. McWhorter, F.Y., et al., *Modulation of macrophage phenotype by cell shape.* Proceedings of the National Academy of Sciences, 2013. **110**(43): p. 17253-17258.
346. Fernandez-Arjona, M.D.M., et al., *Microglia Morphological Categorization in a Rat Model of Neuroinflammation by Hierarchical Cluster and Principal Components Analysis.* Front Cell Neurosci, 2017. **11**: p. 235.
347. Ransohoff, R.M., *A polarizing question: do M1 and M2 microglia exist?* Nature neuroscience, 2016. **19**(8): p. 987.
348. Bottema, M.J. *Circularity of objects in images*. in *2000 IEEE International Conference on Acoustics, Speech, and Signal Processing. Proceedings (Cat. No. 00CH37100)*. 2000. IEEE.
349. Smith, E.S., J.E. Porterfield, and R.M. Kannan, *Leveraging the interplay of nanotechnology and neuroscience: Designing new avenues for treating central nervous system disorders.* Adv Drug Deliv Rev, 2019. **148**: p. 181-203.
350. Sun, J., et al., *Tunable rigidity of (polymeric core)-(lipid shell) nanoparticles for regulated cellular uptake.* Adv Mater, 2015. **27**(8): p. 1402-7.
351. Hutter, E., et al., *Microglial response to gold nanoparticles.* ACS Nano, 2010. **4**(5): p. 2595-606.
352. Ducray, A.D., et al., *Uptake of silica nanoparticles in the brain and effects on neuronal differentiation using different in vitro models.* Nanomedicine, 2017. **13**(3): p. 1195-1204.
353. Nance, E., et al., *Brain-penetrating nanoparticles improve paclitaxel efficacy in malignant glioma following local administration.* ACS nano, 2014. **8**(10): p. 10655-10664.
354. Zhang, C., et al., *Strategies to enhance the distribution of nanotherapeutics in the brain.* Journal of Controlled Release, 2017. **267**: p. 232-239.
355. Nance, E.A., et al., *A dense poly(ethylene glycol) coating improves penetration of large polymeric nanoparticles within brain tissue.* Sci Transl Med, 2012. **4**(149): p. 149ra119.
356. Rice, M.E. and C. Nicholson, *Diffusion characteristics and extracellular volume fraction during normoxia and hypoxia in slices of rat neostriatum.* J Neurophysiol, 1991. **65**(2): p. 264-72.
357. Perez-Pinzon, M.A., L. Tao, and C. Nicholson, *Extracellular potassium, volume fraction, and tortuosity in rat hippocampal CA1, CA3, and cortical slices during ischemia.* J Neurophysiol, 1995. **74**(2): p. 565-73.
358. Sykova, E. and C. Nicholson, *Diffusion in brain extracellular space.* Physiol Rev, 2008. **88**(4): p. 1277-340.
359. del Zoppo, G.J., et al., *Microglial activation and matrix protease generation during focal cerebral ischemia.* Stroke, 2007. **38**(2 Suppl): p. 646-51.
360. Brisson, C.D., M.K. Lukewich, and R.D. Andrew, *A distinct boundary between the higher brain's susceptibility to ischemia and the lower brain's resistance.* PLoS One, 2013. **8**(11).
361. Dirnagl, U., *Inflammation in stroke: the good, the bad, and the unknown.* Ernst Schering Res Found Workshop, 2004(47): p. 87-99.
362. Buetler, T.M., A. Krauskopf, and U.T. Ruegg, *Role of superoxide as a signaling molecule.* Physiology, 2004. **19**(3): p. 120-123.
363. de Vries, L.S. and F. Groenendaal, *Patterns of neonatal hypoxic-ischaemic brain injury.* Neuroradiology, 2010. **52**(6): p. 555-66.
364. Varano, G.P., et al., *Post-ischemic treatment with azithromycin protects ganglion cells against retinal ischemia/reperfusion injury in the rat.* Mol Vis, 2017. **23**: p. 911-921.

365. Cuevas, S., et al., *Mechanisms involved in the antioxidant properties of azithromycin in lung epithelial cells stimulated with cigarette smoke extract.* The FASEB Journal, 2016. **30**(1_supplement): p. 982.2-982.2.